

MEASUREMENT OF THE TOP QUARK MASS IN THE ALL
HADRONIC CHANNEL AT THE TEVATRON

By

GHEORGHE LUNGU

A DISSERTATION PRESENTED TO THE GRADUATE SCHOOL
OF THE UNIVERSITY OF FLORIDA IN PARTIAL FULFILLMENT
OF THE REQUIREMENTS FOR THE DEGREE OF
DOCTOR OF PHILOSOPHY

UNIVERSITY OF FLORIDA

2007

© 2007 Gheorghe Lungu

To my wife, Corina.

ACKNOWLEDGMENTS

The first person I want to acknowledge is my advisor, Prof. Jacobo Konigsberg, for guiding and supporting me during my graduate student years in many ways. His dedication, his commitment to his work and his students, and his savviness in the high-energy experimental field serve as an example to which I aspire as a physicist and as a scientist.

Also I will be forever grateful to Dr. Valentin Neula in many aspects. He made possible many things for me starting with lending me money to pay the tests needed for admission in the graduate school at the University of Florida. Moreover, he contributed greatly to the success of this analysis, from the writing the C++ code for main tools and ending with rich and enlightening discussions on the topic. His great skills and his excellence represent a standard for me.

I would like to mention the great influence I received in my first years at the University of Florida from Prof. Kevin Ingersent and Prof. Richard Woodard. With or without their awareness, they helped me deepen my knowledge in theoretical physics. Also I take this opportunity to thank the members of the committee supervising this thesis: Dr. Toshikazu Nishida, Dr. Richard Field, Dr. Pierre Ramond and Dr. Guenakh Mitselmakher. I will be inspired by their tremendous work and by their extraordinary achievements in physics. Despite our rather brief interaction, I want to mention that my experience during my Oral Examination helped redefine me as a physicist and as a person.

At CDF I drew much knowledge from interacting with many people such as Dr. Roberto Rossin, Dr. Andrea Castro, Dr. Patrizia Azzi, Dr. Fabrizio Margaroli, Dr. Florencia Canelli, Dr. Daniel Whiteson, Dr. Nathan Goldschmidt, Dr. Unki Yang, Dr. Erik Brubaker, Dr. Douglas Glenzinski, Dr. Alexandre Pronko, Dr. Mircea Coca, Dr. Gavril Giurgiu. Special thanks to Dr. Dmitri Tsybychev, Dr. Alexander Sukhanov and Dr. Song Ming Wang who helped me greatly getting up to the speed of the experimental physics at CDF. Also I want to mention and thank Yuri Oksuzian and Lester Pinera for

many interesting discussions we had and for being the friends I needed during difficult times.

At last, yet most importantly, I want to thank my wife, Corina, whom I dedicate this work. Without her constant support, criticism and love I wouldn't have succeeded in finding the balance needed to reach this goal. Also I thank my father and my sisters for loving me, and my mother who will be always in my mind.

TABLE OF CONTENTS

	<u>page</u>
ACKNOWLEDGMENTS	4
LIST OF TABLES	9
LIST OF FIGURES	10
ABSTRACT	14
CHAPTER	
1 INTRODUCTION	15
1.1 History of Particle Physics	15
1.2 The Standard Model	21
1.3 Top Quark Physics	23
1.4 Highlights of Mass Measurement	32
2 EXPERIMENTAL APPARATUS	38
2.1 Tevatron Overview	38
2.2 CDF Overview and Design	40
2.2.1 Cherenkov Luminosity Counters	41
2.2.2 Silicon Tracking	42
2.2.3 Central Outer Tracker	42
2.2.4 Calorimeters	43
2.2.5 The Muon System	44
2.2.6 The Trigger System	44
3 EVENT RECONSTRUCTION	51
3.1 Tracks	51
3.2 Vertex Reconstruction	53
3.3 Jets Reconstruction	54
3.3.1 Relative Energy Scale Correction	56
3.3.2 Multiple Interactions Correction	57
3.3.3 Absolute Energy Scale Correction	57
3.3.4 Underlying Event Correction	58
3.3.5 Out of Cone Correction	58
3.4 Leptons Reconstruction	59
3.4.1 Electrons	59
3.4.2 Muons	59
3.4.3 Tau Leptons	60
3.4.4 Neutrinos	60
3.5 Photon Reconstruction	60
3.6 Bottom Quark Tagging	61

3.6.1	SecVtx Algorithm	61
3.6.2	Jet Probability Algorithm	62
3.6.3	Soft Lepton Tag Algorithm	62
4	DESCRIPTION OF THE MATRIX ELEMENT MACHINERY	68
4.1	Probability Density Definition	68
4.2	Combinatorics	70
4.3	Calculation of the Matrix Element	71
4.4	Transfer Functions	76
4.5	Transverse Momentum of the $t\bar{t}$ System	78
4.6	Implementation and Evaluation of the Probability Density	79
4.7	Checks of the Matrix Element Calculation	84
5	DATA SAMPLE AND EVENT SELECTION	91
5.1	Data and Monte Carlo Samples	91
5.2	Event Selection	91
6	BACKGROUND MODEL	97
6.1	Definition	97
6.2	Validation of the Background Model	98
6.2.1	Validation in Control Region 1	98
6.2.2	Validation in Control Region 2	99
6.2.3	Validation in the Signal Region	99
6.2.4	Effects on the Statistical Uncertainty	99
7	DESCRIPTION OF THE MASS MEASUREMENT METHOD	104
7.1	Likelihood Definitions	104
7.2	Top Templates	106
7.2.1	Definition of the Template	106
7.2.2	Parameterization of the Templates	106
7.3	Dijet Mass Templates	108
7.3.1	Definition of the Template	108
7.3.2	Parameterization of the Templates	108
8	MODEL VALIDATION AND SENSITIVITY STUDIES	114
8.1	Pseudo-experiments Setup	114
8.2	Validation of the Model	115
8.3	Expected Statistical Uncertainty	118
9	SYSTEMATIC UNCERTAINTIES	127
9.1	Jet Fragmentation	127
9.2	Initial State Radiation	127
9.3	Final State Radiation	128

9.4	Proton and Antiproton PDFs	128
9.5	Background Shape	128
9.6	Background Statistics	129
9.7	Correlation Between Top Mass and Dijet Mass	130
9.8	2D Calibration	130
9.9	B-jet Energy Scale	131
9.10	Residual Jet Energy Scale	131
9.11	Summary of the Systematic Uncertainties	132
10	CONCLUSION	136
APPENDIX		
A	PARTON DISTRIBUTION FUNCTION OF THE PROTON	141
B	TRANSVERSE MOMENTUM OF THE $T\bar{T}$ SYSTEM	142
C	TRANSFER FUNCTIONS	143
D	SIGNAL TOP TEMPLATES	149
E	SIGNAL DIJET MASS TEMPLATES	163
REFERENCES		177
BIOGRAPHICAL SKETCH		181

LIST OF TABLES

<u>Table</u>	<u>page</u>
1-1 Classification of the fundamental fermions in Standard Model.	34
1-2 Force carriers described in Standard Model.	34
1-3 Branching ratios of the $t\bar{t}$ decay channels.	35
4-1 Definition of the binning of the parton pseudo-rapidity	85
4-2 Definition of the binning of the parton energy for b -jets	86
4-3 Definition of the binning of the parton energy for W -jets	87
5-1 Number of events in the multi-jet data	94
5-2 Number of events in the $t\bar{t}$ Monte Carlo sample	94
5-3 Expected signal to background ratios for the $t\bar{t}$ Monte Carlo samples.	95
5-4 Efficiency of the $minLKL$ cut for the $t\bar{t}$ Monte Carlo samples.	96
7-1 Values of the parameters describing the shapes of the top templates for the $t\bar{t}$ samples.	110
7-2 Values of the parameters describing the shapes of the top templates in the case of the background events.	110
7-3 Values of the parameters describing the dijet mass templates shapes for the $t\bar{t}$ samples.	112
7-4 Values of the parameters describing the dijet mass templates shapes in the case of the background events.	113
8-1 Value of the correlation factor between any two pseudo-experiments	119
8-2 Linearity check of the M_{top} and JES reconstruction	119
9-1 Uncertainties on the parameters of the top mass templates for background.	132
9-2 Residual jet energy scale uncertainty on the top mass.	132
9-3 Summary of the systematic sources of uncertainty on the top mass.	133
10-1 Expected and observed number of events for the $t\bar{t}$ events	138

LIST OF FIGURES

<u>Figure</u>	<u>page</u>
1-1 Leading order diagram for $t\bar{t}$ production via quark-antiquark annihilation	34
1-2 Leading order diagrams for $t\bar{t}$ production via gluon-gluon fusion.	34
1-3 Cross-section of $t\bar{t}$ pair production as a function of center-of-mass energy	35
1-4 Diagrams for the self-energies of W -boson and Z -boson	35
1-5 Constraint on the Higgs boson mass	36
1-6 Loop contributions to the Higgs boson propagator	36
1-7 Experimental constraints on M_W and M_{top}	37
2-1 Diagram of the Tevatron accelerator complex	46
2-2 Elevation view of the East hall of the CDF detector	46
2-3 Schematic of tracking volume and plug calorimeters	47
2-4 Initial instantaneous luminosity and total integrated luminosity in Run II	47
2-5 Schematic view of the Run II CDF silicon tracking system.	48
2-6 East end-plate slots Sense and field planes in COT	48
2-7 Cross section of upper part of new end plug calorimeter.	49
2-8 Configuration of steel, chambers and counters for the CMU detector	49
2-9 Readout functional block diagram in Run II.	50
3-1 Jets correction factor as a function of η	63
3-2 Average transverse energy as a function of the number of primary vertices in the event	64
3-3 Absolute jet energy scale corrections for jets with cone size of 0.4	64
3-4 Fractional systematic uncertainty due to underlying event	65
3-5 Jet corrections due to out-of-cone effect for jets	65
3-6 Schematic view of an event containing a jet with a secondary vertex.	66
3-7 Jet probability distribution for prompt, charm and bottom jets.	66
3-8 Signed impact parameter distribution	67
4-1 Tree level Feynman diagram for the process $u\bar{u} \rightarrow t\bar{t}$	85

4-2	Tree level Feynman diagram for the process $u\bar{u} \rightarrow t\bar{t} \rightarrow b\bar{b}u\bar{u}d\bar{d}$	86
4-3	Cross section for $t\bar{t}$ production versus the top mass, from CompHep	87
4-4	Transverse momentum of the $t\bar{t}$ events	88
4-5	Mass reconstruction using smeared parton energies	88
4-6	Mass reconstruction using jets matched to partons	89
4-7	Reconstructed top mass versus input top mass using realistic jets.	90
5-1	Minimum of the negative log event probability	95
6-1	Background validation in control region 1 for single tagged events	100
6-2	Background validation in control region 1 for double tagged events	101
6-3	Sum of event probabilities calculated for for background samples.	101
6-4	Dijet invariant mass of the untagged jets for background before the cut on the signal-like probability	102
6-5	Dijet invariant mass of the untagged jets for background samples after the cut on the signal-like probability	102
6-6	Event by event most probable top mass distributions for background samples after the signal-like probability cut	103
6-7	Effect of the background contamination in the top mass reconstruction using only the matrix element technique.	103
7-1	Top templates for $t\bar{t}$ events.	111
7-2	Top templates for background events	111
7-3	Dijet mass templates for $t\bar{t}$ events.	111
7-4	Dijet mass templates for background events	113
8-1	Raw reconstruction in the JES versus Top Mass plane	120
8-2	Reconstructed top mass versus input top mass, for input JES equal to 0.	120
8-3	Reconstructed JES versus input JES, for input top mass equal to 170 GeV.	120
8-4	Slope of the mass calibration curve versus input JES.	121
8-5	Constant of the mass calibration curve versus input JES.	121
8-6	Slope of the JES calibration curve versus input JES.	121
8-7	Constant of the JES calibration curve versus input JES.	121

8-8	Mass pull means versus input top mass, for input JES equal to 0.	122
8-9	Mass pull widths versus input top mass, for input JES equal to 0.	122
8-10	Average of mass pull means versus input JES.	122
8-11	Average of mass pull widths versus input JES.	122
8-12	JES pull means versus input top mass, for input top mass equal to 170 GeV. . .	123
8-13	JES pull widths versus input top mass, for input top mass equal to 170 GeV. . .	123
8-14	Average of JES pull means versus input top mass.	123
8-15	Average of JES pull widths versus input top mass.	123
8-16	Corrected reconstruction in the JES versus Top Mass plane	124
8-17	Slope of the M_{top} calibration curve versus true JES after the 2D correction. . . .	125
8-18	Intercept of the M_{top} calibration curve versus true JES after the 2D correction. .	125
8-19	Slope of the JES calibration curve versus true M_{top} after the 2D correction. . . .	125
8-20	Intercept of the JES calibration curve versus true M_{top} after the 2D correction. .	125
8-21	Mass reconstruction using blind mass samples	125
8-22	JES reconstruction using blind JES samples	125
8-23	Expected uncertainty on top mass versus input top mass	126
8-24	Expected uncertainty on JES versus input JES	126
9-1	Event multiplicity for background events	132
9-2	Parameters of the top mass template for single tagged background events	133
9-3	Parameters of the top mass template for double tagged background events	134
9-4	Top mass pull mean as a function of M_{top} considering the correlation between the event top mass and the dijet mass	134
9-5	Top mass pull width as a function of M_{top} considering the correlation between the event top mass and the dijet mass.	135
10-1	Event reconstructed top mass in the data	138
10-2	Contours of the mass and JES reconstruction in the data	139
10-3	Expected statistical uncertainty from Monte Carlo	139
10-4	Most precise top mass results at Fermilab	140

A-1	Shapes for the PDF distributions used in the matrix element calculation	141
B-1	Transverse momentum of the $t\bar{t}$ system for different generators and top masses. .	142
C-1	Transfer functions for the W -boson decay partons	143
C-2	Transfer functions for the b -quark partons	146
D-1	Top templates for $t\bar{t}$ single tagged events	149
D-2	Top templates for $t\bar{t}$ double tagged events	156
E-1	Dijet mass templates for $t\bar{t}$ single tagged events	163
E-2	Dijet mass templates for $t\bar{t}$ double tagged events	170

Abstract of Dissertation Presented to the Graduate School
of the University of Florida in Partial Fulfillment of the
Requirements for the Degree of Doctor of Philosophy

MEASUREMENT OF THE TOP QUARK MASS IN THE ALL
HADRONIC CHANNEL AT THE TEVATRON

By

Gheorghe Lungu

August 2007

Chair: Jacobo Konigsberg

Major: Physics

This study presents a measurement of the top quark mass in the all hadronic channel of the top quark pair production mechanism, using 1 fb^{-1} of $p\bar{p}$ collisions at $\sqrt{s}=1.96 \text{ TeV}$ collected at the Collider Detector at Fermilab (CDF). Few novel techniques have been used in this measurement. A template technique was used to simultaneously determine the mass of the top quark and the energy scale of the jets. Two sets of distributions have been parameterized as a function of the top quark mass and jet energy scale. One set of distributions is built from the event-by-event reconstructed top masses, determined using the Standard Model matrix element for the $t\bar{t}$ all hadronic process. This set is sensitive to changes in the value of the top quark mass. The other set of distributions is sensitive to changes in the scale of jet energies and is built from the invariant mass of pairs of light flavor jets, providing an in situ calibration of the jet energy scale. The energy scale of the measured jets in the final state is expressed in units of its uncertainty, σ_c . The measured mass of the top quark is $171.1 \pm 3.7(\text{stat.unc.}) \pm 2.1(\text{syst.unc.}) \text{ GeV}/c^2$ and to the date represents the most precise mass measurement in the all hadronic channel and third best overall.

CHAPTER 1 INTRODUCTION

1.1 History of Particle Physics

At the end of the 19th century, the scientists were convinced that matter is made up by atoms. The atomic theory has been first conjectured by ancient Greek philosophers like Leucippus, Democritus, and Epicurus, then later indicated by Dalton's chemistry experiments. One of the philosophical motivations behind this theory was the reductionist desire to explain the diversity of matter by the existence of few fundamental and indivisible particles.

The atoms were thought to be these fundamental particles, but an uncomfortably large number of different atoms have been identified. Moreover, some experiments were showing evidence that the atoms are not indivisible. By 1897, Thomson discovered the electrons and measured its charge to mass ratio. Also he proposed his plum-pudding model of the atom, where the electrons are small, negatively charged and distributed inside the massive, positively charged atom. It was already known that some atoms decay spontaneously producing three types of radiations: α -rays, bent slightly by a magnetic field, β -rays, bent significantly in a magnetic field, and γ -rays, not affected by the magnetic field. Therefore the atoms were no longer seen as fundamental.

In 1900, studying the radiation of the black body, Planck determined that the power of light emitted by matter is a multiple of a fundamental quantum of energy. At a given frequency of the light ν , the minimum quantum of energy is $h\nu$. He introduced the constant $h=6.625\times 10^{-34}$ Js, which is one of the most important constants of the quantum theory. Later in 1905, Einstein's explanation of the photoelectric effect confirmed the quantum theory of light and then in 1923 Compton's experiment settled in the photon as particle of light.

Back in 1909, Rutherford concluded following the scattering of α -particles off gold atoms that Thomson's atom is not realistic and that the positive charge and almost all

mass is concentrated in a nucleus with the electrons orbiting around it. Several years later in 1918, following a different scattering experiment with α -particles, he will conclude that the hydrogen nucleus is an elementary particle and it is present inside the nucleus of every atom. This new particle was later called proton. While the proton was able to explain the charge of the nucleus, it couldn't explain the mass of heavier atoms. Rutherford believed that a neutral particle he called neutron exists, but this was confirmed experimentally only in 1932 by Chadwick.

Rutherford's atom was not a satisfactory model. The electron going around the nucleus would be accelerated centripetally and therefore should emit electromagnetic radiation according to the classical theory of electromagnetism. The loss of energy through radiation should make the electron collapse on the nucleus rendering Rutherford's atom unstable. In 1913, Bohr will propose a different model for the atom in which the electrons sit on orbits with discrete values of the orbital angular momentum. The electron can move from one orbit to another by releasing or receiving a photon with an energy equal to the energy difference between the orbits. This model will receive support from the Franck-Hertz experiment where it was observed that the atoms can absorb only specific amounts of photons.

Bohr's atom was still not explaining several experimental observations like the splitting of the atomic spectral lines (Zeeman effect) or the splitting of a beam of electrons when passing a magnetic field (Stern-Gerlach experiment). To explain this, in 1925, Uhlenbeck and Goudsmit proposed that the electron spins on its axis as it orbits around the nucleus. Soon Pauli introduced the exclusion principle stating that two particles can occupy a state defined by the same quantum numbers explaining why the electrons were spread overall several orbits.

In 1924, De Broglie extended the particle-wave duality from photons to any particle such as the electron. The wavelike character of the electron was observed in 1927 in a diffractive experiment by Davisson and Germer. Based on this idea, Schrodinger

formulated his famous matter wave equation predicting precisely the energies levels of the electron in a hydrogen atom. Simultaneously, Heisenberg introduced the uncertainty principle which helped explain the concept of matter as both waves and particles. This constitutes the starting point of the quantum mechanics.

The quantum theory developed by Schrodinger and Heisenberg wasn't incorporating the special relativity theory and the spin of the electron. This problem was solved by Dirac by writing the appropriate equation which could also explain the fine splitting and hyperfine splitting of energy levels within the hydrogen atom. The Dirac equation also predicted the existence of negative energy states which lead to the prediction of antiparticles. This surprising prediction was validated in 1931 by Anderson who discovered the positron, the anti-particle of the electron. Later in 1955, the antiproton was discovered and a year later the antineutron.

Besides the gravitational force and the electromagnetic force which were known at that time, a new force was introduced which will bind the protons and the neutrons inside the nucleus. This force was called the strong force and in 1935 Yukawa believed it is mediated by a massive particle called pion, denoted by π . To account for all possible interactions between the nucleons it was expected that the pion exists in three charge states: positive, neutral and negative. In 1937, Anderson observed a new particle, but it wasn't exhibiting the expected properties of the pion. Therefore the scientists decided that the new particle wasn't the pion, but a different new particle they called the muon, denoted μ .

Studying the β decay of nuclei, the scientists concluded that it was due to either neutron decay or proton decay. While it was found that the proton decays only if stimulated, the neutron was decaying spontaneously with a half-time of about 10 minutes. This period couldn't be associated to strong force or the electromagnetic force. So a new force was introduced to explain the process and they called it the weak force. The neutron decays into a proton and an electron. The spectrum of the electron energy led Pauli

in 1930 to postulate the existence of a new particle which Fermi called neutrino. This particle was discovered in 1956 by Reines.

Eventually, in 1947, Powell, Lattes and Occhialini discovered the charged pions, while the neutral pion was discovered later in 1950. However, in about the same time with the pion discovery other new strongly interacting particles were observed, the kaons and the hyperons. They were generically called strange particles because they were unexpected and they seemed to be produced via strong interaction, but decay via the weak interaction. Attempting to classify the strongly interacting particles, in 1964 Gell-Mann and Zweig introduced the quark model containing three varieties of quarks: up, down and strange. All the known particles are either mesons where two quarks are combined or baryons where three quarks are combined. This was not a totally new idea because between 1953 and 1957 scattering of electrons off nuclei revealed a charge density distribution inside the protons and the neutrons. Later in 1968, Feynman and Bjorken made the same observation in an experiment at Stanford Linear Accelerator where electrons were collided with protons.

The decay of the strange kaons led Lee and Yang in 1956 to propose that the weak interaction doesn't conserve parity. Later that year Wu observed this feature in the decay of the cobalt. This discovery shocked the scientific community as much as the corpuscular theory of light did in the past. Following this property of the weak interaction, it was expected that the electron and the neutrino have preferred polarizations. In 1957, Fraunfelder determined that the electron is left-handed and in 1958 Goldhaber showed that the neutrino is left-handed as well. Studying the spins of the electrons emitted in the muon decays, it was discovered that the charge conjugation symmetry is also violated by the weak interaction. It was believed though that the CP symmetry is preserved by the weak interaction. However, in 1964, Christenson, Cronin, Fitch and Turlay showed that the kaon decay doesn't preserve this symmetry either. The CP violation of the weak

interaction was not understood until later. However, the CP conservation by the strong force remains a mystery.

Another thing that puzzled the physicists was why the decay of the muon into an electron and a photon was not observed. The solution adopted was the postulation of two types of neutrinos, the electron-neutrino and the muon-neutrino, along with the conservation of two new quantum numbers, the electron number and the muon number. The muon-neutrino was eventually discovered in 1962 by Lederman, Schwarts and Steinberger.

Through the work of Feynman in 1947, the physicists were able to calculate the electromagnetic properties of the electron, positron and the photon using the Feynman diagrams. This constitutes the birth of quantum electrodynamics, or QED.

The theory of weak interaction was first formulated by Fermi in 1933 and it was assuming a four-fermion interaction acting at a single point. The Fermi coupling constant $G_F = 1.16639 \times 10^{-5} \text{ GeV}^{-2}$ was giving the strength of the weak interaction. In 1956, Feynman and Gell-Mann incorporated the phenomenon of parity violation into this theory. The Fermi theory of weak interaction was able to explain the low-energy processes, but was making unacceptable prediction for high-energy weak interactions. The solution to this problem was to introduce a particle which mediates the weak interaction. This particle was thought to be a spin 1 boson, with three charge states, W^- , W^0 , W^+ and was the result of work done by Schwinger, Bludman and Glashow in 1959. Later in 1967 Weinberg and Salam propose a theory that unifies the weak and the electromagnetic forces. In this theory the neutral boson carrying the weak force is called Z^0 . In addition to that a massive boson called the Higgs boson is predicted. The W and Z bosons will be eventually discovered in 1983 at CERN in according to the predictions.

In 1964 the fundamental particles were: three quarks - up (u), down (d) and strange (s), and two pairs of leptons - the electron (e) with its neutrino (ν_e), and the muon (μ) with its neutrino (ν_μ). Their corresponding antiparticles were also considered as

fundamental. Observing the pattern of the leptons many physicists started believing in the existence of a fourth quark, called charm (c). In 1970 Glashow, Iliopoulos and Maiani proposed a mechanism through which the weak theory will allow flavor-conserving Z^0 -mediated weak interactions. This mechanism was requiring the existence of a fourth quark. Later in 1973, at CERN, Perkins found evidence of weak interactions with no charge exchange. The existence of charm was confirmed in 1974 by Richter and Ting who found a charm-anticharm meson called J/Ψ , and then reconfirmed in 1976 by Goldhaber and Pierre who found a charm-antiup meson called D^0 .

A quantum field theory of strong interaction is formulated in 1973 by Fritzsche and Gell-Mann. They introduce the gluon (g) as a massless quanta of the strong force. This theory of quarks and gluons is similar in structure to QED, but since strong interaction deals with color charge this theory is called quantum chromodynamics, or QCD. The color charge was a concept introduced earlier in 1963 by Greenberg, Han and Nambu. The hadrons made of quarks were considered color neutral. In 1973, Politzer, Gross and Wilczek discover that at short distances the strong force was vanishing. This special property was called asymptotic freedom. In 1979, a strong evidence for a gluon radiated by a quark is found at DESY, in Hamburg, Germany.

In 1976, another unexpected particle is discovered. This new particle seen by Perl at SLAC was the tau lepton, denoted τ , and it was the first particle of the third generation. In 1977, the existence of a third generation was confirmed by Lederman at Fermilab by discovering a new quark, called bottom (b). In 1989, the experiments at SLAC and CERN strongly supported the hypothesis of only three generations of fundamental particles by measuring the lifetime of Z^0 -boson. Later in 1995 at Fermilab the remaining quark of the third generation is discovered. This is called the top quark (t) and it has mass much larger than the other quarks. Also at Fermilab the third generation is completed by the discovery of the tau neutrino (ν_τ) in 2000.

All the discoveries described above led to the formulation of a theory that summarizes the current knowledge of the fundamental particles and the interactions between them. This theory is called the Standard Model of particle physics and it will be described in more detail in the next section.

1.2 The Standard Model

The Standard Model of particle physics is a theory which describes three of the four known fundamental interactions between the elementary particles that make up all matter. It is a quantum field theory which is consistent with both quantum mechanics and special relativity. To date, almost all experimental tests of the three forces described by the Standard Model have agreed with its predictions. However, the Standard Model falls short of being a complete theory of fundamental interactions, primarily because of its lack of inclusion of gravity, the fourth known fundamental interaction, but also because of the large number of numerical parameters (such as masses and coupling constants) that must be put "by hand" into the theory (rather than being derived from first principles).

The matter particles described by the Standard Model all have an intrinsic spin whose value is determined to be $1/2$, making them fermions. For this reason, they follow the Pauli exclusion principle in accordance with the spin-statistics theorem giving them their material quality. Apart from their antiparticle partners, a total of twelve different types of matter particles are known and accounted for by the Standard Model. Six of these are classified as quarks (up, down, strange, charm, top and bottom), and the other six as leptons (electron, muon, tau, and their corresponding neutrinos).

Each quark carries any one of three color charges - red, green or blue, enabling them to participate in strong interactions. The up-type quarks (up, charm, and top quarks) carry an electric charge of $+2/3$, and the down-type quarks (down, strange, and bottom) carry an electric charge of $-1/3$, enabling both types to participate in electromagnetic interactions.

Leptons do not carry any color charge - they are color neutral, preventing them from participating in strong interactions. The down-type leptons (the electron, the muon, and the tau lepton) carry an electric charge of -1, enabling them to participate in electromagnetic interactions. The up-type leptons (the neutrinos) carry no electric charge, preventing them from participating in electromagnetic interactions.

Both quarks and leptons carry a handful of flavor charges, including the weak isospin, enabling all particles to interact via the weak nuclear interaction. Pairs from each group (one up-type quark, one down-type quarks, a lepton and its corresponding neutrino) form a generation. Corresponding particles between each generation are identical to each other apart from their masses and flavors (Table 1-1). The force-mediating particles described by the Standard Model all have an intrinsic spin whose value is 1, making them bosons (Table 1-2). As a result, they do not follow the Pauli Exclusion Principle.

The photons mediate the familiar electromagnetic force between electrically charged particles (these are the quarks, electrons, muons, tau, W -boson). They are massless and are described by the theory of quantum electrodynamics. The W and Z gauge bosons mediate the weak nuclear interactions between particles of different flavors (all quarks and leptons). They are massive, with the Z -boson being more massive than the W -boson.

An interesting feature of the weak force is that interactions involving the W gauge bosons act on exclusively left-handed particles. The right-handed particles are completely neutral to the W bosons. Furthermore, the W -bosons carry an electric charge of +1 and -1 making those susceptible to electromagnetic interactions. The electrically neutral Z -boson acts on particles of both chiralities, but preferentially on left-handed ones. The weak nuclear interaction is unique in that it is the only one that selectively acts on particles of different chiralities; the photons of electromagnetism and the gluons of the strong force act on particles without such prejudice. These three gauge bosons along with the photons are grouped together which collectively mediate the electroweak interactions.

There are no mass terms for the fermions. Everything else will come through the scalar (Higgs) sector. The eight gluons mediate the strong nuclear interactions between color charged particles (the quarks). They are massless. But, each of the eight carry combinations of color and an anticolor charge enabling them to interact among themselves. The gluons and their interactions are described by the theory of quantum chromodynamics. Leptons carry no color charge; quarks do. Moreover, the quarks have only vector couplings to the gluons, ie, the two helicities are treated on par in this part of the standard model.

The Higgs particle described by the Standard Model has no intrinsic spin, and thus is also classified as a boson. As of early 2007 there have been indications of particles at the predicted mass of the Higgs boson found by the Tevatron at Fermilab; the significance level of these indications is however not high enough to warrant it being confirmed as the Higgs particle. It is hoped that upon the completion of the Large Hadron Collider, experiments conducted at CERN would bring experimental evidence confirming the existence for the particle. The Higgs boson plays a unique role in the Standard Model.

The Standard Model predicted the existence of W and Z bosons, the gluon, the top quark and the charm quark before these particles had been observed. Their predicted properties were experimentally confirmed with good precision. The Large Electron-Positron collider at CERN tested various predictions about the decay of Z bosons, and found them confirmed.

1.3 Top Quark Physics

The first observations of the top quark were reported twelve years ago by the CDF and D0 experiments [1]. The discovery of the top quark was not a surprise. Indeed, the existence of an isospin partner for the b -quark is strongly motivated by arguments of theoretical consistency of the Standard Model, absence of flavor changing neutral current in B meson decays and studies of Z boson decays [2]. However, the large mass of the top quark, nearly $175 \text{ GeV}/c^2$, was in itself a surprise at the time. In this regard, the top

quark separates itself from all other quarks. For example, it is the most massive fermion by a factor of nearly 40 (the bottom being the closest competitor).

Interestingly, even though the top quark is the most recent quark observed, its mass is the best known of all quarks. This is because it has such a short lifetime that it decays before any hadronization effects can occur. We should not be satisfied with this relative success and a more accurate determination of M_{top} is strongly motivated inside and beyond the SM.

The top quark is the weak isospin partner of the b -quark in the Standard Model. As such, it carries the following quantum numbers: an electric charge $+2/3$, an intrinsic spin of $1/2$ and a color charge associated with the strong force. Due to the relatively small data sample collected in Run I of the Tevatron, none of these assignments have been measured directly. However, strong indirect evidence exists. First, the precision electroweak data of Z boson decay properties requires the existence of an isospin partner of the b -quark with electric charge $+2/3$ and a large mass. Furthermore, the predicted rate of top quark pair production, which is very sensitive to the spin and strong coupling of the top quark, is in good agreement with the data [3] [4] [5] [6]. Therefore, current observations lead us to believe that the particle observed at the Tevatron is indeed the top quark. However, direct measurements are still desirable and will be attempted in the case of the electric charge and spin using data from the Run II of the Tevatron or the LHC [7].

The other intrinsic properties of an elementary particle are its mass and lifetime. The most precise knowledge of the mass comes from direct measurements. The current world average containing only measurements performed during Run I at the Tevatron is $178 \pm 4.3 \text{ GeV}/c^2$. In quantum mechanics, the lifetime of a particle is related to its natural width through the relationship $\tau = \hbar/\Gamma$. The branching ratio for the electroweak top quark decay $t \rightarrow Wb$ is far larger than any other decay mode and thus its full width can be approximately calculated from the partial width $\Gamma(t \rightarrow Wb)$. Assuming $M_W = M_b = 0$, the lowest order calculation of the partial width has the expression shown in Equation 1-1,

where G_F is the Fermi constant and V_{tb} is the Cabibbo-Kobayashi-Maskawa (CKM) matrix element linking the top and bottom quarks.

$$\Gamma_0(t \rightarrow Wb) = \frac{G_F M_{top}^2 |V_{tb}|^2}{8\pi\sqrt{2}} = 1.76 \text{ GeV}, \quad (1-1)$$

This simplified picture illustrates that the width is driven by the square of M_{top} . More sophisticated calculations result in negative corrections of about 20%, the final result being 1.42 GeV with theoretical uncertainties less than 1%. This results in a lifetime for the top quark of approximately 4×10^{-25} s. This is about an order of magnitude lower than the characteristic time for QCD effects to take place. Therefore, due to its very large mass, the top quark will not form hadrons before it decays. This property makes the top quark the only quark without hadron spectroscopy (i.e., where we can expect meson or baryon states including a top quark). In addition, the short lifetime facilitates the measurement of top quark properties since the information about the bare quark is directly reflected by the decay products.

The top quark is produced predominantly in $t\bar{t}$ pairs at the Tevatron via the strong interaction. At a center-of-mass energy of 1.96 TeV, the process $q\bar{q} \rightarrow t\bar{t}$ and $gg \rightarrow t\bar{t}$ occur approximately 85% and 15% of the time, respectively. The leading order diagrams for the two processes are shown in Figure 1-1 and in Figure 1-2. Calculations of the total $t\bar{t}$ cross-sections $\sigma(t\bar{t})$ have been performed up to the next-to-leading order (NLO) in the coupling constant of the strong force (α_s). The theoretical value at a center-of-mass energy of 1.96 TeV [8] is shown in Equation 1-2 for $M_{top} = 175 \text{ GeV}/c^2$.

$$\sigma_{th}(t\bar{t}) = 6.7_{-0.9}^{+0.7} \text{ pb}, \quad (1-2)$$

Since the typical partonic center-of-mass energy available at the Tevatron is still relatively close to the $t\bar{t}$ threshold production, (for example the average velocity of the produced top quarks is $\beta \approx 0.5$), the cross-section displays significant dependence on M_{top} . This is illustrated in Figure 1-3 where we show $\sigma(t\bar{t})$ as a function of the center-of-mass

energy for various values of M_{top} . The theoretical calculations are in good agreement with the measurements performed at 1.8 TeV (Run I) [3] [4] and 1.96 TeV (Run II) [5] [6].

Figure 1-3 illustrates one motivation to measure accurately M_{top} : the knowledge of the top quark mass is necessary to compare as precisely as possible the theoretical predictions and measurements of the $t\bar{t}$ cross-section. An eventual discrepancy could be a sign of new physics as discussed in more detail in [7].

The electroweak production of single top quarks is also predicted by the Standard Model but has not been observed to date [9] [10]. The production cross-section is predicted to be smaller than for $t\bar{t}$ (≈ 2.4 pb) and the experimental signature suffers from much larger background contamination.

The top quark decay is mediated by the electroweak interaction. Since flavor changing neutral currents are forbidden in the Standard Model due to the GIM mechanism [11], the decays of the top quark involving Z or γ bosons in the final state (e.g., $t \rightarrow Zc$) are highly suppressed and can only occur through higher order diagrams. Therefore, the top quark decay vertex must include a W boson. Three possible final states exist: $t \rightarrow Wb$, $t \rightarrow Ws$ and $t \rightarrow Wd$. As illustrated in Equation 1-1, the partial width of charged current top decays is proportional to the square of the corresponding CKM matrix element. Assuming a Standard Model with three families, the relevant CKM matrix elements have the constraints [12] given in Equation 1-3.

$$\begin{aligned} 0.0048 &< |V_{td}| < 0.014, \\ 0.037 &< |V_{ts}| < 0.043, \\ 0.9990 &< |V_{tb}| < 0.9992. \end{aligned} \tag{1-3}$$

Therefore, the decay $t \rightarrow Wb$ is completely dominant and its predicted branching ratio is $BR(t \rightarrow Wb) > 99.8\%$. Hence only $t \rightarrow Wb$ decays have been considered in the identification of top quarks, though searches for other decay modes have been undertaken [13]. We note that the W boson from the top quark decay is real (i.e., its mass

corresponds to the measured mass $M_W \approx 80.4 \text{ GeV}/c^2$), given that $M_{top} > M_W + M_b$. This is an important characteristic of $t\bar{t}$ events that is exploited in this analysis in the reconstruction of the top quark mass and the W boson mass. The W boson will in turn decay to two quarks about 2/3 of the time and a charged lepton associated with a neutrino about 1/3 of the time.

The experimental signature of top quarks thus emerge. They are produced as $t\bar{t}$ pairs, each one decaying immediately to a real W boson and a b -quark, the latter hadronizing to form a b -jet. The resulting W decay defines the $t\bar{t}$ final state: There can be two hadronic decays (all-hadronic channel), one leptonic and one hadronic decay (lepton + jets channel), and two leptonic decays (dilepton channel), where the leptonic decays considered are usually only to electrons and muons (with their associated neutrinos) due to the experimental difficulty of identifying tau leptons. The approximate branching ratios for each channel are given in Table 1-3.

The top quark plays a central role in the predictions of many SM observables by contributing to their radiative corrections. Good examples are the W and Z boson propagators, in which loops involving top quarks are expected to strongly contribute, as illustrated in Figure 1-4. These diagrams can exist for any type of quark or lepton, but the very large value of M_{top} makes the top quark contribution dominant. To illustrate the effect of the top quark, we consider in Equation 1-4 the theoretical calculation of the W boson mass [12].

$$M_W^2 = \frac{\pi\alpha}{\sqrt{2}G_F \sin^2\theta_W} \frac{1}{1 - \Delta r}, \quad (1-4)$$

α is the fine structure constant, θ_W is the Weinberg angle and Δr contains the radiative corrections and is approximately given by Equation 1-5.

$$\Delta r \approx \Delta r_0 - \frac{\Delta\rho}{\tan^2\theta_W} \quad (1-5)$$

The term Δr_0 is due to the running of α . The term $\Delta\rho$ is due to the one-loop top quark correction to W -boson propagators shown in Figure 1-4, and is given by Equation 1-6.

$$\Delta\rho = \frac{3G_F M_{top}^2}{8\sqrt{2}\pi^2} \quad (1-6)$$

The uncertainty on the Fermi constant G_F is completely negligible with respect to the one on the top quark mass in the computation of $\Delta\rho$. The term Δr_0 and the Weinberg angle in Equation 1-5 are known to a precision of 0.2%. The uncertainty on the top quark mass is currently about an order of magnitude larger than the other uncertainties and moreover it contributes quadratically to Δr . Thus the precision on M_{top} is currently the limiting factor in the theoretical prediction of the W boson mass. The parameter $\Delta\rho$ is qualified as “universal” in the literature because it enters in the calculation of many other electroweak observable like $\sin\theta_W$ and the ratio of the production of b -quark hadrons of all types (usually denoted R_b), to name a few. Therefore, the top quark mass plays a central role in the interplay between theoretical predictions and experimental observables that aims to test consistency of the SM.

One consistency check is to compare the measured value of M_{top} with the predicted value from SM precision observables (excluding of course direct measurements of M_{top}). The indirect constraints, inferred from the effect of top quark radiative corrections, yields $M_{top} = 181_{-9}^{+12}$ GeV/c² [14]. The relatively small uncertainty is achieved because of the large dependence of M_{top} on many electroweak observables. This is in remarkable agreement with the Run I world average of $M_{top} = 178 \pm 4.3$ GeV/c² [15], and is considered a success of the SM.

A similar procedure can be used to constrain the Higgs boson mass (M_H), the last particle in the SM that has yet to be observed. The only direct information on M_H is a lower bound obtained from searches at LEP-II: $M_H > 114$ GeV/c² at 95% confidence level [16]. Indirect constraints on M_H can be obtained with precise measurements of

M_W and M_{top} . Indeed, the correction to the W boson mass Δr given in Equation 1-4 contains additional terms due to Higgs boson loops. These corrections depend only logarithmically on M_H and have thus weaker dependence on M_H than on M_{top} . Still, precise determination of M_{top} and M_W can be used to obtain meaningful constraints on M_H as illustrated in Figure 1-5. Numerically, the constraints are [14] made explicit in Equations 1-7 and 1-8.

$$M_H = 126^{+73}_{-48} \text{ GeV}/c^2 \quad (1-7)$$

$$M_H < 280 \text{ GeV}/c^2 \text{ at } 95\% \text{ C.L.}, \quad (1-8)$$

Only the top quark mass measurements from Run I have been used. Such constraints on M_H can help direct future searches at the Tevatron and LHC and constitutes another stringent test of the Standard Model when compared to limits from direct searches or mass measurements from an eventual discovery.

Even though the Standard Model successfully describes experimental data up to a few hundred GeV, it is believed that new physics must come into play at some greater energy scale. At the very least, gravity effects are expected at the Planck scale ($\approx 10^{19}$ GeV) that the SM ignores in its current form.

The SM can thus be thought of as an effective theory with some unknown new physics existing at higher energy scale. A link exists between the new physics and the SM that manifests itself through radiative corrections to SM particles. The Higgs boson sector is the most sensitive to loops of new physics. For example the Higgs boson mass corrections from fermion loops shown in diagram (a) of Figure 1-6 are given by Equation 1-9, where m_f is the fermion mass and Λ is the “cut-off” scale used to regulate the loop integral.

$$\Delta M_H = 2\Lambda^2 + 6m_f^2 \ln(\Lambda/m_f) + \dots, \quad (1-9)$$

The parameter Λ can be interpreted as the scale for new physics that typically corresponds to the scale of the Grand Unified Theory (GUT) near 10^{16} GeV. This is a

problem for the SM, since on the one hand the Higgs boson mass receives corrections of the order of $100 \text{ GeV}/c^2$ to give the correct mass to the SM electroweak gauge bosons. There is a discrepancy of 14 orders of magnitude between the targeted mass and the radiative corrections! This is known as the fine-tuning problem of the SM Higgs boson (or gauge hierarchy problem) and has occupied theoretical physicists for several decades. A few solutions have emerged from this work, all of them manifesting themselves near the scale of the origin of mass near 1 TeV (or electroweak symmetry breaking scale).

The top quark, with its large mass of nearly 0.2 TeV, could be more closely connected to new physics than any other SM particle. One interesting numerological argument suggests the top quark is indeed a special case. Its Yukawa coupling (y_t) (i.e., its coupling to the Higgs field), is approximately equal to unity as shown in Equation 1–10, where v is the vacuum expectation value of the Higgs field that is known from properties of the weak interaction to be approximately 171 GeV.

$$y_t = \sqrt{2} \frac{M_{top}}{v} \approx 1, \tag{1-10}$$

This could be a coincidence, or it could be a sign that the top quark mass is related to the mechanism of the origin of mass that physics beyond the SM must explain, as suggested above. In this respect, the top quark mass could turn out to be a more fundamental parameter of nature. For these reasons, albeit somewhat hypothetical, a precise measurement of M_{top} would certainly be desirable for the understanding of any theory.

One example of a new physics model is Supersymmetry (SUSY), which constitutes an extension of the SM where the SM fermionic particles have associated bosonic particles and vice-versa. It is generally regarded as the favored option to extend or replace the SM at higher energies. Indeed, SUSY solves elegantly the gauge hierarchy problem since the fermion and boson partners cancel each other's divergent corrections to the Higgs boson mass proportional to Λ^2 (given in Equation 1–9 for fermionic particles). Moreover,

SUSY has other attractive features, such as providing a good candidate for dark matter, predicting the unification of the gauge coupling constants at the GUT scale and being required by the only consistent theory of quantum gravity currently available (superstring theory).

The top quark plays an important role in SUSY models. Indeed, the radiative corrections from SUSY particles to electroweak observables, which can be computed in a similar fashion as for the SM particles, are dominated by loops involving the top quark and its scalar partners, the stop quarks. This effect is especially apparent in the Higgs sector of SUSY models. Considering the simplest model of SUSY, the Minimum Supersymmetric Standard Model (MSSM), the one-loop correction to the lightest MSSM Higgs boson mass (M_h) is proportional to [17] as shown in Equation 1–11, where $M_{\tilde{t}_1}$ and $M_{\tilde{t}_2}$ are the masses of the lightest and the heaviest stop quarks, respectively.

$$\Delta M_h^2 \approx G_F M_{top}^4 \log\left(\frac{M_{\tilde{t}_1} M_{\tilde{t}_2}}{M_{top}^2}\right), \quad (1-11)$$

Thus the corrections to M_h depend quartically on M_{top} ! Therefore, the same conclusion as discussed previously for the SM is valid for SUSY (and even reinforced due to the stronger M_{top} dependence): high precision measurements of M_{top} will be crucial for the self-consistency check of the theory and determination of unknown parameters. For instance, the value of the top quark mass was crucial to determine the current upper bound of about 135 GeV/c² on the lightest MSSM Higgs boson mass [18].

Using the current measurements of precision observables, it is already possible to set meaningful constraints on SUSY. For example, Figure 1-7 shows the current measurements of M_{top} and M_W as well as the region allowed exclusively inside the MSSM (green), the SM (red) as well as an overlap region between the MSSM and SM (blue). As can be seen, the additional radiative corrections from SUSY particles are large enough such that the overlap region between SM and MSSM is small in the $M_{top} - M_W$ plane. The current experimental accuracies are not good enough to distinguish between the two theories, but

future prospects (e.g., black curve for Tevatron/LHC and red curve for the International Linear Collider (ILC)) demonstrates very good discriminating power. The radiative corrections from MSSM particles to the SM precision observables are discussed in more detail in [19].

Other alternatives to replace the SM at energies near the TeV scale are theories involving dynamical breaking of the electroweak symmetry [20]. These models, one well-known example being Technicolor [21], do not include an elementary Higgs boson, but rather give mass to the SM particles by introducing a new strong gauge interaction that produce condensates of fermions that act as Higgs bosons. In some versions of these models, denoted “topcolor”, the new gauge interaction acts only on the third generation, and the fermion condensates are made of top quarks [22]. Such a model could be discovered by looking for evidence of new particles in the $t\bar{t}$ invariant mass at the Tevatron or LHC.

1.4 Highlights of Mass Measurement

Now that the top quark was placed in the context of particle physics and of the Standard Model, the most successful theory describing it, we stop to outline the remaining of the study. In the following chapters a detailed analysis of the measurement of the mass of the quark will be presented.

The experimental apparatus used to produce and collect the data is described in broad details. This description is divided into a section dedicated to the accelerator of particles, Tevatron, and another for detailing the particle detector, the Collider Detector at Fermilab (CDF). Many techniques are used for the identification of particles separately for leptons, photons, quarks and gluons.

A more sophisticated tool involves the calculation of the matrix element for the process $u\bar{u} \rightarrow t\bar{t} \rightarrow b\bar{b}u\bar{u}d\bar{d}$ used in the computation of a probability to observe such process. This probability will be later used in the event selection and the in the mass

reconstruction. However, in the fourth chapter details of the matrix element calculation are offered as well as consistency checks.

The data samples and the Monte Carlo samples used in this study to determine the event selection used to enhance the $t\bar{t}$ content of the data sample. The achieved signal to background ratio is almost 1/1 and it will have a big impact in the value of the uncertainty on the mass. The modeling of the background processes is extracted from a data sample with small $t\bar{t}$ contribution.

The top quark mass reconstruction technique allows for the simultaneous determination of the top quark mass and of the scale of jet energies. The need for having the jet energy scale determined together with the top mass is to take into account the correlation between the two. As a consequence the effect of the jet energy scale on the uncertainty on the top mass is not double counted. This would be the case of a method where the top mass is determined separately from the jet energy scale but a systematic uncertainty due to the jet energy scale uncertainty has to be assigned. Moreover, in the bi-dimensional analysis the jet energy scale can be easily constrained and calibrated as it will be seen. The method briefly described above involves the full statistical treatment of the expected uncertainties. Also various systematic effects are described in detail and the corresponding uncertainty evaluated.

The mass measurement represented the best such measurement in the $t\bar{t}$ all hadronic channel. The treatment of the jet energy scale was one of the main improvements with respect to other mass measurements in this channel along with the use of the $t\bar{t}$ matrix element in the event selection and in the mass measurement technique itself. This measurement had a 11% weight in the world averaged top quark mass. Only two other measurements had a larger impact in the world average and those were done in the $t\bar{t}$ lepton+jets channel.

Table 1-1. Classification of the fundamental fermions in Standard Model. They are arranged in three generations.

Generation	Flavor	Mass (GeV/c ²)	Charge	Weak Isospin
I	Up (u)	0.003	$\frac{2}{3}$	$\frac{1}{2}$
	Down (d)	0.006	$-\frac{1}{3}$	$-\frac{1}{2}$
	e-Neutrino (ν_e)	$< 2 \times 10^{-6}$	0	$\frac{1}{2}$
	Electron (e)	0.0005	-1	$-\frac{1}{2}$
II	Charm (c)	1.5	$\frac{2}{3}$	$\frac{1}{2}$
	Strange (s)	0.1	$-\frac{1}{3}$	$-\frac{1}{2}$
	μ -Neutrino (ν_μ)	$< 2 \times 10^{-6}$	0	$\frac{1}{2}$
	Muon (μ)	0.1	-1	$-\frac{1}{2}$
III	Top (t)	171	$\frac{2}{3}$	$\frac{1}{2}$
	Bottom (b)	4.2	$-\frac{1}{3}$	$-\frac{1}{2}$
	τ -Neutrino (ν_τ)	$< 2 \times 10^{-6}$	0	$\frac{1}{2}$
	Tau (τ)	1.7	-1	$-\frac{1}{2}$

Table 1-2. Force carriers described in Standard Model.

Boson	Force	Mass (GeV/c ²)	Charge
Photon (γ)	EM	0	0
W^\pm	weak	80.4	± 1
Z^0	weak	91.2	0
Gluon (g)	strong	0	0

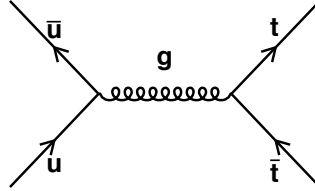


Figure 1-1. Leading order diagram for $t\bar{t}$ production via quark-antiquark annihilation. In this figure the incident quarks are the up -quarks.

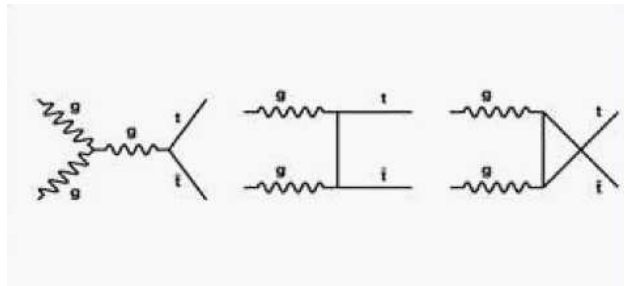


Figure 1-2. Leading order diagrams for $t\bar{t}$ production via gluon-gluon fusion.

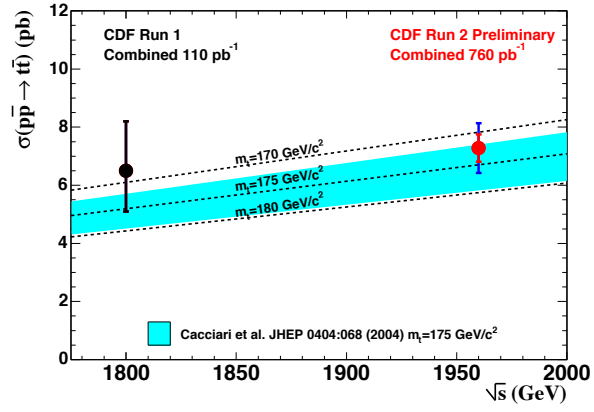


Figure 1-3. Cross-section of $t\bar{t}$ pair production as a function of center-of-mass energy for the theory prediction and CDF measurements.

Table 1-3. Branching ratios of the $t\bar{t}$ decay channels.

Channel	Branching Ratio
all-hadronic	44 %
lepton+jets	30 %
dilepton	5 %
tau lepton + X	21 %



Figure 1-4. Diagrams for the self-energies of W-boson and Z-boson where a loop involving the top quark is contributing.

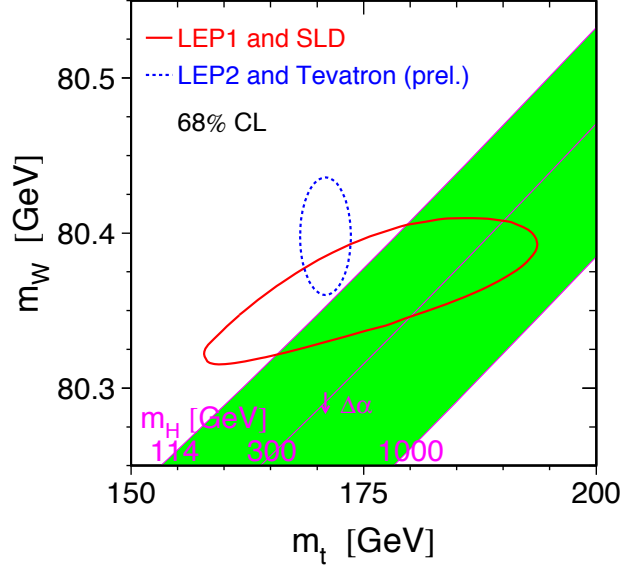


Figure 1-5. Constraint on the Higgs boson mass as a function of the top quark and W boson measured masses as of winter 2007. The full red curve shows the constraints (68% C.L.) coming from studies at the Z boson pole. The dashed blue curve shows constraints (68% C.L.) from precise measurement of M_W and M_{top} .

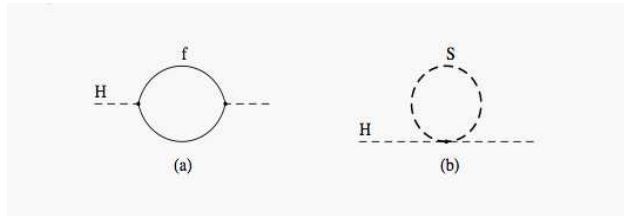


Figure 1-6. Loop contributions to the Higgs boson propagator from (a) fermionic and (b) scalar particles.

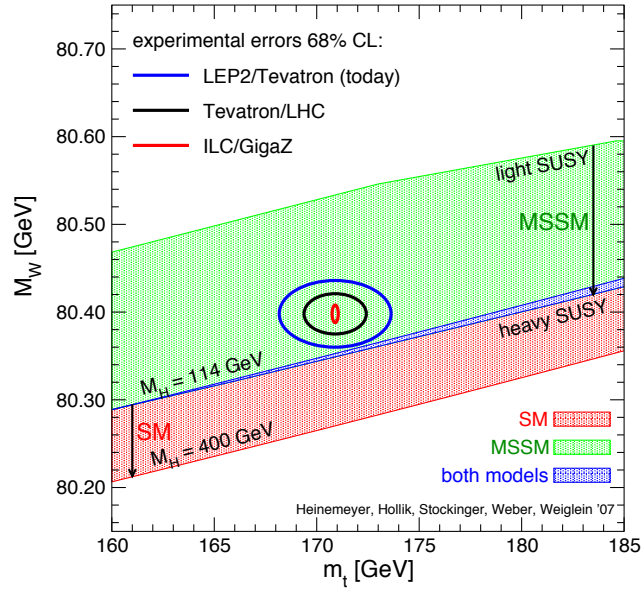


Figure 1-7. Experimental constraints on M_W and M_{top} (outer blue ellipse), the projected constraints at the end of the Tevatron and LHC (middle black ellipse) and at the ILC (red inner ellipse). Also shown are the allowed region for MSSM (green hatched), the SM (red cross-hatched) and the overlap region between the SM and MSSM (blue vertical lines).

CHAPTER 2

EXPERIMENTAL APPARATUS

The Fermi National Accelerator Laboratory (FNAL, Fermilab) has been running in its current phase of operation since 2001. Located near Batavia, IL, the $p\bar{p}$ synchrotron accelerator supports several experiments, including two collider detectors, one of which, the Collider Detector at Fermilab (CDF), collected data for this analysis. The accelerator also provides protons to fixed target experiments. CDF is a general purpose hard scattering detector supporting a wide variety of physics analyses. One of the priorities of FNAL is a precise measurement of the top quark mass. Several hundred people support the operation of the accelerator and another several hundred are responsible for the commissioning and operation of the CDF detector. A competing collaboration, D0, independently measures similar physics quantities. Combined results from these two collaborations have resulted in increasingly precise measurements of the top quark mass and other interesting physical phenomena. This chapter outlines the basic operation and structure of the accelerator and of the detector.

2.1 Tevatron Overview

The main accelerator at FNAL, the Tevatron, accelerates protons and antiprotons, colliding them at a center of mass energy of 1.96 TeV. Several stages of acceleration are necessary before protons and antiprotons can be brought to this energy. Since no readily available source of antiprotons exists, they must be produced using energetic proton collisions. Figure 2-1 schematically describes the Tevatron complex.

Protons colliding in the Tevatron start out as hydrogen gas. The hydrogen is ionized by adding an electron and then fed to a Cockroft-Walton direct current electrostatic accelerator. Exiting the Cockroft-Walton with 750 keV, the hydrogen ions are fed into a RF linear accelerator, the Linac, and ramped to 400 MeV. The hydrogen ions then strike a stationary target of carbon foil, stripping the two electrons from the ions and leaving bare protons.

Protons are collected and accelerated to 8 GeV in the Booster, a 475 m circumference synchrotron. The Booster then injects them into the Main Injector, a 3 km circumference synchrotron. The Main Injector has several purposes. It accelerates protons and antiprotons from 8 GeV to 150 GeV, preparing them for injection into the Tevatron; and it also accelerates protons to 120 GeV for antiproton production, as described later.

The Tevatron is a 6.3 km circumference synchrotron using superconducting magnets with a peak field of 4.2 T. Protons and antiprotons are injected into the Tevatron forming a beam containing 36 discrete packages of particles known as bunches and are accelerated from 150 to 980 GeV. Protons and antiprotons rotate in opposite directions in the ring and are held in separate helical orbits. Focusing quadrupole magnets at two collision points bring the proton and the antiproton beams to intersection. Bunches pass a given collision point every 396 ns. Each bunch collides approximately 2.6×10^{11} p and 3.5×10^{10} \bar{p} . These numbers contribute to the instantaneous luminosity of the beam [23] as shown in Equation 2-1.

$$\mathcal{L} = \frac{3\gamma f_o N_B N_p N_{\bar{p}} F}{\beta(\epsilon_p + \epsilon_{\bar{p}})}, \quad (2-1)$$

N_B is the number of bunches in the accelerator; N_p and $N_{\bar{p}}$ are the number of p and \bar{p} per bunch, respectively; f_o is the revolution frequency; $\gamma = E/m$ is the relativistic energy factor; β is the beta function at the low beta focus; ϵ_p and $\epsilon_{\bar{p}}$ are the proton and antiproton beam emittances, respectively; and F is a form factor describing bunch geometry. Integrating instantaneous luminosity over time and taking the product with a scattering cross-section returns the number of events produced.

Antiprotons are produced by colliding accelerated protons from the Main Injector with a stationary nickel target in the Target Station. Magnets focus charged particles from this collision into a beam and strip away everything but the antiprotons. Antiproton production is not very efficient, requiring a million incident protons to produce 20 antiprotons.

Once collected into a beam, the antiprotons are sent to the Debuncher, a triangular synchrotron with a radius of 90 m, where their spread in energy is reduced using a synchronized oscillating potential in the RF cavities. This potential is designed to accelerate slower particles and decelerate faster particles. Uniform velocities of antiprotons enables more efficient beam manipulation and increases instantaneous luminosity by reducing bunch widths.

Thus prepared, the antiprotons are collected and stored until they are needed for acceleration and collisions. One storage unit, the Accumulator, is a synchrotron in the same tunnel as the Debuncher, labeled “antiproton source” in Figure 2-1. The Accumulator reduces the longitudinal momentum of the antiprotons using a synchronized potential and stochastic cooling [24]. Stochastic cooling was developed at CERN in the 1970s and dampens unwanted momentum phase-space components of the particle beam using a feedback loop. Essentially, the beam orbit is measured with a pickup and corrected with a kicker.

The other antiproton storage unit is the Recycler, a synchrotron in the same ring as the Main Injector. The Recycler was originally designed to collect antiprotons from the Tevatron once collisions for a given store were finished, but attempts to use it for this purpose have not been worthwhile. As an additional storage unit, the Recycler has allowed increased instantaneous luminosity since 2004. The Recycler takes advantage of electron cooling, in which a 4.3 MeV beam of electrons over 20 m is used to reduce longitudinal momentum. When a store is ready to begin, antiprotons are transferred from either or both the Accumulator and the Recycler to the Tevatron for final acceleration.

2.2 CDF Overview and Design

The Collider Detector at FNAL (CDF) is a general purpose charged and neutral particle detector [25] [26]. It surrounds one of the beam crossing points described in section 2.1. The detector observes particles or their decay remnants via charged tracks bending in a 1.4 T solenoidal field, electromagnetic and hadronic showers in calorimeters,

and charged tracks in muon detection chambers. Additionally, Cherenkov counters measure the instantaneous luminosity of the colliding beams. In order from nearest to beam line to the outermost region of the detector, the major components are the silicon tracking system, the central outer tracking system, the solenoid, the calorimeters, and the muon chambers, Figure 2-2.

CDF is cylindrical in construction, with the beam line defining the z -axis oriented with the direction of proton travel, which is also the direction of the solenoidal field lines. The x -axis is defined as pointing away from the Tevatron ring, and the y -axis is defined as pointing directly upward. Transverse components are defined to be perpendicular to the beam line, in other words the polar $r - \phi$ dimension as given in Equation 2-2. Another useful coordinate variable is the rapidity shown in Equation 2-3. The pseudo-rapidity, η , is the massless limit of rapidity and is given in Equation 2-4.

$$E_T = E \sin \theta \quad (2-2)$$

$$y = \frac{1}{2} \ln \frac{E + p_z}{E - p_z}. \quad (2-3)$$

$$\eta = -\frac{1}{2} \ln(\tan \theta). \quad (2-4)$$

Pseudo-rapidity is always defined with respect to the detector coordinates unless explicitly specified. Many of the components of CDF are segmented in pseudo-rapidity. Figure 2-3 shows the η coordinates relative to the tracking volume and plug calorimeter.

2.2.1 Cherenkov Luminosity Counters

To measure luminosity, Cherenkov Luminosity Counters (CLC) [27] are positioned near the beam line, $3.7 < |\eta| < 4.7$. The counters are long, conical chambers filled with isobutane at atmospheric pressure. Cherenkov light radiated from particles passing through the chambers is collected with Photo-Multiplier Tubes (PMTs) allowing a measurement of the number of inelastic $p\bar{p}$ interactions at each bunch crossing. The momentum threshold for detection of electrons is 9.3 MeV/c and of pions is 2.6 GeV/c.

Figure 2-4 shows the initial instantaneous luminosity and total integrated luminosity as a function of year. The initial instantaneous luminosity increased with running time due to improvements such as using the Recycler to store antiprotons. Total integrated luminosity is separated according to that delivered by the Tevatron and that recorded to tape by the CDF detector.

2.2.2 Silicon Tracking

The innermost component of CDF is a tracking system composed of silicon micro-strip arrays. Its main function is to provide precise position measurements near collision vertices, and it is essential for identification of secondary vertices.

Constructed in three separate components, L00 [28], SVXII [29] and ISL [30], the silicon tracking system covers detector $|\eta| < 2$. L00 is a single layer mounted directly on the beam pipe, $r = 1.6$ cm, and is a single-sided array with a pitch of $50 \mu\text{m}$ providing solely axial measurements. SVXII is mounted outside of L00, $2.4 < r < 10.7$ cm, and is composed of 5 concentric layers in ϕ and 3 segments, or barrels, in z . Each layer is further subdivided into 12 segments in ϕ , or wedges. Double-sided arrays provide axial ($r - \phi$) measurements on one side and stereo (z) measurements on the other. The stereo position of layer 0, 1 and 3 is perpendicular to the z -axis, and that of layer 2 and 4 is -1.2° and $+1.2^\circ$, respectively. The SVXII detector spatial resolution for axial measurements is $12 \mu\text{m}$. ISL surrounds SVXII, $20 < r < 29$ cm, and is composed of three layers of double-sided arrays. As with SVXII, one side provides axial measurements and the other stereo measurements at 1.2° relative to the z -axis. The ISL detector resolution for axial measurements is $16 \mu\text{m}$ (Figure 2-5).

2.2.3 Central Outer Tracker

The Central Outer Tracker (COT) [31] comprises the bulk of CDF's tracking volume, located between $40 < r < 132$ cm and detector $|\eta| < 1$. The COT provides the best measurements of charged particle momentum, but does not measure position as precisely as the silicon tracking system. It is a 96-layer open-cell drift chamber subdivided into 8

super-layers. Each super-layer is further divided with gold covered Mylar field sheets into cells containing 25 wires alternating between potential and sense wires, see Figure 2-6.

In half of the super-layers, the wires are parallel to the beam line and provide axial measurements, while in the other half, the wires are alternately at $\pm 2^\circ$ and provide stereo measurements. The innermost super-layer provides a stereo measurement and subsequent layers alternate between axial and stereo measurements. The gas filling the chamber is comprised of 50% argon and 50% ethane (and lately, some oxygen was added to prevent corrosion). This results in a maximum drift time of 100 ns, far shorter than the time between bunch collisions. The single hit resolution of the COT is $140 \mu\text{m}$, and the track momentum resolution using muon cosmic rays is $\sigma_{p_T/p_T^2} \approx 0.001 (\text{GeV}/c)^{-1}$.

2.2.4 Calorimeters

Calorimeters provide energy and position measurements of electron, photon and hadron showers. They are divided into electromagnetic (EM) and hadronic (HA) segments, with EM positioned closer to the interaction region than the HA. Both regions are sampling calorimeters with alternating layers of scintillators and absorbers. Showers generate photons in the scintillators which are collected and carried to PMTs with wavelength shifting optical fibers. Lead is used as the absorber in EM segments and iron in HA segments. The EM segment closest to the interaction region acts as a pre-shower detector useful for photon and π^0 discrimination. A shower-maximum detector, placed at about 6 radiation lengths in the EM calorimeter, measures the shower profile and obtains a position measurement with a resolution on the order of a few mm.

Due to detector geometry, calorimeters are divided into a barrel shaped region surrounding the solenoid, the central calorimeters (CPR, CES, CEM and CHA) [32]; and calorimeters capping the barrel, the plug calorimeters (PPR, PES, PEM and PHA) [33]. A wall hadronic calorimeter (WHA) fills the gap between the two. The central region covers detector $|\eta| < 1$, the wall $0.6 < |\eta| < 1.3$, and the plug $1.1 < |\eta| < 3.6$. Each of these regions is further segmented in η and ϕ into towers covering $0.1 \times 15^\circ$ in the central, $0.1 \times$

7.5° in the wall, and 0.16 x 7.5° or 0.2-0.6 x 15° in the plug. The energy resolution of the CEM is $\sigma(E)/E = 0.135/\sqrt{E_T(\text{GeV})} \pm 0.015$. Figure 2-7 shows a cross-sectional view of the plug calorimeter.

2.2.5 The Muon System

Whereas electrons create showers confined to the calorimeters, the mass of muons makes them nearly minimum ionizing particles (MIPs), and high momentum pass through the calorimeters. The calorimeters (and in some cases additional steel shielding) block the majority of hadronic particles from reaching the outer detector. Drift chambers placed on the outside of the detector identify charged tracks from muons and measure their position. There are three muon detection systems: CMU, CMP and CMX [34]. CMU and CMP cover detector $|\eta| < 0.6$, with CMP located outside CMU, and CMX covers detector $0.6 < |\eta| < 1$.

The CMU chambers surround the central calorimeter in ϕ . They are composed of 4 concentric layers of cells containing argon-ethane gas and high-voltage sense wires parallel to the beam pipe (Figure 2-8). The CMP chambers are separated from the CMU chambers by 60 cm of steel shielding. They are similar in construction to the CMU chambers, but the layers are successively offset by half of a cell. The CMX chambers are nearly identical to the CMU chambers. They are arranged in four logical layers successively offset by half of a cell. Each logical layer consists of two partially overlapping physical layers of cells. On average, a particle will traverse six cells. Sense wires are independent in the CMP chambers, but are shared between ϕ neighbors in CMU and CMX. The single-hit $r - \phi$ resolution is 0.25 mm. Measurements in z with a resolution of 1.2 mm are also possible by using differences in arrival times and amplitudes of pulses measured at either end of each wire in neighboring cells.

2.2.6 The Trigger System

Collisions occur every 396 ns (2.5 MHz), far too quickly even for CDF's custom hardware to process and read out detector information. To reduce the number of collisions

for which data is stored, CDF uses information from some detector components to make a decision to save an event, called a trigger. Data is stored in buffers until trigger decisions cause some of the events to be read out and stored on computer disk or the buffer to be emptied. The trigger is divided into three levels of increasing sophistication in object identification (Figure 2-9).

Data is stored in synchronous buffers awaiting an initial trigger decision. The first trigger level returns a decision with a latency of $5.5\ \mu\text{s}$ and a maximum accept rate of 50 kHz and will always occur in time to read out the event. Level one uses solely custom hardware operating in three parallel streams. One stream, the extremely Fast Tracker (XFT), reconstructs transverse COT tracks and extrapolates them to calorimeters and muon chambers. Another stream detects possible electron, photon or jet candidates, along with total and missing transverse energy. The final stream searches for tracks in muon chambers. These streams are combined in the final level one decision.

After a level one accept, the event information is read out into asynchronous buffers. Since events remain in these buffers until a level two decision is made, it is possible some events passing level one will be lost when these buffers are full. The level two trigger returns a decision with a latency of $25\ \mu\text{s}$ and a maximum accept rate of 300 Hz. Level two used custom hardware and modified commercial microprocessors to cluster energy in calorimeters and reconstruct tracks in the silicon detector using the Silicon Vertex Tracker (SVT). Calorimeter clusters estimate the total jet energy and help to identify electrons and photons. The SVT measures the impact parameters of tracks, part of locating displaced vertices.

The third trigger level runs on a commercial dual microprocessor farm and returns a decision with a maximum accept rate of 150 Hz. The farm runs a version of CDF offline reconstruction merging information from many detector systems to identify physical objects in the event. Data passing level three trigger requirements is transferred via

computer network to a storage facility using a robotic tape library. This data is then processed with offline reconstruction software for use in analyses.

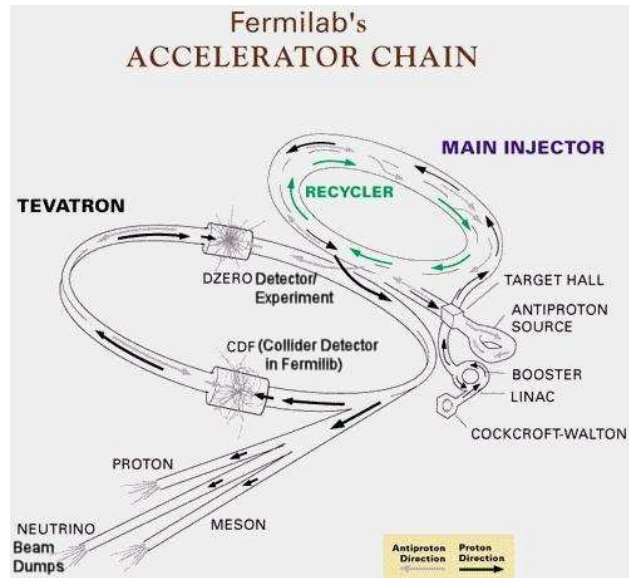


Figure 2-1. Diagram of the Tevatron accelerator complex

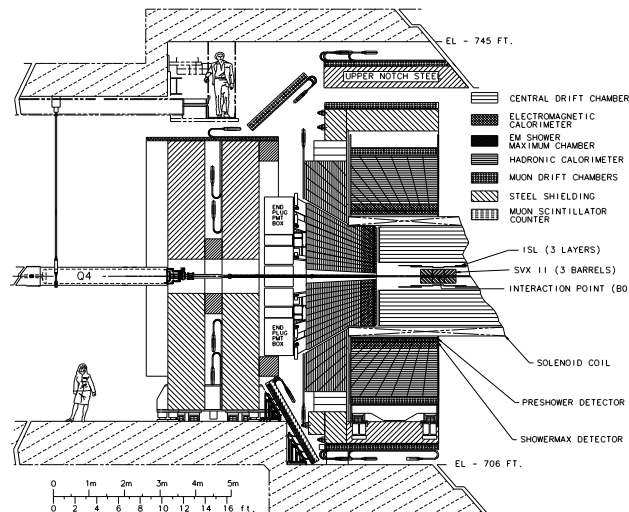


Figure 2-2. Elevation view of the East hall of the CDF detector. The West half is nearly symmetric.

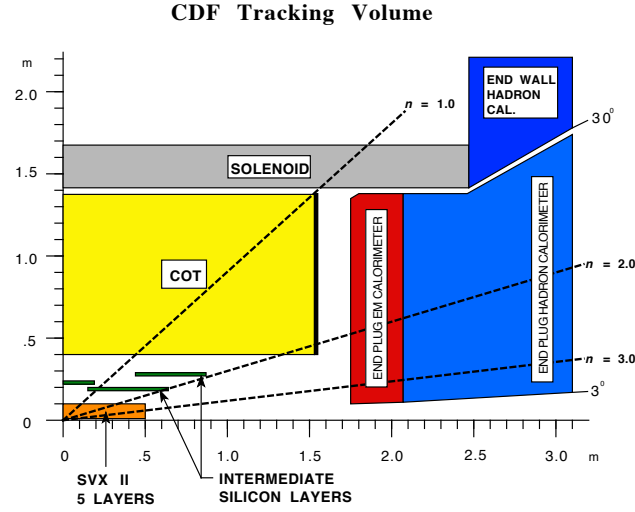


Figure 2-3. Schematic of tracking volume and plug calorimeters of the upper east quadrant of the CDF detector.

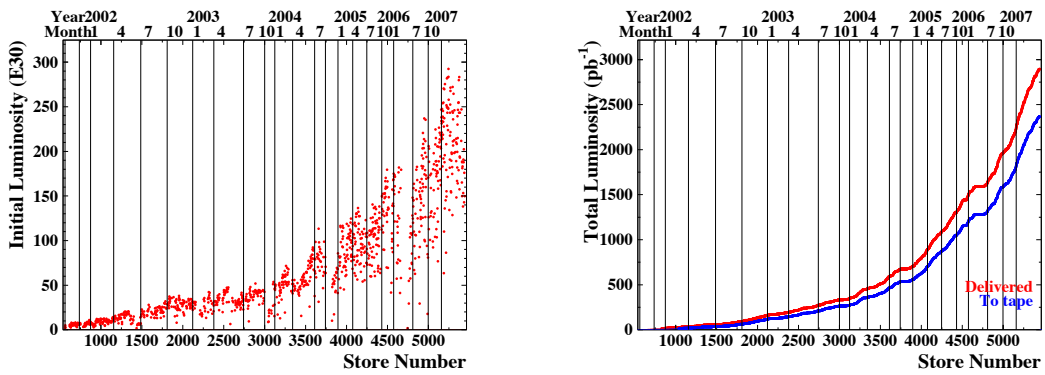


Figure 2-4. Initial instantaneous luminosity (left) and total integrated luminosity (right) as a function of year since the start of Run II.

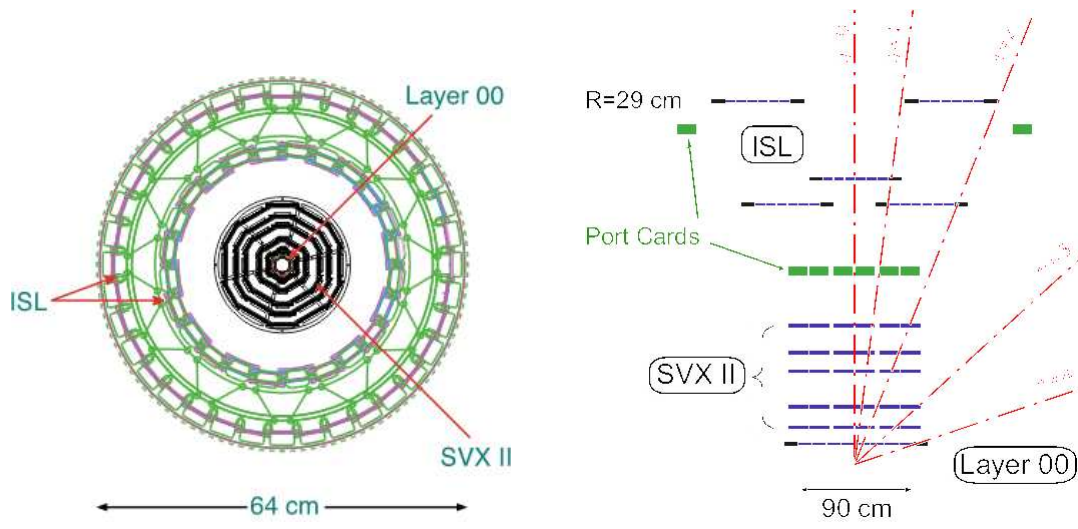


Figure 2-5. Schematic with the r - ϕ and the y - z views of the Run II CDF silicon tracking system.

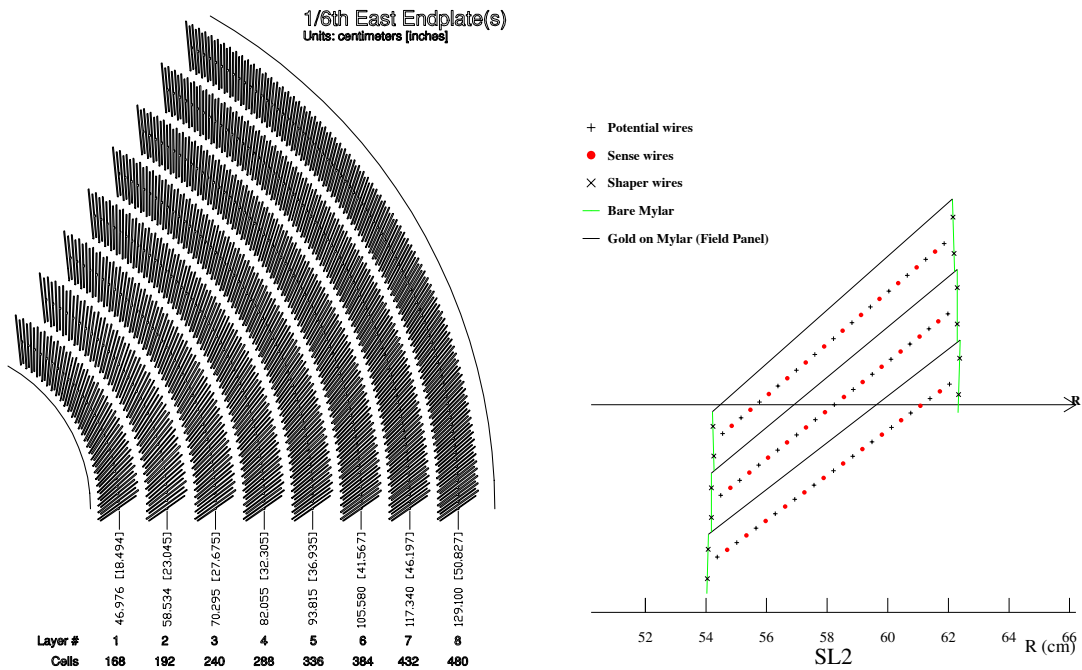


Figure 2-6. East end-plate slots Sense and field planes are at the clock-wise edge of each slot (left). Nominal cell layout (right).

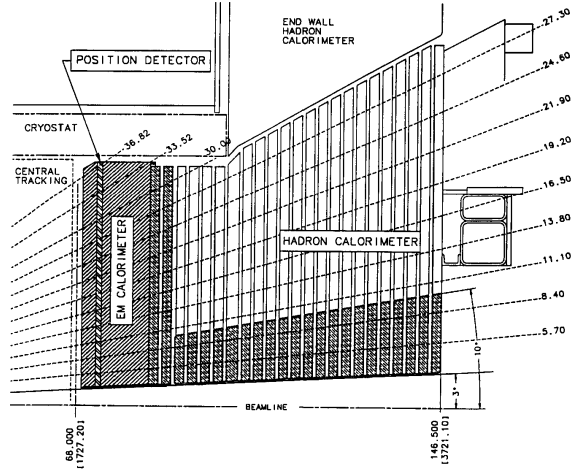


Figure 2-7. Cross section of upper part of new end plug calorimeter.

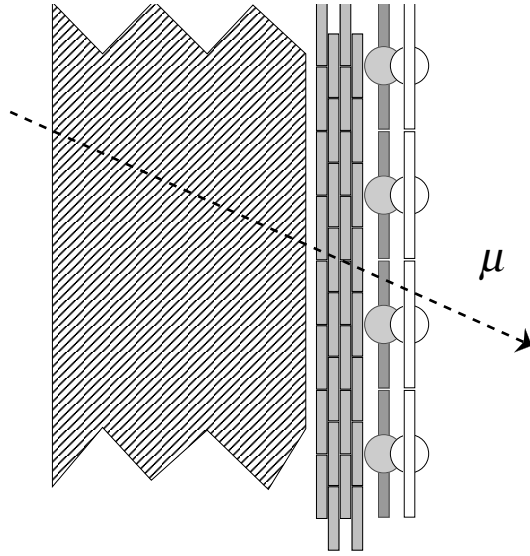


Figure 2-8. Detail showing the configuration of steel, chambers and counters for the Central Muon Upgrade walls. A muon track is drawn to establish the interaction point. Counter readout is located at $z=0$. Counters layers are offset from the chambers and from each other in x to allow overlapping light guides and PMTs, minimizing the space required.

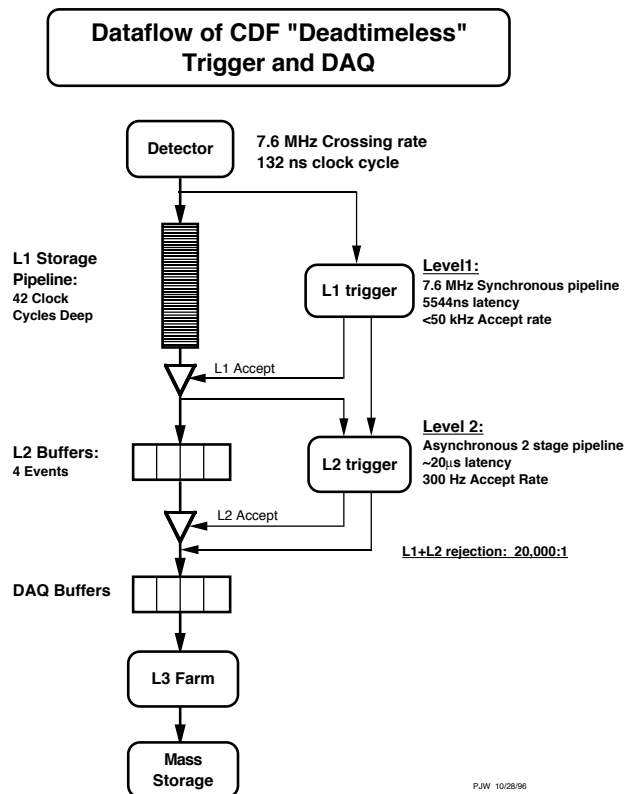


Figure 2-9. Readout functional block diagram in Run II.

CHAPTER 3

EVENT RECONSTRUCTION

In this chapter we will describe how we can identify the particles produced in a $p\bar{p}$ collision starting from the raw outputs of the different parts of the detector. First we will see how information from silicon detectors and COT are used to reconstruct charged particle trajectories. Then we will move to the reconstruction of jets of hadronic particles, based on calorimeters. A section will be devoted to the correction of jet energies for different error sources introduced by calorimeters and reconstruction algorithms. After a brief description of the identification of leptons and photons, we will end with the different methods used at CDF to identify a jet of particles originated from a b quark.

3.1 Tracks

Track reconstruction is performed using data from silicon tracking system and COT. The reconstruction is based on the position of the hits left by charged particles on detector components. Combining these hits one can reconstruct particle trajectories.

The whole tracking system is immersed in a 1.4 T magnetic field. Charged particles moving in a homogeneous magnetic field follow a helix trajectory. The helix axis is parallel to the magnetic field. Measuring the radius of curvature of the helix, one can obtain the transverse momentum of the particle, while the longitudinal momentum is related to the helix pitch. To describe a helix five parameters are needed, three to parameterize the circle in $r - \phi$ projection and two to parameterize the trajectory in z . At CDF, as shown by Equation 3-1, the helix of a charged particle is parameterized.

$$\vec{\alpha} = (\cot\theta, C, z_0, D, \phi_0) \quad (3-1)$$

The parameters used to describe the helix of a charged particle are: $\cot\theta$ is the cotangent of the polar angle at minimum approach to the origin; C is the half curvature, whose sign is given by the charge of the particle; z_0 is the position on z axis of the minimum approach to the helix origin; D is the signed impact parameter (i.e., the distance

between the helix and the origin at minimum approach); ϕ_0 is the direction in $r - \phi$ of the helix at the point of minimum approach.

If (x_0, y_0) is the center of the circle, then the impact parameter is calculated as in Equation 3-2, where $\rho = \frac{1}{2CQ}$ is the radius of the circle and Q the charge of the particle.

$$D = Q(\sqrt{x_0^2 + y_0^2} - \rho) \quad (3-2)$$

Having described the parameterization of a particle trajectory, we'll turn on the main tracking algorithms developed for offline analysis, the Standalone and the Outside-In algorithms.

Standalone tracking [35] is a strategy to reconstruct tracks in the silicon detector. It consists in finding triplets of aligned 3D hits, extrapolating them and adding matching 3D hits on other layers. This technique is called standalone because it doesn't require any input from outside: it performs tracking completely inside the silicon detector. First the algorithm builds 3D hits from all possible couples of intersecting axial and stereo strips on each layer. Once a list of such hits is available, the algorithm searches for triplets of aligned hits. This search is performed fixing a layer and doing a loop on all hits in the inner and outer layers with respect to the fixed one. For each hit pair - one in the inner and one in the outer layer - a straight line in the $r - z$ plane is drawn. Next step consists in examining the layer in the middle: each of its hits is used to build a helix together with the two hits of the inner and outer layers. The triplets found so far are track candidates. Once the list of candidates is complete, each of them is extrapolated to all silicon layers looking for new hits in the proximity of the intersection between candidate and layer. If there is more than one hit, the candidate is cloned and a different hit is attached to each clone. Full helix fits are performed on all candidates. The best candidate in a clone group is kept, the others rejected.

The Outside-In algorithm [36] exploits information from both COT and silicon. The first step is tracking in the COT, which starts translating the measured drift times in

hits positions: once all COT hit candidates in the event are known, the eight super-layers are scanned looking for line segments. A line segment is defined as a triplet of aligned hits which belong to consecutive layers. A list of candidate segments is formed and ordered by increasing slope of the segment with respect to the radial direction so that high momentum tracks will be given precedence. Once segments are available, the tracking algorithm tries to assemble them into tracks. At first, axial segments are joined in a 2D track and then stereo segments and individual stereo hits are attached to each axial track. Outside-In algorithm takes COT tracks and extrapolates them into the silicon detectors, adding hits via a progressive fit. As each layer of silicon is encountered (going from the outside in), a road size is established based on the error matrix of the track: currently, it is four standard deviations big. Hits that are within the road are added to the track, and the track parameters and error matrix are refit with this new information. A new track candidate is generated for each hit in the road, and each of these new candidates are then extrapolated to the next layer in, where the process is repeated. At the end of this process, there may be many track candidates associated with the original COT track. The candidate that has hits in the largest number of silicon layers is chosen as the real track: if more than one candidate has the same number of hits, the χ^2 of the fit in the silicon is used to choose the best track.

3.2 Vertex Reconstruction

The position of the interaction point of the $p\bar{p}$ collision (primary vertex) is of fundamental importance for event reconstruction. At CDF two algorithms can be used for primary vertex reconstruction.

One is called PrimVtx [37] and starts by using the beam line z -position (seed vertex) measured during collisions. Then the following cuts (with respect to the seed vertex position) are applied to the tracks: $|z_{trk} - z_{vertex}| < 1.0$ cm, $|d_0| < 1.0$ cm, where d_0 is track impact parameter, and $\frac{d_0}{\sigma} < 3.0$, where σ is error on d_0 .

Tracks surviving the cuts are ordered in decreasing p_T and used in a fit to a common vertex. Tracks with χ^2 relative to the vertex greater than 10 are removed and the remaining ones are fit again to a common point. This procedure is iterated until no tracks have $\chi^2 > 10$ relative to the vertex.

The second vertex finding algorithm developed at CDF is ZVertexColl [38]. This algorithm starts from pre-tracking vertices (i.e., vertices obtained from tracks passing minimal quality requirements). Among these, a lot of fake vertices are present: ZVertexColl cleans up these vertices requiring a certain number tracks with $p_T > 300$ MeV be associated to them. A track is associated to a vertex if it is within 1 cm from silicon standalone vertex (or 5 cm from COT standalone vertex). Vertex position z is calculated from tracks positions z_0 weighed by their error δ according to Equation 3-3.

$$z = \frac{\sum_i \frac{z_{0_i}}{\delta_i^2}}{\sum_i \frac{1}{\delta_i^2}} \quad (3-3)$$

Vertices found by ZVertexColl are classified by quality flags according to the number of tracks with silicon/COT tracks associated to the vertex. Associated COT tracks have shown to reduce the fake rate of vertices thus higher quality is given to vertices with COT tracks associated:

- **Quality 0:** all vertices
- **Quality 4:** at least one track with COT hits
- **Quality 7:** at least one track with COT hits, at least 6 tracks with silicon hits
- **Quality 12:** at least 2 tracks with COT hits
- **Quality 28:** at least 4 tracks with COT hits
- **Quality 60:** at least 6 tracks with COT hits

3.3 Jets Reconstruction

Jets are reconstructed by applying a clustering algorithm to calorimeter data. This algorithm determines the number of jets in an event, their energies and directions.

Each tower in the calorimeter is assigned a vector in the $r\eta\phi$ space: it originates in the interaction point and points toward the tower energy barycenter. Its module is equal to the total transverse energy of the tower. The tower barycenter is located at 6 radiation lengths X_0 for electromagnetic calorimeters and 1.5 interaction lengths λ for hadronic ones (i.e., it is assumed that all energy has been released at the average depth of calorimeters).

Towers with $E_T > 1$ GeV are ordered according to their decreasing energy and adjacent towers are grouped in pre-clusters. A fixed radius cone is drawn around each precluster in the $\eta - \phi$ plane ($\Delta r = \sqrt{\Delta\eta^2 + \Delta\phi^2}$); High multiplicity events have a smaller value for radius (typically $\Delta r = 0.4$), while a greater radius ($\Delta r = 0.7$) is chosen in other cases. The cone axis is the vector with maximum module.

All vectors falling inside a cone are summed and the axis is estimated again. This step is repeated until all vectors are assigned to a cone. Remaining vectors with $E_T > 1$ GeV are associated to the cone containing them and the axis is estimated again until no new vector is found inside the cone.

If two cone overlap, two solutions are possible, depending on how much is the energy they have in common: if the less energetic one has more than 75% of its energy in common with the other, the two cones are merged into a single one. Otherwise, they are kept separated and common vectors are assigned to the closest cone in the $\eta - \phi$ plane.

Finally, summing all vectors in a cone, jet 4-momentum is computed in Equation 3–4 assuming that each vector corresponds to a massless particle that deposited all its energy in the tower barycenter.

$$\begin{aligned}
E &= \sum_i (E_i^{had} + E_i^{em}) \\
p_x &= \sum_i (E_i^{had} \sin\theta_i^{had} + E_i^{em} \sin\theta_i^{em}) \cos\phi_i \\
p_y &= \sum_i (E_i^{had} \sin\theta_i^{had} + E_i^{em} \sin\theta_i^{em}) \sin\phi_i \\
p_z &= \sum_i (E_i^{had} \cos\theta_i^{had} + E_i^{em} \cos\theta_i^{em})
\end{aligned} \tag{3–4}$$

Starting from the quantities in Equation 3-4, the jet transverse energy, transverse momentum and pseudo-rapidity are calculated in Equations 3-5, 3-6 and 3-7.

$$P_T = \sqrt{p_x^2 + p_y^2} \quad (3-5)$$

$$E_T = P_T \frac{E}{P} \quad (3-6)$$

$$\eta = 0.5 \ln \frac{E + p_z}{E - p_z} \quad (3-7)$$

The jet 4-momenta measured in the calorimeter suffer from intrinsic limits of both calorimeter and jet algorithm. Different particles produce different responses in calorimeters and some of them can fall in uninstrumented regions of the detector. Moreover, calorimeter response to particle energies is non-linear. The jet clustering algorithm, on the other hand, doesn't take into account multiple interactions and energy that can be radiated outside the fixed radius cone. For all these reasons, a set of corrections has been developed in order to scale measured jet energy back to the energy of the particle [39].

3.3.1 Relative Energy Scale Correction

Relative (or η -dependent) jet energy corrections [40] are applied to raw jet energies to correct for non-uniformities in calorimeter response along η . Calorimeter response in each η bin is normalized to the response in the region with $0.2 \leq |\eta| \leq 0.6$, because this region is far away from detector cracks and it is expected to have a stable response. The correction factor is obtained using the dijet balancing method applied to dijet events.

This method starts selecting events with one out of two jets in the region $0.2 \leq |\eta| \leq 0.6$. This jet is defined as trigger jet. The other jet is defined as probe jet. If both jets are in the region of $0.2 \leq |\eta| \leq 0.6$, trigger and probe jet are assigned randomly. The transverse momentum of two jets in a $2 \rightarrow 2$ process should be equal and this property is used to calculate first a p_T balancing fraction $\Delta p_T f$ as shown in Equation 3-8.

$$\Delta p_T f = \frac{\Delta p_T}{p_T^{ave}} = \frac{p_T^{probe} - p_T^{trigger}}{(p_T^{probe} + p_T^{trigger})/2} \quad (3-8)$$

Then a correction factor to make, on average, the probe jet scale equal to trigger is calculated in Equation 3-9.

$$\beta = \frac{p_T^{probe}}{p_T^{trigger}} = \frac{2 + \Delta p_T f}{2 - \Delta p_T f} \quad (3-9)$$

In Figure 3-1 we show the correction factor as a function of η for dijet data (black) and for dijet Monte Carlo using Pythia as generator (red).

3.3.2 Multiple Interactions Correction

At current instantaneous luminosity and with 36 bunches, we expect on average one hard interaction per beam crossing. However, in a fraction of events more than one $p\bar{p}$ interaction can occur. Energy from these non overlapping minimum bias events may fall into the jet clustering cone of the hard interaction causing thus a mis-measurement of jet energy. A correction for this effect is extracted using a sample of minimum bias events [41]: for each event, transverse energy E_T inside cones of different radii (0.4, 0.7 and 1.0) is measured in a region far away from cracks ($0.1 \leq |\eta| \leq 0.7$): then, the distribution of average E_T as a function of the number of quality 12 vertices is fitted with a straight line and the slope of the fitting lines are taken as correction factors (Figure 3-2).

3.3.3 Absolute Energy Scale Correction

A jet contains different types of particles with wide momentum spectra. Absolute energy scale correction converts the calorimeter cluster transverse momentum p_T to the sum of transverse momenta of the particles in the jet cone [42]. The procedure to extract a calorimeter-to-hadron correction factor is based on the following steps:

- use fully simulated CDF samples where particles have p_T ranging from 0 to 600 GeV,
- cluster the calorimeter towers and the HEPG particles,
- associate calorimeter-level jets with hadron-level jets,
- parameterize the mapping between calorimeter and hadron-level jets as a function of hadron-level jets,
- as a correction factor, extract the probabilities of measuring a jet with p_T^{cal} given a jet with fixed value of p_T^{had} .

In Figure 3-3 the absolute jet energy scale corrections for jets cone size of 0.4 as a function of the jet momentum (blue). The uncertainty for this correction is also shown as a function of the jet momentum (black).

3.3.4 Underlying Event Correction

In a hadron-hadron collision, in addition to the hard interaction that produces the jets in the final state, there is also activity in the detector originating from soft spectator interactions. In some event, the spectator interaction may be hard enough to produce soft jets. Energy from the underlying event can fall in the jet cones of the hard scattering process thus biasing jet energy measurements. A correction factor for such effect has been calculated using a sample of minimum bias events as for multiple interaction correction, but selecting only those events with one vertex [43]. For each event, transverse energy E_T inside cones of different radii (0.4, 0.7 and 1.0) is measured in a region far away from cracks ($0.1 \leq |\eta| \leq 0.7$). The correction factor is extracted from the mean values of E_T distribution (Figure 3-4).

3.3.5 Out of Cone Correction

The jet clustering may not include all the energy from the initiating partons. Some of the partons generated during fragmentation may fall outside the cone chosen for the clustering algorithm. This energy must be added to the jet to get the parton level energy. A correction factor is obtained using MC events [44]: hadron-level jets are matched to partons if their distance in the $\eta - \phi$ plane is less than 0.1. Then the difference in energy between hadron and parton jet is parameterized using the same method as for absolute correction (Figure 3-5).

We have seen different corrections that account for different sources of jet energy mis-measurement. Depending on the physics analysis, all of them or just a subset can be applied. The corrections are applied to the raw measured jet momentum.

$$P_T(R, P_T, \eta) = (P_T^{raw}(R) \cdot f_\eta(R, P_T, \eta) - M_I(R)) \cdot f_{abs}(R, P_T) - UE(R) + OOC(R, P_T) \quad (3-10)$$

In Equation 3–10, R is the clustering cone radius, P_T is the raw energy measured in the cone and η the pseudo-rapidity of the jet: f_η , M_I , f_{abs} , UE and OOC are respectively relative, multiple interactions, absolute, underlying event and out-of-cone correction factors.

3.4 Leptons Reconstruction

3.4.1 Electrons

Being a charged particle, an electron traversing the detector first leaves a track in the tracking system and then loses its energy in the electromagnetic calorimeter. So a good electron candidate is made of a cluster in the electromagnetic calorimeter (central or plug) and one or more associated tracks; if available, shower max cluster and preshower clusters can help electron identification. The shower has to be narrow and well defined in shape, both longitudinally and transversely. The ratio between hadronic and electromagnetic energies has to be small and track momentum has to match electromagnetic cluster energy [45].

3.4.2 Muons

Muons can leave a track in the tracking system and in the muon system, with little energy deposition in the calorimeter. Muons are reconstructed using the information coming from muon chambers (CMU , CMP , CMX , BMU) and muon scintillators (CSP , CSX , BSU , TSU). The first provide measurements of drift time, which is then converted to a drift distance (i.e., a distance from the wire to a location that the muon has occupied in its flight, in the plane perpendicular to the chamber sense wire). Scintillators, on the other hand, only produce timing information. The output of chambers and scintillators produce muon hits. A muon track segment (a stub) is obtained by fitting the muon hits. Finally, COT tracks are extrapolated to the muon chambers and matched to muon stubs in the $r - \phi$ plane [46].

3.4.3 Tau Leptons

Tau lepton can decay leptonic-ally into electron or muon (and the corresponding neutrinos) or semileptonically into charged and neutral pions: the first case is not distinguishable from a leptonic decay from W bosons, while the second has a precise signature. Taus decay preferably into 1 or 3 charged pions and in most cases neutral pions are present. So a well isolated jet with low track multiplicity and neutral pions is a good tau candidate. The reconstruction procedure exploits information from calorimeter and tracking systems. One looks for an isolated narrow cluster above a certain energy threshold and then matches it to COT tracks.

3.4.4 Neutrinos

Neutrinos don't leave any signature in the detector, but their presence can be inferred from requiring momentum conservation in the plane transverse to the beam line. As the mass of the neutrino is negligible, then its transverse energy can be expressed as the opposite of the vector sum of all calorimetric towers.

$$\vec{E}_T = - \sum_{towers} (E_i \sin \theta_i) \vec{n}_i \quad (3-11)$$

In Equation 3-11, E_i is the energy of the i th tower, θ_i is the polar angle of the line pointing from the interaction point to the i th tower and \vec{n}_i is the transverse unit vector pointing from the interaction point to the center of the tower.

3.5 Photon Reconstruction

A photon traversing with the CDF detector leaves most of its energy in the electromagnetic calorimeter and leaves a signature in the shower max detector without a track pointing to it. Its identification algorithms start looking for clusters of energy around a seed tower with energy greater than 3 GeV. Total energy of the hadronic towers located behind the photon cluster has to be very small with respect to the electromagnetic cluster. Photon cluster isolation is required: the difference between photon energy and the energy in a cone of radius 0.4 around the seed tower has to be less than 15% of photon

energy. Moreover, the sum of transverse momenta of all tracks pointing to the 0.4 cone should be less than 2 GeV/c. The line connecting the primary vertex to the shower max position of the photon candidate determines the photon direction.

3.6 Bottom Quark Tagging

The hadrons produced by a b quark have two important properties: long lifetime allowing it to travel before decaying and the possibility of semi-leptonic decay $b \rightarrow l\nu s$. Typically, the lifetime is about 1.5 ps for a hadron with an energy of about 40 GeV, so the distance it travels is few millimeters. From these properties it is possible to construct algorithms to tag jets if they are produced by b quarks. At CDF there are used three such algorithms: the SecVtx algorithm, the JetProbability (JP) algorithm and the Soft Lepton Tagging (SLT) algorithm.

3.6.1 SecVtx Algorithm

This algorithm [47] exploits the fact that the B hadron travels before it decays and therefore the jet produced by it will contain a secondary vertex (Figure 3-6). The algorithm starts from COT and silicon tracks inside a cone and as a first step, using as discriminating variable their impact parameter, it removes tracks identified as K_S, Λ or γ daughters, or consistent with primary vertex or too far from it. Then a three dimensional common vertex constrained fit is performed using two tracks: if $\chi^2 < 50$ the two tracks are used as seed to find other tracks that point toward the same secondary vertex. If at least three tracks are found to be compatible with a secondary vertex, the jet containing them is considered a b-tag if it passes the following cuts:

- $|L_{xy}| < 2.5$ cm, where L_{xy} is the decay length of the secondary vertex; this cut helps rejecting conversions from the first layer of SVXII;
- $\frac{L_{xy}}{\sigma_{L_{xy}}} > 3$;
- if M_{trk} is the invariant mass of the tracks, $|m_{K_S} - M_{trk}| > 0.01$ GeV and $|m_{\Lambda} - M_{trk}| > 0.006$ GeV;
- $|L_{xy} \cdot (M_{trk}/p_{trk})| < 1$ cm.

The tags are classified depending on where the secondary vertex is located with respect to the jet cone axis. Secondary vertices on the same side of the interaction point as the jet cone axis are positive tags, otherwise they are labeled as negative tags. Negative tags can arise from tracks mis-measurements.

3.6.2 Jet Probability Algorithm

This algorithm uses the information of the tracks associated to a jet to determine the probability that the jet comes from the primary vertex [48]. The probability distribution is uniformly distributed for a jet arising from the primary vertex, while it shows a peak at zero for a long-lived jet (Figure 3-7). The probability is based on track impact parameters and on their uncertainties. All tracks associated to the primary vertex have equal probability to be either positively or negatively signed as far as their impact parameter is concerned. The width of the impact parameter distribution from these tracks is solely due to the tracking detector resolution and multiple scattering. A long-lived particle will produce more tracks with positive impact parameter (Figure 3-8). To minimize the contribution of mis-measured tracks, the final probability is computed using the signed impact parameter significance (ratio of the impact parameter to its measured error) instead of the parameter itself. Given a track with impact parameter significance S_{d_0} , the probability that a track from a light quark has a larger value of S_{d_0} is calculated. Combining probabilities for all tracks in a jet, one obtains the jet probability. By construction, this probability is flat for jets coming from light quarks or peaked at zero for those coming from heavy quarks.

3.6.3 Soft Lepton Tag Algorithm

This algorithm is based on the fact that about 20 % of b quarks decay to muons. In general, muon identification relies on the presence of a stub in the muon chambers, associated with a track and minimum ionization energy deposition in the calorimeter. Muons coming from b quarks are not isolated so information from calorimeters can't be used. Moreover, multiple scattering of muons in the material of CDF detector has to be

taken into account. This causes a deflection in the muon path that ranges from about a few milimeters for a momentum of 2 GeV/c to about half a meter for a 50 GeV/c muon. The SLT algorithm procedure can be divide in two steps [49].

First, the taggable tracks are found (i.e., tracks that could have been left by muons). To take into account the fact that the muon might not have had enough energy to reach the muon chambers, tracks whose momentum is lower than 2.8 GeV are rejected. Moreover, it has to point to a volume limited by the physical edges of the muon chambers, or a distance of $3 \sigma_{MS}$ inside/outside the physical edges. Here σ_{MS} is the standard deviation of the maximum deflection expected from multiple scattering through the material of the detector.

If a track is taggable and has a stub associated to it, the algorithm computes a likelihood comparing all the available information about the muon candidate with the expected values. Besides variables from muon detectors, for the likelihood one can use also some track quality information, like the number of COT hits, the beam line-corrected impact parameter and the track z_0 position.

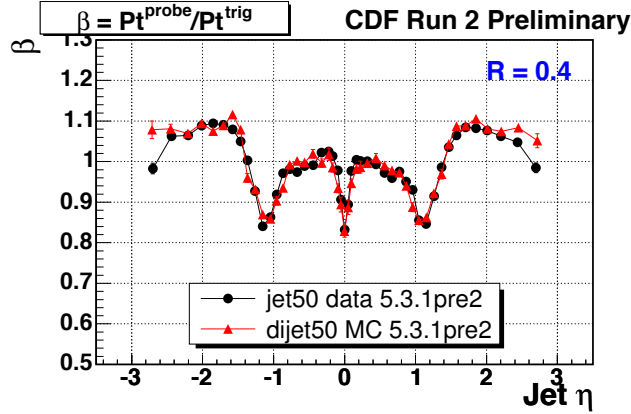


Figure 3-1. Correction factor as a function of η for dijet data (black) and for dijet Monte Carlo using Pythia as generator (red). The jets were reconstructed with a cone of 0.4.

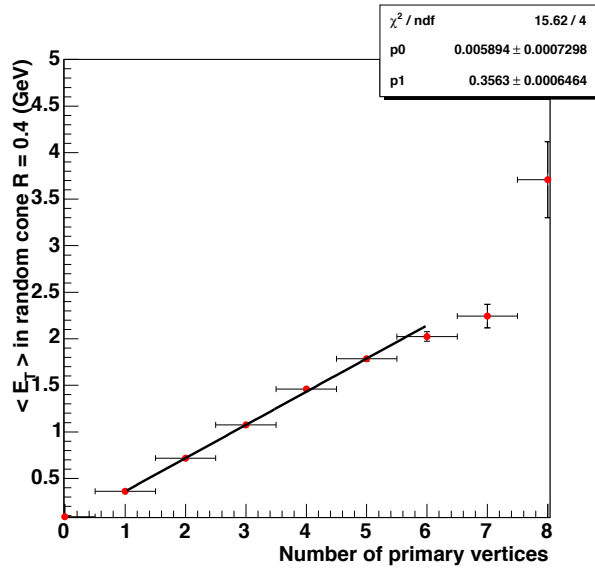


Figure 3-2. Average transverse energy as a function of the number of primary vertices in the event: a correction factor is extracted from the slope of the fitting line.

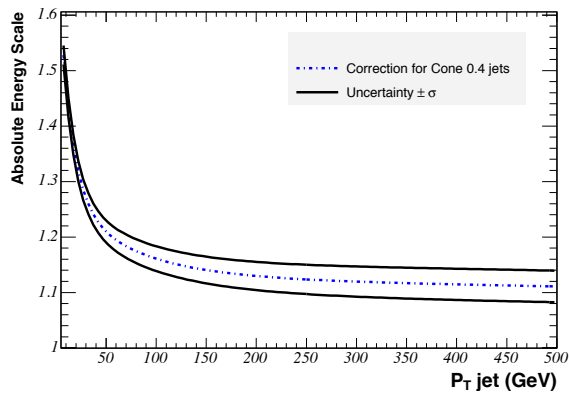


Figure 3-3. Absolute jet energy scale corrections for jets with cone size of 0.4 as a function of the jet momentum (blue). The uncertainty for this correction is also shown as a function of the jet momentum (black).

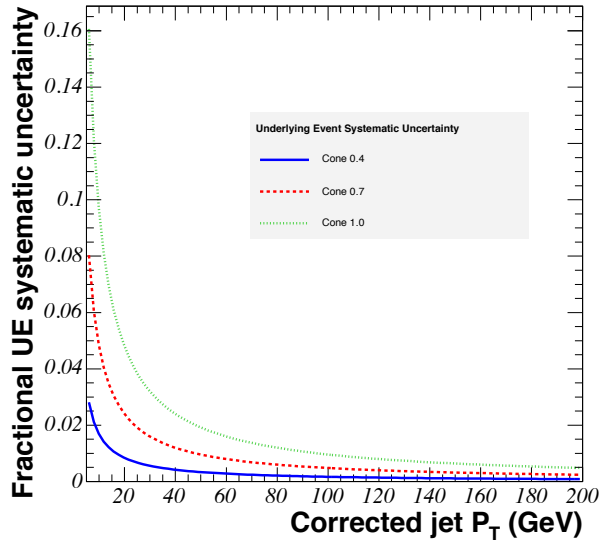


Figure 3-4. Fractional systematic uncertainty due to underlying event as a function of jet transverse momentum for different jet cone sizes.

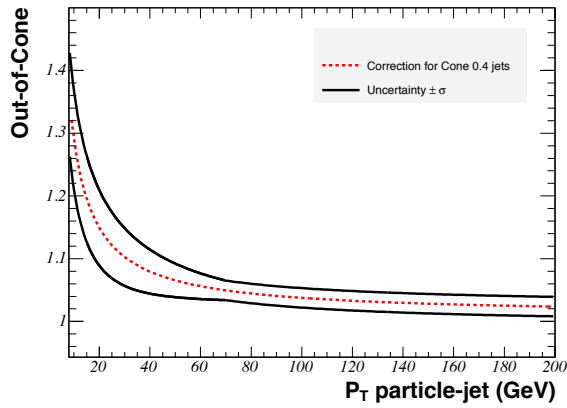


Figure 3-5. Jet corrections due to out-of-cone effect for jets with cone size of 0.4 as a function of the jet momentum (red). The uncertainty for this correction is also shown as a function of the jet momentum (black).

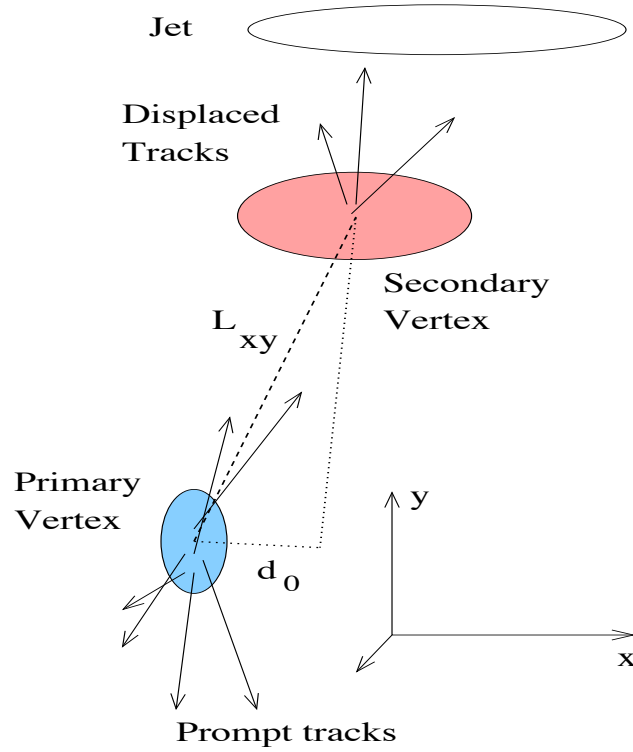


Figure 3-6. Schematic view of an event containing a jet with a secondary vertex.

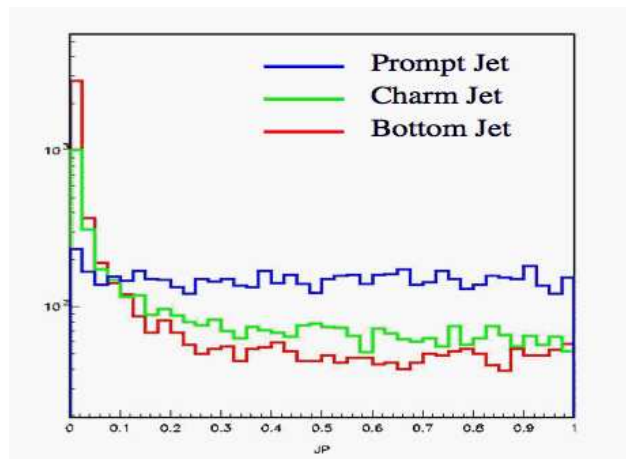


Figure 3-7. Jet probability distribution for prompt, charm and bottom jets.

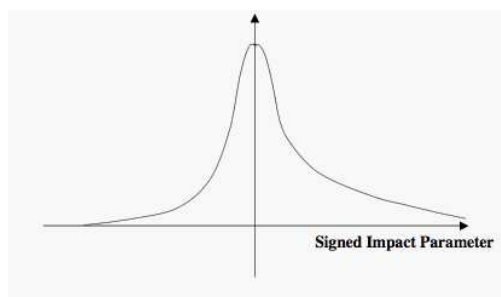
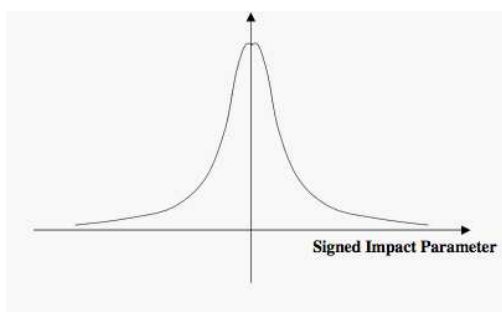


Figure 3-8. Signed impact parameter distribution for tracks from primary vertex (left) and from secondary vertex (right).

CHAPTER 4

DESCRIPTION OF THE MATRIX ELEMENT MACHINERY

In this section we will present in detail how the matrix element is calculated and used in our analysis. The matrix element is used to calculate the a priori probability density for an event to be the result of the $t\bar{t}$ Standard Model production and decay at a given pole mass M_{top} . We will dedicate a section for the general expression of the probability density, one section discussing the combinatorics, another for the matrix element calculation, another for the transfer functions, another on the transverse momentum of the $t\bar{t}$ system, and in the final section of this chapter we will put together the final expression of the probability density with its implementation details.

4.1 Probability Density Definition

Given an event defined by a set of six observables (i.e., jets) one can compute the elementary cross-section at a given top mass m as if the event were the result of $t\bar{t}$ production followed by the all hadronic decay as given by Equation 4-1.

$$d\sigma(m, j) = \int \frac{dz_a dz_b f(z_a) f(z_b)}{4E_a E_b |v_a - v_b|} |\mathcal{M}(m, j)|^2 (2\pi)^4 \delta^{(4)}(E_{fin} - E_{ini}) \prod_{i=1}^6 \left[\frac{d^3 \vec{j}_i}{(2\pi)^3 2E_i} \right] \quad (4-1)$$

In Equation 4-1, j is a generic notation by which we understand all six 4-momenta describing the final state; $z_a(z_b)$ is the fraction of the proton(anti-proton) momentum carried by the colliding partons; $f(z_a)$ and $f(z_b)$ stand for the parton distribution functions for proton and for anti-proton respectively; $\mathcal{M}(m, j)$ is the matrix element corresponding to the all hadronic $t\bar{t}$; E_{fin} is a generic notation for the 4-vector of the final state, and similarly for the initial state we use E_{ini} .

If the elementary cross-sections from a group of events are added up we should obtain a fraction of total $t\bar{t}$ cross-section, $\sigma_{tot}(m)$, for top mass m as shown in Equation 4-2.

$$\sigma(m) = \int d\sigma(m, j) = \sigma_{tot}(m) \epsilon(m) \quad (4-2)$$

where $\epsilon(m)$ represents the fraction of events considered. In practice we use only a fraction of the events, namely those passing certain selection criteria.

At this point, we can define a probability density for each event. This is nothing but the normalized elementary cross-section without the d^3j measure as given by Equation 4-3.

$$P(j|m) = \int \frac{dz_a dz_b f(z_a) f(z_b)}{4E_a E_b |v_a - v_b|} \frac{|\mathcal{M}(m, j)|^2 (2\pi)^4 \delta^{(4)}(E_{fin} - E_{ini})}{\sigma_{tot}(m) \epsilon(m)} \prod_{i=1}^6 \left[\frac{1}{(2\pi)^3 2E_i} \right] \quad (4-3)$$

The quantity $P(j|m) \prod_{i=1}^6 d^3\vec{j}_i$ will be the probability for an event defined by the set of six jets (i.e., six 4-momenta) to be the result of $t\bar{t}$ production followed by an all hadronic decay for top mass m .

So far we didn't worry about how accurately we can determine the six 4-momenta. In reality, the final state partons which are observed as jets in the detector, can be mis-measured. We can account for this using our $t\bar{t}$ Monte Carlo samples and determine a probability for a parton with 4-momentum p to be observed as a jet with 4-momentum j . This new probability is called *TransferFunction* $TF(\vec{j}|\vec{p})$ and all the technical details on how we determine them will be presented in section 4.4.

Since we don't know what is the parton 4-momentum that generated a given jet 4-momentum we have to consider all possibilities and integrate over them weighed by the transfer functions. The Equation 4-3 can be rewritten as in Equation 4-4.

$$P(j|m) = \frac{1}{\sigma_{tot}(m) \epsilon(m)} \int \frac{dz_a dz_b f(z_a) f(z_b)}{4E_a E_b |v_a - v_b|} \int \prod_{i=1}^6 \left[\frac{d^3\vec{p}_i}{(2\pi)^3 2E_i} \right] |\mathcal{M}(m, p)|^2 \times \\ \times TF(\vec{j}|\vec{p}) (2\pi)^4 \delta^{(4)}(E_{fin} - E_{ini}) \quad (4-4)$$

The parton configurations integrated over in Equation 4-4 are weighed by the transfer functions so that those more likely to produce a given 6-jets event are enhanced. Ideally the $t\bar{t}$ phase space should be enhanced as well and not diminished. In order to enforce this last aspect of the integration, we introduce an additional weight, $P_T(\vec{p})$, that follows the shape of the transverse momentum of the $t\bar{t}$ system. This last weight

is also determined with the help of a Monte Carlo sample and we'll offer more details in section 4.5. Therefore the new expression for the probability density is shown in Equation 4-5.

$$P(j|m) = \frac{1}{\sigma_{tot}(m)\epsilon(m)} \int \frac{dz_a dz_b f(z_a) f(z_b)}{4E_a E_b |v_a - v_b|} \int \prod_{i=1}^6 \left[\frac{d^3 \vec{p}_i}{(2\pi)^3 2E_i} \right] |\mathcal{M}(m, p)|^2 \times \\ \times (2\pi)^4 \delta^{(4)}(E_{fin} - E_{ini}) TF(\vec{j}|\vec{p}) P_T(\vec{p}) \quad (4-5)$$

Even though a $t\bar{t}$ event in the all hadronic final state is fully reconstructed, there is an ambiguity in assigning the jets to the partons. Therefore all the possible combinations are considered and their contributions averaged. The number of possible assignments depends on the topology of the event and this will be discussed in section 4.2. Until then the Equation 4-6 gives the most general expression of the probability density.

$$P(j|m) = \frac{1}{\sigma_{tot}(m)\epsilon(m)N_{combi}} \sum_{combi} \int \frac{dz_a dz_b f(z_a) f(z_b)}{4E_a E_b |v_a - v_b|} \int \prod_{i=1}^6 \left[\frac{d^3 \vec{p}_i}{(2\pi)^3 2E_i} \right] \times \\ \times |\mathcal{M}(m, p)|^2 (2\pi)^4 \delta^{(4)}(E_{fin} - E_{ini}) TF(\vec{j}|\vec{p}) P_T(\vec{p}) \quad (4-6)$$

4.2 Combinatorics

In general, there are $6! = 720$ ways to assign the observed jets to the six partons of the final state in an all hadronic $t\bar{t}$ process. This number can be reduced by making few observations and assumptions.

First, one has to notice that the matrix element is symmetric to $t \leftrightarrow \bar{t}$. Let's write down in Equation 4-7 the spin averaged matrix element squared for the process $u\bar{u} \rightarrow t\bar{t}$.

$$\frac{1}{4} \sum_{spins} |\mathcal{M}|^2 = \frac{g_s^4}{288(p_u + p_{\bar{u}})^4} Tr[\gamma^\mu (\not{p}_u + m_u) \gamma^\nu (\not{p}_{\bar{u}} - m_{\bar{u}})] Tr[\gamma_\mu (\not{p}_{\bar{t}} - m_{\bar{t}}) \gamma_\nu (\not{p}_t + m_t)] \quad (4-7)$$

Assuming that the masses of the up quarks are zero and omitting the constant and the gluon propagator term, we can write Equation 4-8.

$$\frac{1}{4} \sum_{spins} |\mathcal{M}|^2 \approx Tr[\gamma^\mu \not{p}_u \gamma^\nu \not{p}_{\bar{u}}] Tr[\gamma_\mu (\not{p}_{\bar{t}} - m_{\bar{t}}) \gamma_\nu (\not{p}_t + m_t)] \quad (4-8)$$

After using the properties of the gamma matrices and the full trace technology, we are left with the expression in Equation 4-9.

$$\frac{1}{4} \sum_{spins} |\mathcal{M}|^2 \approx 32(p_u \cdot p_{\bar{t}})(p_{\bar{u}} \cdot p_t) + 32(p_u \cdot p_t)(p_{\bar{u}} \cdot p_{\bar{t}}) + 32m(p_u \cdot p_{\bar{u}}) \quad (4-9)$$

From Equation 4-9 the $t \leftrightarrow \bar{t}$ symmetry is evident. This should hold for the matrix element of the process containing the decay of the top quarks since this symmetry reflects the invariance to the charge conjugation of the strong interaction. This symmetry can be translated into a symmetry to $b \leftrightarrow \bar{b}$ once we consider all possible b - W pairings for each top quark: $\{t = (b_1, W_1), \bar{t} = (b_2, W_2)\}, \{t = (b_1, W_2), \bar{t} = (b_2, W_1)\}$. It is obvious that swapping the b 's is equivalent with swapping the top quarks.

In conclusion, due to the $t \leftrightarrow \bar{t}$ symmetry the total number of combinations is reduced to 360. Secondly, if any of the jets can be identified as a heavy flavor jet we can assume that jet to be produced by a b -quark. This assumption results in a factor of 3 reduction of the total number of combinations, down to 120 (or 5!). If there is an additional heavy flavor jet, we get a factor of 5 reduction down to 24 (or 4!). If there are more than two heavy flavor jets, we will assign to a b -quark only the two jets with the highest transverse energy since we expect the b -quarks to be more energetic than the W -boson decay products. The Equation 4-10 summarizes the possible values for N_{combi} .

$$N_{combi} = \begin{cases} 360, & \text{for 0 } b\text{-tags} \\ 120, & \text{for 1 } b\text{-tags} \\ 24, & \text{for 2 } b\text{-tags} \end{cases} \quad (4-10)$$

4.3 Calculation of the Matrix Element

In this analysis we use the matrix element describing the process $u\bar{u} \rightarrow t\bar{t} \rightarrow b\bar{b}u\bar{u}d\bar{d}$. As far as the incident partons are concerned, the $d\bar{d}$ annihilation and the gluon-gluon fusion should be considered as well. For the energy at the Tevatron the gluon-gluon fusion is about 15%, and of the remaining contributions the $u\bar{u}$ dominates at 90%. In a sample

with only gluon-gluon fusion we reconstructed the top mass using an only $u\bar{u}$ matrix element and we didn't observe any bias. We concluded that using $u\bar{u}$ in the initial state should be sufficient for mass reconstruction.

For the final state, having a W boson decay into a ud pair or a cs pair doesn't make a difference. The other decays are suppressed via the CKM matrix. Therefore all we need to do is calculate the matrix element for the case when both W bosons decay into ud pairs and multiply by 4 in the expression of the probability density given in Equation 4-6.

The invariant amplitude for the process $u\bar{u} \rightarrow t\bar{t} \rightarrow b\bar{b}u\bar{u}d\bar{d}$ is given below as a product of several factors as shown in Equation 4-11.

$$i\mathcal{M} = A \cdot C(ij \rightarrow kl) \cdot I \cdot P_g \cdot T \cdot P_t \cdot P_{\bar{t}} \cdot W_1 \cdot P_{W_1} \cdot W_2 \cdot P_{W_2} \quad (4-11)$$

All the terms entering the invariant amplitude shown in Equation 4-11 are detailed by the Equation 4-12.

$$\begin{aligned} A &= \frac{-ig_s^2 g_W^4}{2^8} \\ C(ij \rightarrow kl) &= \lambda_{ij}^a \lambda_{kl}^b \\ I &= \bar{v}(p_{\bar{u}}) \gamma^\mu u(p_u) \\ P_g &= \frac{1}{(p_u + p_{\bar{u}})^2 + i\epsilon} \\ T &= \bar{u}(p_b) \gamma^\alpha (1 - \gamma^5) (\not{p}_t + m) \gamma_\mu (\not{p}_{\bar{t}} + m) \gamma^\rho (1 - \gamma^5) v(p_{\bar{b}}) \\ P_t &= \frac{1}{p_t^2 - m^2 + im\Gamma_t} \\ P_{\bar{t}} &= \frac{1}{p_{\bar{t}}^2 - m^2 + im\Gamma_t} \\ W_1 &= \bar{u}(q_u) \gamma_\alpha (1 - \gamma^5) v(q_{\bar{d}}) \\ P_{W_1} &= \frac{1}{P_{W_+}^2 - M_W^2 + iM_W\Gamma_W} \\ W_2 &= \bar{u}(q_d) \gamma_\rho (1 - \gamma^5) v(q_{\bar{u}}) \\ P_{W_2} &= \frac{1}{P_{W_-}^2 - M_W^2 + iM_W\Gamma_W} \end{aligned} \quad (4-12)$$

The term A is a constant representing the product of all constants present in the vertex terms and the propagator terms of the process $u\bar{u} \rightarrow t\bar{t} \rightarrow b\bar{b}u\bar{u}d\bar{d}$. We will omit this term in the actual calculation since only the top mass dependent terms are useful.

The term $C(ij \rightarrow kl)$ is the color term with ij being the colors of the $u\bar{u}$ pair and kl being the colors of the $t\bar{t}$ pair. λ_{ij}^a and λ_{kl}^b are the Gell-Mann SU(3) matrices with $a, b = 1, 2, \dots, 8$. For completeness we will average over the initial state colors and sum over the final state colors, but we will ignore this constant as well in the final expression of the probability density for the same reason given for term A .

The term I represents the $u\bar{u}$ and gluon vertex. The term P_g is the denominator of the gluon propagator between $u\bar{u}$ and $t\bar{t}$.

The term T is the product of the $t\bar{t}g$, tbW^+ and $\bar{t}bW^-$ vertices with the numerators of the top quark and the antitop quark propagators. The terms P_t and $P_{\bar{t}}$ are the denominators of the top quark and the antitop quark propagators.

The terms W_1 and W_2 represent the $W^+u\bar{d}$ and $W^-d\bar{u}$ vertices. The terms P_{W_1} and P_{W_2} are the denominators of the W^+ and W^- propagators. We have used the Feynman gauge for the W boson propagator.

The Dirac gamma matrices γ^μ are defined in the Dirac representation as shown in Equation 4-13, where $\sigma^\mu = (1, \vec{\sigma})$ and $\bar{\sigma}^\mu = (1, -\vec{\sigma})$. $\vec{\sigma}$ are the Pauli spin matrices.

$$\gamma^\mu = \begin{pmatrix} 0 & \sigma^\mu \\ \bar{\sigma}^\mu & 0 \end{pmatrix}, \quad \gamma^5 = \begin{pmatrix} -1 & 0 \\ 0 & 1 \end{pmatrix} \quad (4-13)$$

In general, the solutions of the Dirac equation for positive frequencies, $u(p)$, and for negative frequencies, $v(p)$, for any spin states ξ (or η for antiparticles) can be written as in Equation 4-14.

$$u(p) = \begin{pmatrix} \sqrt{p \cdot \sigma} \xi \\ \sqrt{p \cdot \bar{\sigma}} \xi \end{pmatrix}, \quad v(p) = \begin{pmatrix} \sqrt{p \cdot \sigma} \eta \\ -\sqrt{p \cdot \bar{\sigma}} \eta \end{pmatrix} \quad (4-14)$$

In the high-energy limit (or the massless limit) the solutions to the Dirac equation can be written as in Equation 4-15.

$$u(p) = \sqrt{2E_p} \begin{pmatrix} \frac{1}{2}(1 - \hat{p} \cdot \vec{\sigma})\xi \\ \frac{1}{2}(1 + \hat{p} \cdot \vec{\sigma})\xi \end{pmatrix}, v(p) = \sqrt{2E_p} \begin{pmatrix} \frac{1}{2}(1 - \hat{p} \cdot \vec{\sigma})\eta \\ -\frac{1}{2}(1 + \hat{p} \cdot \vec{\sigma})\eta \end{pmatrix} \quad (4-15)$$

The presence of the operator $\hat{p} \cdot \vec{\sigma}$ will project the spin states along the direction of movement defined by \hat{p} . For a particle traveling in the direction defined by the polar angle θ and by the azimuthal angle ϕ , the spin states along this direction are shown in Equation 4-16.

$$\xi(\uparrow) = \begin{pmatrix} \cos\frac{\theta}{2} \\ e^{i\phi}\sin\frac{\theta}{2} \end{pmatrix}, \xi(\downarrow) = \begin{pmatrix} -e^{-i\phi}\sin\frac{\theta}{2} \\ \cos\frac{\theta}{2} \end{pmatrix} \quad (4-16)$$

For an antiparticle we have that $\eta(\uparrow) = \xi(\downarrow)$ and $\eta(\downarrow) = -\xi(\uparrow)$. These spin states satisfy the Equation 4-17.

$$\begin{cases} (\hat{p} \cdot \vec{\sigma})\xi(\uparrow) = \xi(\uparrow) & \text{and} & (\hat{p} \cdot \vec{\sigma})\xi(\downarrow) = -\xi(\downarrow) \\ (\hat{p} \cdot \vec{\sigma})\eta(\uparrow) = -\eta(\uparrow) & \text{and} & (\hat{p} \cdot \vec{\sigma})\eta(\downarrow) = \eta(\downarrow) \end{cases} \quad (4-17)$$

Using Equations 4-15 and 4-17, we can rewrite in Equation 4-18 the 4-vectors W_1 and W_2 from Equation 4-12.

$$\begin{aligned} W_1 &= \bar{u}(q_u)\gamma_\alpha(1 - \gamma^5)v(q_d) = 2\sqrt{2E_u}\sqrt{2E_d}\xi_u^\dagger(\downarrow)\bar{\sigma}_\alpha\xi_d(\downarrow) = (W_1)_\alpha \\ W_2 &= \bar{u}(q_d)\gamma_\rho(1 - \gamma^5)v(q_u) = 2\sqrt{2E_d}\sqrt{2E_u}\xi_d^\dagger(\downarrow)\bar{\sigma}_\rho\xi_u(\downarrow) = (W_2)_\rho \end{aligned} \quad (4-18)$$

Also the tensor in term T from Equation 4-12 can be rewritten in the form given by Equation 4-19.

$$T = 4\sqrt{2E_b}\sqrt{2E_{\bar{b}}} \begin{pmatrix} \xi_b^\dagger(\downarrow)\bar{\sigma}^\alpha & 0 \end{pmatrix} (\not{p}_t\gamma_\mu\not{p}_{\bar{t}} + m^2\gamma_\mu) \begin{pmatrix} 0 \\ \bar{\sigma}^\rho\xi_{\bar{b}}^\dagger(\downarrow) \end{pmatrix} \quad (4-19)$$

We assume that the incoming partons travel along the z -axis, with the proton going in the positive direction. For the final expression of the probability density given in

Equation 4-6, we will need to sum over all the possible spin configurations of the initial state. We find two non-zero contributions corresponding to the situations when the incoming partons have the same handedness. Therefore for the term I from Equation 4-12 is expressed in Equation 4-20.

$$I = \bar{v}(p_{\bar{u}})\gamma^\mu u(p_u) = \begin{cases} I_{RR}^\mu = \sqrt{2E_u^{in}}\sqrt{2E_{\bar{u}}^{in}} (0, 1, i, 0) \\ I_{LL}^\mu = \sqrt{2E_u^{in}}\sqrt{2E_{\bar{u}}^{in}} (0, 1, -i, 0) \end{cases} \quad (4-20)$$

In principle, we need to average over all the possible spin configurations of the final state. The Equations 4-18 and 4-19 represent the non-zero contributions. Using Equations 4-18, 4-19 and 4-20, the product of the terms I , T , W_1 and W_2 is given in Equation 4-21.

$$I \cdot T \cdot W_1 \cdot W_2 = E \times M_{RR,LL} \quad (4-21)$$

From Equation 4-21, the term E proportional to the product of the energies of all particles, incoming or outgoing, is shown in Equation 4-22.

$$E = 2^4 \sqrt{2E_b} \sqrt{2E_{\bar{b}}} \sqrt{2E_u} \sqrt{2E_{\bar{d}}} \sqrt{2E_d} \sqrt{2E_{\bar{u}}} \sqrt{2E_u^{in}} \sqrt{2E_{\bar{u}}^{in}} \quad (4-22)$$

$$M_{RR,LL} = \begin{pmatrix} \xi_b^\dagger(\downarrow) (W_1 \cdot \vec{\sigma}) & 0 \end{pmatrix} (\not{p}_t \not{A}_{RR,LL} \not{p}_{\bar{t}} + m^2 \not{A}_{RR,LL}) \begin{pmatrix} 0 \\ (W_2 \cdot \vec{\sigma}) \xi_{\bar{b}}^\dagger(\downarrow) \end{pmatrix} \quad (4-23)$$

The terms M_{RR} and M_{LL} , shown in Equation 4-23, are calculated in a C++ code using Equation 4-15 and the matrix algebra. Therefore we can write down the expression of the matrix element squared from Equation 4-6 in the form of Equation 4-24.

$$|\mathcal{M}|^2 \rightarrow \frac{1}{2^6} \sum_{\substack{\text{spins} \\ \text{colors}}} |\mathcal{M}|^2 = \frac{|A|^2 \cdot C \cdot |E|^2}{2^6} \widetilde{P}_g \cdot \widetilde{P}_t \cdot \widetilde{P}_{\bar{t}} \cdot \widetilde{P}_{W_1} \cdot \widetilde{P}_{W_2} \cdot (|M_{RR}|^2 + |M_{LL}|^2) \quad (4-24)$$

The factors entering the final expression of the matrix element squared from Equation 4–24 are detailed in Equation 4–25.

$$\begin{aligned}
C &= \frac{1}{9} \sum_{i,j,k,l=1}^3 \lambda_{ij}^a \lambda_{kl}^a \times 3^6 = 2 \times 3^4 \\
\widetilde{P}_g &= |P_g|^2 = \frac{1}{(p_u + p_{\bar{u}})^4} \\
\widetilde{P}_t &= |P_t|^2 = \frac{1}{(p_t^2 - m^2)^2 + m^2 \Gamma_t^2} \\
\widetilde{\tilde{P}}_t &= |P_t|^2 = \frac{1}{(p_t^2 - m^2)^2 + m^2 \Gamma_t^2} \\
\widetilde{P}_{W_1} &= |P_{W_1}|^2 = \frac{1}{(P_{W_+}^2 - M_W^2)^2 + M_W^2 \Gamma_W^2} \\
\widetilde{P}_{W_2} &= |P_{W_2}|^2 = \frac{1}{(P_{W_-}^2 - M_W^2)^2 + M_W^2 \Gamma_W^2}
\end{aligned} \tag{4-25}$$

4.4 Transfer Functions

These functions are defined as the probability for a parton of energy E_p to be associated to a jet of energy E_j . The transfer functions term present in Equation 4–6 is in fact a product of six terms, one for each of the final state quarks: two for the b -quarks and four for the decay products of the W -boson. The probability density for the transfer functions is given in Equation 4–26.

$$TF(\vec{j}|\vec{p}) \rightarrow \prod_{i=1}^6 TF(\vec{j}_i|\vec{p}_i) \tag{4-26}$$

For each jet in the final state we assume that the jet angles are in fact the angles of the parton that went on to form the jet. Therefore we can write Equation 4–27 to express the transfer functions in a more general way.

$$TF(\vec{j}_i|\vec{p}_i) = TF(j_i|p_i) j_i^2 \delta^{(2)}(\Omega_{J_i} - \Omega_{P_i}) \tag{4-27}$$

The transfer function depends both on the jet energy and on the parton energy. This bi-dimensional dependence can be projected either on the jet axis to obtain the *jet-to-parton* type of transfer functions or on the parton axis to obtain the *parton-to-jet* type.

We use the second type, *parton-to-jet*. That is for a given parton energy p we build a probability to produce a jet of energy j normalized as shown in Equation 4–28.

$$\int TF(\vec{j}|\vec{p}_i)d\vec{j}_i = 1 = \int TF(j_i|p_i) j_i^2 dj_i \quad (4-28)$$

In order to assure Lorentz invariance for transfer functions we will make a change of variables $j \rightarrow \xi = 1 - j/p$. Therefore the transfer functions we will use are $\widetilde{TF}(\xi_i|p_i)$ and Equation 4–29 gives their normalization.

$$\int \widetilde{TF}(\xi_i|p_i)d\xi_i = 1 = \int \widetilde{TF}(\xi(j_i)|p_i) \frac{-1}{p_i} dj_i \quad (4-29)$$

We can write the Equation 4–26 again with the full expression entering Equation 4–6 holding the probability density for the $t\bar{t}$ all hadronic process.

$$TF(\vec{j}|\vec{p}) \rightarrow \prod_{i=1}^6 TF(\vec{j}_i|\vec{p}_i) = \prod_{i=1}^6 \widetilde{TF}(\xi(j_i)|p_i) \frac{-1}{p_i} \delta^{(2)}(\Omega_{J_i} - \Omega_{P_i}) \quad (4-30)$$

The transfer functions $\widetilde{TF}(\xi_i|p_i)$ are built using $t\bar{t}$ Monte Carlo samples. More exactly, a jet is associated to a parton if its direction is within a cone of $\Delta R = 0.4$ around the parton direction. We say that a jet is *matched* to the parton if no other jet should satisfy this geometrical requirement. We call an event as being a *matched* event if each of the six partons in the final state has a different jet matched to it. Of all the $t\bar{t}$ Monte Carlo events passing the kinematical selection defined later in section 5, about 50% are matched events.

The jets formed by the decay partons of the W -bosons have a different energy spectrum than the jets originating from the b -quarks. Thus we form different sets of transfer functions depending on the flavor of the parton the jet has been matched to.

The transfer functions are described using a parameterization in bins of the parton energies and of the parton pseudo-rapidities. Table 4–1 shows the definition of the binning in pseudo-rapidity. The same definition holds for b -jet transfer function and for W -jets transfer functions.

The binning in parton energy is defined such that each bin contains at least 3000 entries and it is wider than 5 GeV. This is done in each bin of pseudo-rapidity. Table 4-2 shows the definition of energy binning for the b -jets transfer functions, while Table 4-3 is for the W -jets transfer functions.

In each bin the transfer function is represented by the distribution of the variable $1 - E_{jet}/E_{parton}$. The shape of this distribution is fitted to the sum of two gaussians. Appendix C holds the fitted shapes.

4.5 Transverse Momentum of the $t\bar{t}$ System

The $P_T(\vec{p})$ weight is written as dependent on the 4-vectors of the partons in the final state, generically represented by \vec{p} in the argument of the function. This dependence is difficult to parameterize. Therefore we will pick a more natural set of parameters to work with. In the next section we will detail the change of variables needed to accommodate this simplification. Until then we anticipate that the variables used for integration in Equation 4-6 are p_x^6 and p_y^6 , representing the projections of the transverse momentum of the $t\bar{t}$ system along the x and y axes. The probability density related to the transverse momentum of the $t\bar{t}$ system weight is shown in Equation 4-31.

$$P_T(\vec{p}) \rightarrow P_T(p_x^6, p_y^6) \quad (4-31)$$

The parameters we actually use are the magnitude of the transverse momentum of the $t\bar{t}$ system, p_T^6 , and the azimuthal angle, ϕ_T^6 . The upper index means that these parameters are determined using the 6 partons in the final state. We expect to have a flat dependence on ϕ_T^6 and therefore we can factorize the two dependences. The Equation 4-32 gives the normalization relation.

$$\int dp_T^6 d\phi_T^6 \hat{P}_T(p_T^6, \phi_T^6) = 1 = \int dp_T^6 \tilde{P}_T(p_T^6) \int d\phi_T^6 \Phi_T^6 \quad (4-32)$$

The transverse momentum spectrum of the $t\bar{t}$ events, represented by $\tilde{P}_T(p_T^6)$ in the Equation 4-32, is obtained from a $t\bar{t}$ Monte Carlo sample with $M_{top} = 178$ GeV. The

shape of this distribution is normalized to unity and therefore we have in Equation 4-33 the value for Φ_T^6 .

$$\int dp_T^6 \tilde{P}_T(p_T^6) = 1, \quad \Phi_T^6 = \frac{1}{2\pi} \quad (4-33)$$

As mentioned before we need to express everything in terms of p_x^6 and p_y^6 . This can be done just by changing the variables from the polar to the Cartesian coordinates as shown in Equation 4-34.

$$\begin{aligned} \int dp_T^6 d\phi_T^6 \tilde{P}_T(p_T^6) \frac{1}{2\pi} = 1 &= \int dp_x^6 dp_y^6 \frac{\tilde{P}_T\left(p_T^6 = \sqrt{(p_x^6)^2 + (p_y^6)^2}\right)}{\sqrt{(p_x^6)^2 + (p_y^6)^2}} \frac{1}{2\pi} = \\ &= \int dp_x^6 dp_y^6 P_T(p_x^6, p_y^6) \end{aligned} \quad (4-34)$$

We can now write in Equation 4-35 the full expression of the transverse momentum of the $t\bar{t}$ system weight.

$$P_T(\vec{p}) \rightarrow P_T(p_x^6, p_y^6) = \frac{\tilde{P}_T\left(p_T^6 = \sqrt{(p_x^6)^2 + (p_y^6)^2}\right)}{\sqrt{(p_x^6)^2 + (p_y^6)^2}} \frac{1}{2\pi} \quad (4-35)$$

The shape of $\tilde{P}_T(p_T^6)$ has a slight dependence on the top mass, but it turns out that choosing the shape obtained with $M_{top} = 178$ GeV doesn't introduce a significant bias in the final mass reconstruction. See Appendix B for the mass dependence of this shape. In Figure 4-2 the shape of the transverse momentum of the $t\bar{t}$ events is shown fitted to a sum of 3 gaussians.

4.6 Implementation and Evaluation of the Probability Density

The last expression of the probability density was given by Equation 4-6. The sections 4.3, 4.4 and 4.5 offered details on the expressions of several important pieces entering the probability density. Using Equations 4-24, 4-30 and 4-35, we can write in Equation 4-36 the new expression for the probability density.

$$\begin{aligned}
P(j|m) = & \sum_{combi} \int \frac{dz_a dz_b f(z_a) f(z_b)}{4E_a E_b |v_a - v_b|} \int \prod_{i=1}^6 \left[\frac{d^3 \vec{p}_i}{(2\pi)^3 2E_i} \right] \frac{(2\pi)^4 \delta^{(4)}(E_{fin} - E_{ini})}{\sigma_{tot}(m) \epsilon(m) N_{combi}} \times \\
& \times \frac{|A|^2 \cdot C \cdot |E|^2}{2^6} \widetilde{P}_g \cdot \widetilde{P}_t \cdot \widetilde{P}_{\bar{t}} \cdot \widetilde{P}_{W_1} \cdot \widetilde{P}_{W_2} \cdot (|M_{RR}|^2 + |M_{LL}|^2) \times \\
& \times \prod_{i=1}^6 \left[\frac{(-\widetilde{TF}(\xi(j_i)|p_i))}{p_i} \delta^{(2)}(\Omega_{J_i} - \Omega_{P_i}) \right] \cdot \frac{\widetilde{P}_T \left(p_T^6 = \sqrt{(p_x^6)^2 + (p_y^6)^2} \right)}{2\pi \sqrt{(p_x^6)^2 + (p_y^6)^2}} \quad (4-36)
\end{aligned}$$

As mentioned previously, we will not use any constant that can be factored out in the expression of the probability density. From now on we will omit all such constants except for the number of combinations, N_{combi} . Also in the argument of \widetilde{P}_T we will put just p_T^6 , but it should be understood $\sqrt{(p_x^6)^2 + (p_y^6)^2}$ which in turn should be understood as a function of the 4-vectors of the final state partons.

We will move to spherical coordinates in the integration over the partons momenta. Due to the assumption that the angles of the partons are known as the measured angles of the jets, made explicit by the delta functions, $\delta^{(2)}(\Omega_{J_i} - \Omega_{P_i})$, all the integrals after the angles will be dropped together with the aforementioned delta functions. Also we use ξ_i instead of $\xi(j_i)$ in the argument of \widetilde{TF} .

One should notice that $|E|^2$ is divided out by the energy factors in the denominator as seen in Equation 4-37.

$$\begin{aligned}
P(j|m) = & \sum_{combi} \int \frac{dz_a dz_b f(z_a) f(z_b)}{|v_a - v_b| \sigma_{tot}(m) \epsilon(m) N_{combi}} \int \prod_{i=1}^6 \left[dp_i p_i \widetilde{TF}(\xi_i|p_i) \right] \times \\
& \times \frac{\widetilde{P}_T(p_T^6)}{p_T^6} \cdot \widetilde{P}_g \cdot \widetilde{P}_t \cdot \widetilde{P}_{\bar{t}} \cdot \widetilde{P}_{W_1} \cdot \widetilde{P}_{W_2} \cdot (|M_{RR}|^2 + |M_{LL}|^2) \cdot \delta^{(4)}(E_{fin} - E_{ini}) \quad (4-37)
\end{aligned}$$

To reduce the number of integrals we will work in the narrow width approximation for the W -bosons. This translates in two more delta functions arising from the square of the W -boson propagators as shown by Equation 4-38.

$$\widetilde{P}_W = \frac{1}{(P_W^2 - M_W^2)^2 + M_W^2 \Gamma_W^2} \xrightarrow{\Gamma_W \ll M_W} \delta(P_W^2 - M_W^2) \frac{\pi}{M_W \Gamma_W} \quad (4-38)$$

Considering the high-energy limit, we have that the invariant mass of the W -boson decay products is given by Equation 4-39. $\Omega_{1,2}$ is a generic notation for the polar, $\theta_{1,2}$, and the azimuthal, $\phi_{1,2}$, angles of the two decay products. $\Delta\eta_{12}$ is the difference in pseudo-rapidities of the two decay partons and $\Delta\phi_{12} = \phi_1 - \phi_2$.

$$P_W^2 = 2p_1p_2\sin\theta_1\sin\theta_2(\cosh\Delta\eta_{12} - \cos\Delta\phi_{12}) = 2p_1p_2\omega_{12}(\Omega_1, \Omega_2) \quad (4-39)$$

Making the change of variables $P_W^2 \rightarrow p_1$, the Equation 4-38 can be written as a delta function depending on the energy of one of the W -boson decay partons as shown in Equation 4-40, where $p_1^0 = M_W^2/(2p_2\omega_{12})$.

$$\widetilde{P}_W \xrightarrow{\Gamma_W \ll M_W} \frac{\pi}{M_W \Gamma_W} \frac{1}{2p_2\omega_{12}(\Omega_1, \Omega_2)} \delta(p_1 - p_1^0) \quad (4-40)$$

The mass of the W -boson is 80.4 GeV and its width is 2.1 GeV. Without these new constants and using the expression from Equation 4-40 for both W -boson squared propagators, we can write in Equation 4-41 the probability density.

$$P(j|m) = \sum_{combi} \int \frac{dz_a dz_b f(z_a) f(z_b)}{|v_a - v_b| \sigma_{tot}(m) \epsilon(m) N_{combi}} \int dp_b dp_{\bar{b}} dp_2 dp_4 \frac{p_b p_{\bar{b}}}{p_2 p_4} \frac{\widetilde{P}_T(p_T^6)}{p_T^6} \times \\ \times \prod_{i=1}^6 \left[\widetilde{TF}(\xi_i | p_i) \right] \cdot \widetilde{P}_g \cdot \widetilde{P}_t \cdot \widetilde{P}_{\bar{t}} \cdot \frac{(|M_{RR}|^2 + |M_{LL}|^2)}{(\omega_{12})^2 (\omega_{34})^2} \cdot \delta^{(4)}(E_{fin} - E_{ini}) \quad (4-41)$$

When we calculated the matrix element in section 4.3 we assumed that the incoming partons were traveling along the z -axis. This means their transverse momentum is zero. Therefore the energy conservation is violated in the transverse coordinates since based on Figure 4-2 we considered non-zero transverse momentum for the $t\bar{t}$ system. However, we expect this to be a small effect covered by the uncertainty on the parton distribution functions of the proton and of the antiproton. Anyway, we need ignore the delta functions requiring energy conservation along the x and y axes as shown in Equation 4-42.

$$\begin{aligned}
\delta^{(4)}(E_{fin} - E_{ini}) &\rightarrow \delta\left(E_a + E_b - \sum_{i=1}^6 p_i\right) \delta\left(p_a^z + p_b^z - \sum_{i=1}^6 p_i^z\right) = \\
&= \delta\left(p_u + p_{\bar{u}} - \sum_{i=1}^6 p_i\right) \delta\left(p_u - p_{\bar{u}} - \sum_{i=1}^6 p_i^z\right) \quad (4-42)
\end{aligned}$$

In Equation 4-41, we made the change of variables $z_a \rightarrow p_u$ and $z_b \rightarrow p_{\bar{u}}$ given that $z_a = p_u/p_{proton}$ and $z_b = p_{\bar{u}}/p_{antiproton}$. The values of the proton and antiproton momenta, p_{proton} and $p_{antiproton}$, are constant and from now on we will drop them from any expressions. In the high-energy limit we will have $|v_a - v_b| = 2c$ and therefore we will omit this term as well. In preparation for this change of variables, we write in Equation 4-43 the expression for the energy-conserving delta function, where $p_u^0 = \sum_{i=1}^6 p_i(1 + \cos\theta_i)/2$ and $p_{\bar{u}}^0 = \sum_{i=1}^6 p_i(1 - \cos\theta_i)/2$.

$$\begin{aligned}
\delta^{(4)}(E_{fin} - E_{ini}) &\rightarrow \delta\left(p_u + p_{\bar{u}} - \sum_{i=1}^6 p_i\right) \delta\left(p_u - p_{\bar{u}} - \sum_{i=1}^6 p_i \cos\theta_i\right) = \\
&= \frac{1}{2} \delta(p_u - p_u^0) \delta(p_{\bar{u}} - p_{\bar{u}}^0) \quad (4-43)
\end{aligned}$$

Using all of the above, the expression for the probability density is given by Equation 4-44 in an almost final form.

$$\begin{aligned}
P(j|m) &= \frac{1}{\sigma_{tot}(m)\epsilon(m)N_{combi}} \sum_{combi} \int dp_b dp_{\bar{b}} dp_2 dp_4 \frac{p_b p_{\bar{b}} f(p_u^0) f(p_{\bar{u}}^0)}{(\omega_{12})^2 (\omega_{34})^2 p_2 p_4} \times \\
&\times \prod_{i=1}^6 \left[\widetilde{TF}(\xi_i | p_i) \right] \cdot \frac{\widetilde{P}_T(p_T^6)}{p_T^6} \cdot \widetilde{P}_g \cdot \widetilde{P}_t \cdot \widetilde{P}_{\bar{t}} \cdot (|M_{RR}|^2 + |M_{LL}|^2) \quad (4-44)
\end{aligned}$$

In section 4.5, we announced our preference to integrate over the x and y components of the momentum of the $t\bar{t}$ system. That is accomplished by a last change of variables $\{p_b, p_{\bar{b}}\} \rightarrow \{p_x^6, p_y^6\}$ whose Jacobian, $J(b \rightarrow 6)$, is given by Equation 4-45.

$$J(b \rightarrow 6) = \frac{1}{\sin\theta_b \sin\theta_{\bar{b}} (\cos\phi_b \sin\phi_{\bar{b}} - \sin\phi_b \cos\phi_{\bar{b}})} \quad (4-45)$$

The Jacobian is obtained by solving a system of equations for p_b and $p_{\bar{b}}$. The relations entering the system of equations are shown in Equation 4-46.

$$\begin{cases} p_x^6 = p_b \cos \phi_b \sin \theta_b + p_{\bar{b}} \cos \phi_{\bar{b}} \sin \theta_{\bar{b}} + \sum_{i=3}^6 p_i^x \\ p_y^6 = p_b \sin \phi_b \sin \theta_b + p_{\bar{b}} \sin \phi_{\bar{b}} \sin \theta_{\bar{b}} + \sum_{i=3}^6 p_i^y \end{cases} \quad (4-46)$$

We can then write in Equation 4-47 the expression of the probability density in its final form which is used inside a C++ code.

$$\begin{aligned} P(j|m) = & \sum_{combi} \int \frac{dp_x^6 dp_y^6 dp_2 dp_4}{\sigma_{tot}(m) \epsilon(m) N_{combi}} \frac{J(b \rightarrow 6) p_b p_{\bar{b}} f(p_u^0) f(p_{\bar{u}}^0)}{(\omega_{12})^2 (\omega_{34})^2 p_2 p_4} \times \\ & \times \prod_{i=1}^6 \left[\widetilde{TF}(\xi_i | p_i) \right] \cdot \frac{\widetilde{P}_T(p_T^6)}{p_T^6} \cdot \widetilde{P}_g \cdot \widetilde{P}_t \cdot \widetilde{P}_{\bar{t}} \cdot (|M_{RR}|^2 + |M_{LL}|^2) \end{aligned} \quad (4-47)$$

The integration is performed by simply giving values to the 4 integration variables and then by adding up the integrand obtained at each step. The limits of the integration are -60 GeV \rightarrow 60 GeV for $p_{x,y}^6$ and 10 GeV \rightarrow 300 GeV for $p_{2,4}$. The step of integration is 2 GeV. Given these limits, at each step of integration we have to check the physicality of the components entering Equation 4-47. The probability density is evaluated for top mass values going in 1 GeV increments from 125 GeV \rightarrow 225 GeV.

The dependence on mass of the $t\bar{t}$ cross-section is obtained from values calculated by CompHep Monte Carlo generator for the processes $u\bar{u} \rightarrow t\bar{t}$, $d\bar{d} \rightarrow t\bar{t}$ and $gg \rightarrow t\bar{t}$. The absolute values for these cross sections are not as important as their top mass dependence. Figure 4-1 shows this dependence.

For the proton and antiproton PDF, $f(p_u^0) f(p_{\bar{u}}^0)$, we will use the CTEQ5L distributions with the scale corresponding to 175 GeV. The shapes are given in Appendix A. The $t\bar{t}$ acceptance, $\epsilon(m)$, depends on the top mass and will be described later when the event selection is addressed.

The final expression of the probability density has been given and its implementation has been detailed. The following section is dedicated to the checks we performed in order to assure the proper functionality of the matrix element technique.

4.7 Checks of the Matrix Element Calculation

The event probability described in the section 4.6 depends on the top quark pole mass and is expected to be minimized in negative log scale around the true masses in the event. Multiplying all the event probabilities we obtain a likelihood function that depends on the top pole mass. Equation 4-48 shows the expression of the likelihood.

$$L(M_{top}) = \prod_{events} P(j|M_{top}) \quad (4-48)$$

In negative log scale this likelihood is expected to have a minimum around the true pole mass, and so the top mass reconstruction can be performed. This reconstruction is the traditional matrix element top mass reconstruction. However, we only use this reconstruction to check the matrix element calculation.

We use Monte Carlo samples generated at various input top masses. Only signal events are used. For each sample, the reconstructed top mass done by using only the matrix element calculation can be plotted against the input top mass. This can be done at various levels of complexity. Ideally, we'd see a linear dependence with no bias and a unitary slope.

The first check to do is at the parton level. We take the final state partons momenta from our Monte Carlo, smear their energies and use them as jets momenta. Figure 4-5 shows a good linearity in the case of a 5% uniform smearing. There is a small bias of about 0.8 GeV, but the slope is consistent with 1. As the smearing is increased the bias becomes more evident, and slope degrades slightly. This can be also seen in Figure 4-5 for 10% smearing and for 20% smearing, respectively. In all of these situations a gaussian centered on 0 and with width equal to the amount of smearing used has been employed as a transfer function in the event probability computation.

The partons can also be smeared using the functions described in section 4.4, in which case the same functions are used as transfer functions in the event probability computation. This test makes the transition between the parton level to the jets level,

although it's still a parton level check. Figure 4-5 shows the linearity check in this case as well.

The next check is moving closer to reality by using in the reconstruction the jets that have been matched to the partons. This is already a check at the jets level and the functions defined in section 4.4 have to be used. Figure 4-6 shows the linearity check.

The final check is the most realistic we can get using only signal events, and that is we use all the events we have with disregard to whether the jets have been matched or not to the partons. Figure 4-7 shows the linearity check in this case.

All the checks we have listed above show the good performance of our matrix element calculation. In general, the traditional matrix element approach is expected to provide a better statistical uncertainty on the top mass than the template analyses. In the case of the present analysis, the traditional matrix element method does better only the reconstruction is performed on signal samples. When the background is mixed in, the template method we use has a greater sensitivity.

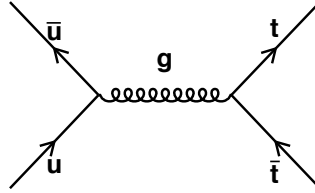


Figure 4-1. Tree level Feynman diagram for the process $u\bar{u} \rightarrow t\bar{t}$

Table 4-1. Definition of the binning of the parton pseudo-rapidity for the parameterization of the transfer functions.

Bin	$ \eta $
1	$0 \rightarrow 0.7$
2	$0.7 \rightarrow 1.3$
3	$1.3 \rightarrow 2.0$

Table 4-2. Definition of the binning of the parton energy for the b -jets transfer functions parameterization.

Bin	$0 \leq \eta < 0.7$	$0.7 \leq \eta < 1.3$	$1.3 \leq \eta \leq 2.0$
1	$10 \rightarrow 53$	$10 \rightarrow 83$	$10 \rightarrow \infty$
2	$53 \rightarrow 64$	$83 \rightarrow 111$	
3	$64 \rightarrow 74$	$111 \rightarrow \infty$	
4	$74 \rightarrow 85$		
5	$85 \rightarrow 97$		
6	$97 \rightarrow 114$		
7	$114 \rightarrow \infty$		

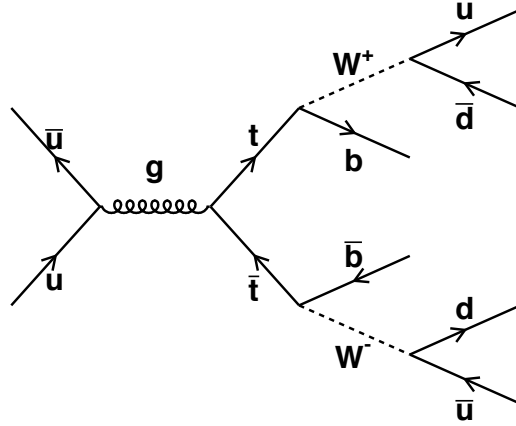


Figure 4-2. Tree level Feynman diagram for the process $u\bar{u} \rightarrow t\bar{t} \rightarrow b\bar{b}u\bar{u}d\bar{d}$

Table 4-3. Definition of the binning of the parton energy for the W -jets transfer functions parameterization.

Bin	$0 \leq \eta < 0.7$	$0.7 \leq \eta < 1.3$	$1.3 \leq \eta \leq 2.0$
1	$10 \rightarrow 32$	$10 \rightarrow 50$	$10 \rightarrow 98$
2	$32 \rightarrow 38$	$50 \rightarrow 63$	$98 \rightarrow \infty$
3	$38 \rightarrow 44$	$63 \rightarrow 76$	
4	$44 \rightarrow 49$	$76 \rightarrow 90$	
5	$49 \rightarrow 54$	$90 \rightarrow 108$	
6	$54 \rightarrow 59$	$108 \rightarrow \infty$	
7	$59 \rightarrow 64$		
8	$64 \rightarrow 69$		
9	$69 \rightarrow 75$		
10	$75 \rightarrow 81$		
11	$81 \rightarrow 89$		
12	$89 \rightarrow 99$		
13	$99 \rightarrow 113$		
14	$113 \rightarrow \infty$		

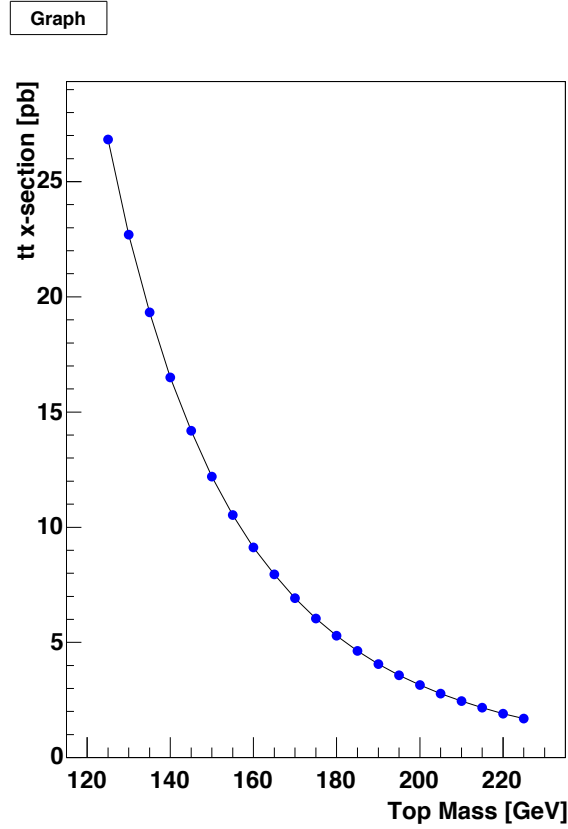


Figure 4-3. Cross section for $t\bar{t}$ production as a function of the top mass, as obtained from CompHep. The line is not a fit.

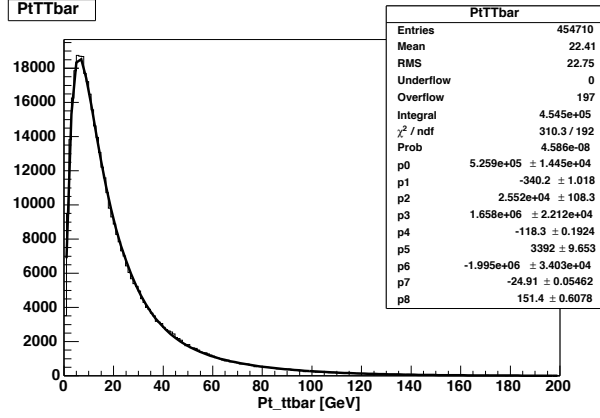
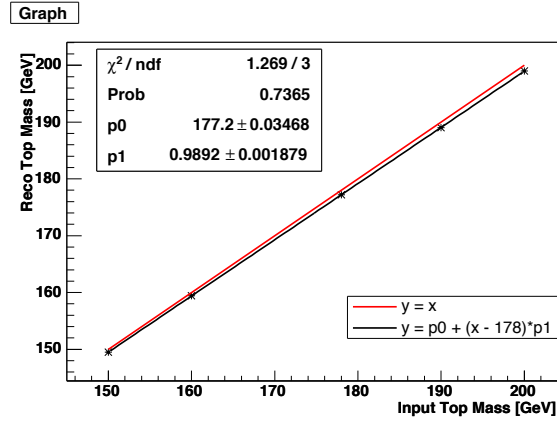
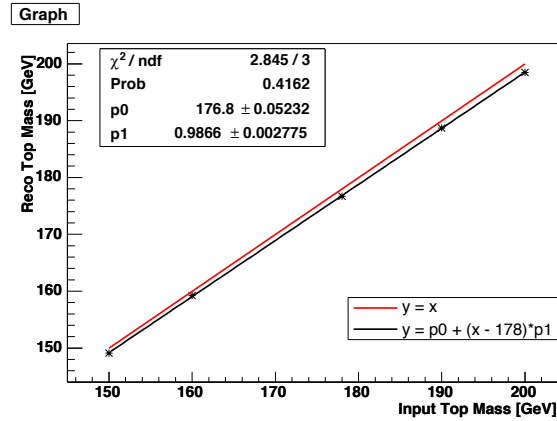


Figure 4-4. Transverse momentum of the $t\bar{t}$ events. The fit is a sum of 3 gaussians.



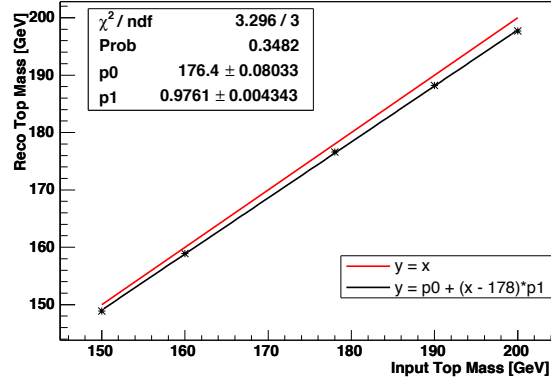
A



B

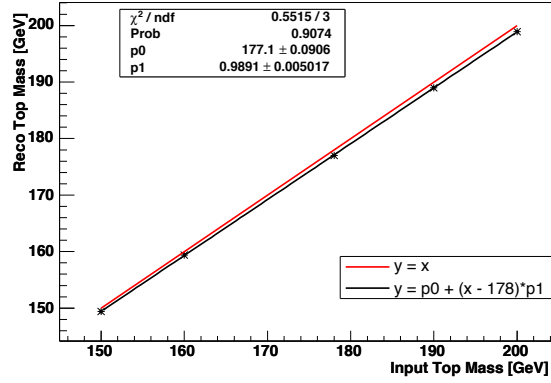
Figure 4-5. Reconstructed top mass versus input top mass at parton level. A) The energies of the partons have been smeared by 5%. B) The energies of the partons have been smeared by 10%. C) The energies of the partons have been smeared by 20%. D) The energies of the partons have been smeared using the transfer functions.

Graph



C

Graph



D

Figure 4-5. Continued

Graph

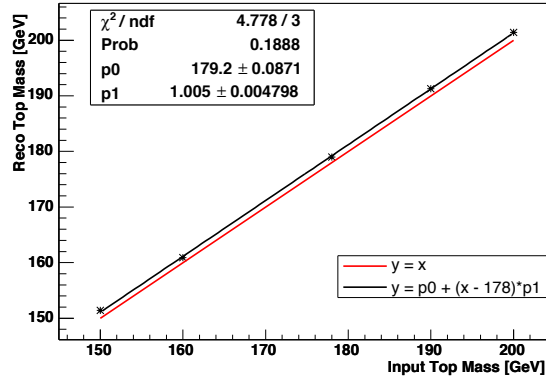


Figure 4-6. Reconstructed top mass versus input top mass using jets that were uniquely matched to partons.

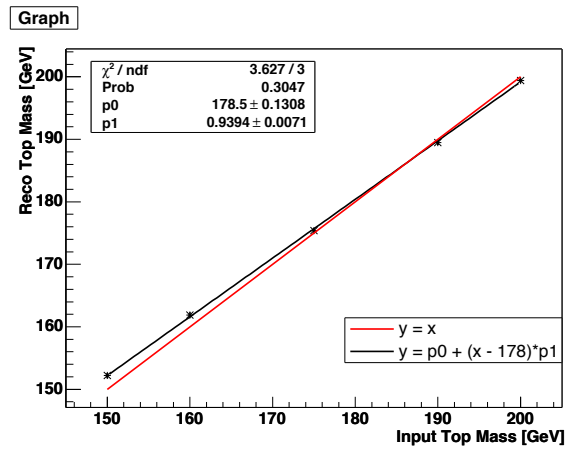


Figure 4-7. Reconstructed top mass versus input top mass using realistic jets.

CHAPTER 5 DATA SAMPLE AND EVENT SELECTION

5.1 Data and Monte Carlo Samples

The data events are the Run2 CDF multi-jet events selected with the *TOP_MULTIJET* trigger, and it amounts to approximately 943 pb^{-1} . This trigger selects about 88% of the $t\bar{t}$ all hadronic events.

The Monte Carlo samples are the official CDF samples. We use 12 different samples generated with the Herwig package to parameterize the mass dependence of our templates. The mass takes values from 150 GeV to 200 GeV in 5 GeV increments. There are also samples with a top mass of 178 GeV used to determine various systematic uncertainties: different choice of generator (in this case we used the Pythia package), different modeling of the initial state radiation (ISR) and of the final state radiation (FSR), different choice of proton parton distribution function (PDF). The background model described in section 6 is validated with the help of two Monte Carlo samples generated with the Alpgen package: one with events having $b\bar{b}+4$ light partons in the final state and another with events having 6 light partons in the final state.

5.2 Event Selection

Before describing and listing the selection cuts, we need to mention the sample composition. The multi-jet events contain beside our signal events, a multitude of backgrounds:

- QCD multi-jets
- hadronic W,Z production
- single top production
- pair production in other channels

The QCD multi-jet production has the biggest contribution, while the others can be neglected since they involve electroweak couplings.

There are three sets of cuts. The first set, clean-up cuts, is aimed at enhancing the all hadronic top content of our datasets. They are listed below:

- vertex position: $|z| < 60$ cm and $|z - z_p| < 5$ cm
- $\cancel{E}_T / \sqrt{\sum E_T} < 3$ (GeV)^{1/2}
- remove events having muons or electrons

These clean-up cuts select about 37% of the $t\bar{t}$ Monte Carlo samples out of which about 84% are all-hadronic events. In the data only 27% of the events pass these cuts, most of the events failing the good run list and the trigger cuts.

Next, the kinematical and topological cuts are applied in order to enhance the $t\bar{t}$ events over the background:

- require events with exactly 6 jets with $|\eta| < 2$ and $E_T > 15$ GeV
- $Aplanarity + 0.005 \sum E_{T3} > 0.96$
- $centrality > 0.78$
- $\sum E_T > 280$ GeV
- ≥ 1 SVX tags

where $\sum E_T$ is sum of all the transverse energies of all the six jets in the event, $\sum_3 E_T$ is the sum of all the six jets minus the two most energetic ones, *Centrality* is defined in Equation 5-1 and the *Aplanarity* is defined as 3/2 of the smallest eigenvalue of the sphericity matrix \hat{S}^{ij} . The sphericity matrix \hat{S}^{ij} is defined in Equation 5-2.

$$Centrality = \frac{\sum_{j=1}^6 (E_T)_j}{\sqrt{(\sum_{j=1}^6 (E_T)_j)^2 - (\sum_{j=1}^6 (P_z)_j)^2}} \quad (5-1)$$

$$S^{ij} = \frac{\sum_{p=1}^6 (P_p^i \times P_p^j)}{\sum_{p=1}^6 (P_p^2)}, \quad \text{where } i, j = x, y, z \quad (5-2)$$

The values of the cuts have been optimized using a $t\bar{t}$ Monte Carlo sample and a sample of background events. The background events were in fact from the multi-jet dataset passing only the clean-up cuts, so that the $t\bar{t}$ content is negligible. The details of

the optimization can be found in [50]. Table 5-1 shows the number of events in the data sample. Table 5-2 shows the number of events in a $t\bar{t}$ Monte Carlo sample with $M_{top} = 170$ GeV.

The SVX b-tagger used has a higher efficiency in the Monte Carlo than in the data. Therefore we need to degrade the number of tagged events according to the appropriate scale factor which is $SF = 0.91$. Taking this scale factor into account, and converting to the luminosity of the data, we show in Table 5-3 the signal to background ratios, S/B , for different top masses after the kinematical cuts for single and double tagged events separately. The conversion to the observed luminosity is done by using the theoretical $t\bar{t}$ cross section. The number of background events is the difference between the observed number of events in the data shown in Table 5-1 and the signal expectation.

An additional cut is introduced to further cut down the background. This new variable we cut on is the minimum of the event probability given in Equation 4-6 of section 4. Figure 5-1 shows the distribution of the minimum of the negative log event probability for a signal sample versus the background shape.

Note that the top mass value for which this event probability is minimized will be used in the final top mass reconstruction, and the value of the probability in negative log scale is used as a discriminating variable between $t\bar{t}$ and background. We denote this value as $minLKL$, and the cut definition is requiring this variable to be less than 10.

The value of this last cut has been obtained by minimizing the statistical uncertainty on the top mass value as reconstructed in section 4, that is using only the matrix element calculation. Table 5-4 shows the efficiency of this cut relative to the number of events after tagging and after the kinematical cuts, for signal at different top masses and for background. The table also shows the number of signal events corresponding to 943 pb^{-1} and the appropriate signal to background ratio.

Comparing the signal-to-background ratios S/B between Table 5-3 and Table 5-4 there is an improvement of about a factor of 3 for samples with one tagged heavy

flavor jets and about a factor of 6 for samples with two tagged heavy flavor jets. This improvement in the signal-to-background ratio will result in a better resolution in the top mass reconstruction.

Table 5-1. Number of events in the multi-jet data after the clean-up cuts, kinematical cuts and tagging. The integrated luminosity is $L = 943 \text{ pb}^{-1}$.

Cut	Events	Fraction (%)
Initial	12274958	100
$ z < 60cm$	3555054	28.9
$ z - z_p < 5cm$	3397341	27.7
Lepton Veto	3392551	27.6
$\cancel{E}_T / \sqrt{\sum E_T} < 3$	3333451	27.2
$N_{tight\ jets} = 6$	380676	3.1
Kinematic Cuts	4172	0.034
1 tag	782	6.37e-5
≥ 2 tag	148	1.21e-5

Table 5-2. Number of events in the $t\bar{t}$ Monte Carlo sample with $M_{top} = 170 \text{ GeV}$.

Cut	Events	Fraction (%)
Initial	233233	100
$ z < 60cm$	128169	55.0
$ z - z_p < 5cm$	128045	54.9
Tight Lepton Veto	113970	48.9
$\cancel{E}_T / \sqrt{\sum E_T} < 3$	88027	37.7
$N_{tight\ jets} = 6$	29485	12.6
Kinematic Cuts	5999	2.6
1 tag	2603	1.1
≥ 2 tag	1599	0.69

Table 5-3. Number of events and expected signal to background ratios for the $t\bar{t}$ Monte Carlo samples with top masses between 150 GeV and 200 GeV for a luminosity of $L = 943 \text{ pb}^{-1}$. The number of data events is shown too. These events are passing the kinematical selection, but not the minimum likelihood cut.

M_{top} (GeV/c ²)	Single Tag	S/B	Double Tag	S/B
150	73	1/10	45	1/2
155	72	1/10	46	1/2
160	74	1/10	45	1/2
165	74	1/10	48	1/2
170	74	1/10	49	1/2
175	71	1/10	47	1/2
178	75	1/9	50	1/2
180	69	1/10	47	1/2
185	67	1/11	44	1/2
190	61	1/12	43	1/2
195	59	1/12	39	1/3
200	56	1/13	38	1/3
Data Events	782	-	148	-

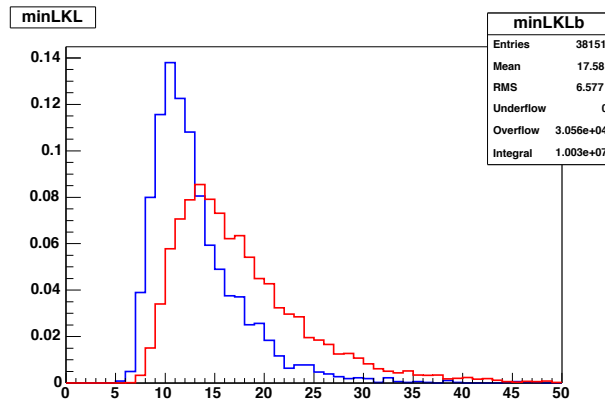


Figure 5-1. Minimum of the negative log event probability. In blue it's shown the curve for $t\bar{t}$ sample of $M_{top} = 175 \text{ GeV}$, while in red it's shown the background shape.

Table 5-4. Number of events, $minLKL$ cut efficiency (ϵ) relative to the kinematical cuts and the signal to background ratios for the $t\bar{t}$ Monte Carlo samples with top masses between 150 GeV and 200 GeV for a luminosity of 943 pb^{-1} . These events pass all the cuts. The efficiency for background events is also shown.

M_{top} (GeV/ c^2)	Single Tag	ϵ	S/B	Double Tag	ϵ	S/B
150	18	0.25	1/2	14	0.32	3/1
155	17	0.23	1/2	15	0.33	4/1
160	16	0.21	1/2	14	0.31	3/1
165	16	0.22	1/2	14	0.3	4/1
170	15	0.2	1/2	14	0.29	4/1
175	13	0.19	1/3	14	0.29	3/1
178	14	0.18	1/3	14	0.28	4/1
180	12	0.18	1/3	13	0.27	3/1
185	11	0.16	1/3	11	0.26	3/1
190	9	0.15	1/4	11	0.25	3/1
195	9	0.15	1/4	10	0.25	2/1
200	7	0.12	1/5	8	0.22	2/1
Background	-	0.05	-	-	0.04	-
Data Events	48	-	-	24	-	-

CHAPTER 6 BACKGROUND MODEL

6.1 Definition

After all the cuts the background events represent at least half of the whole sample. Therefore we need to have a good description of these events. There are two things we have to understand well: the shape of the distributions and the number of such events.

Since there is no cross section measurement of this background, and also, the composition of our data sample hasn't been determined at CDF, we define the expected number of background events as the difference between the total number of events observed in the data and the expected number of $t\bar{t}$ events based on the Standard Model.

The shape of the background events can be determined with the help of our Monte Carlo samples. However, due the small statistics of this samples, we will be forced to re-sample heavily when we will perform the sensitivity studies of our technique. In order to overcome that, we will form a sample of background-like events using data events from a sample quasi-dominated by background. Then we'll make sure that the shape of this data-driven background model corresponds to the shape from Monte Carlo background events.

To form the data-driven background events, we start with our pretag data events before the minimum likelihood cut, but after all the clean-up and kinematical cuts. In this sample the signal to background ratio is about 1/25. Then we start to randomly b -tag the jets of these events by using the b -tag rates of the mistag matrix defined in the all hadronic cross-section analysis [51]. Each event can end up in any of the possible tagged configurations by having a number of tagged jets between 0 and 6. We iterate this artificial b -tagging procedure many times keeping all the configurations that have at least one b -tagged jet. Some configurations will appear multiple times in this process, and we will use it that often in our studies as if it were a distinct configuration. The

reason behind this is to preserve the tag rates determined by the mistag matrix, which by definition are the rates in the background events.

We start with around 2,600 multi-jet data events which passed only the kinematical cuts without requiring the presence of a heavy flavor jet. We apply our b -tag procedure for 20,000 times, and we end up with approximately 9 million configurations with only one heavy flavor jet and 1 million configurations with only two heavy flavor jets in the final sample. Only about 13,000 single tagged configurations and about 27,000 double tagged configurations are indeed distinct.

6.2 Validation of the Background Model

To validate the background model proposed in the previous section, we check the shapes of several variables of interest in two control regions and in the signal region. The three regions are defined as follows:

- **Control Region 1:** events passing the clean-up cuts
- **Control Region 2:** events passing the kinematical cuts
- **Signal Region:** events passing all the cuts

6.2.1 Validation in Control Region 1

The mistag matrix used for the background model is based on the tagging rates of the data sample with 4 tight jets and passing all the other clean-up cuts. This check is meant to validate our assumption that the mistag rates from the 4-jet bin can be used to predict the mistag rates in the 6-jet bin. We do this by comparing the observed rates in the data sample passing the clean-up cuts with the predicted rates for this sample based on the mistag matrix. Figure 6-1 shows the comparison in the exclusive single tagged sample, while Figure 6-2 shows the comparison in the inclusive double tagged sample. The variables chosen for this comparison are the transverse energies, pseudo-rapidity and the polar angle of the jets, and the number of vertices, sum of the transverse energies of the

leading six jets, and of the sub-leading four jets, aplanarity and centrality as defined in section 5.

6.2.2 Validation in Control Region 2

We compare shapes between our background model for this region and a Monte Carlo background. The background model for this region is formed by taking the pretag data sample in this kinematical region and by using the mistag matrix to obtain the tag rates. The Monte Carlo sample used has $b\bar{b} + 4$ light partons in its final state.

One variable we can look at is the sum of the event probabilities as defined in section 4 using the matrix element. The sum is between a top mass equal to 125 GeV up to 225 GeV in steps of 1 GeV. Figure 6-3 shows the shapes of Monte Carlo background and of the data-driven background.

Another interesting variable is the invariant mass of all the untagged pairs of jets in the event. Figure 6-4 shows this variable for the tagged events before the $minLKL$ cut, while Figure 6-5 shows the case of tagged events after the $minLKL$ cut.

6.2.3 Validation in the Signal Region

The top mass value for which the event probability is minimized represents another interesting variable. Figure 6-6 shows this variable for events after the $minLKL$ cut.

The event by event most probable top mass and the dijet mass variables are of particular interest since they will be used in the reconstruction of the top mass and of the JES variable to be described in section 7. All these comparisons show good agreement between our data-driven background model and the Alpgen $b\bar{b} + 4$ light partons.

6.2.4 Effects on the Statistical Uncertainty

Using a top mass reconstruction technique based solely on the matrix element, we can vary the background fraction of our mixture of signal and background events and observe the effects on the statistical uncertainty of the top mass.

The goodness of the mass reconstruction is related to the parameters of the reconstructed versus the input top mass. The statistical uncertainty is affected by the

slope of the calibration curve. The bias in the mass reconstruction is related to the intercept of the calibration curve.

In the upper plot, Figure 6-7 shows how the slope decreases with the background fraction, while the lower plot shows how the intercept changes with the background fraction. The slope decrease indicates a decrease in the sensitivity, in other words an increase in the statistical uncertainty on the top mass. For the calibration curves studied in these plots the intercept should be 178 GeV, and it can be seen that as the background fraction increases the intercept gets further from the 178 GeV value, that is the bias increases.

The reason for the background fraction to have such a big effect on the mass reconstruction using the matrix element technique of section 4 is because the background is completely ignored in the matrix element calculation or in assessing a background event probability. In this analysis we still won't calculate a background matrix element, but we will use a background probability instead, which will be described in the next sections.

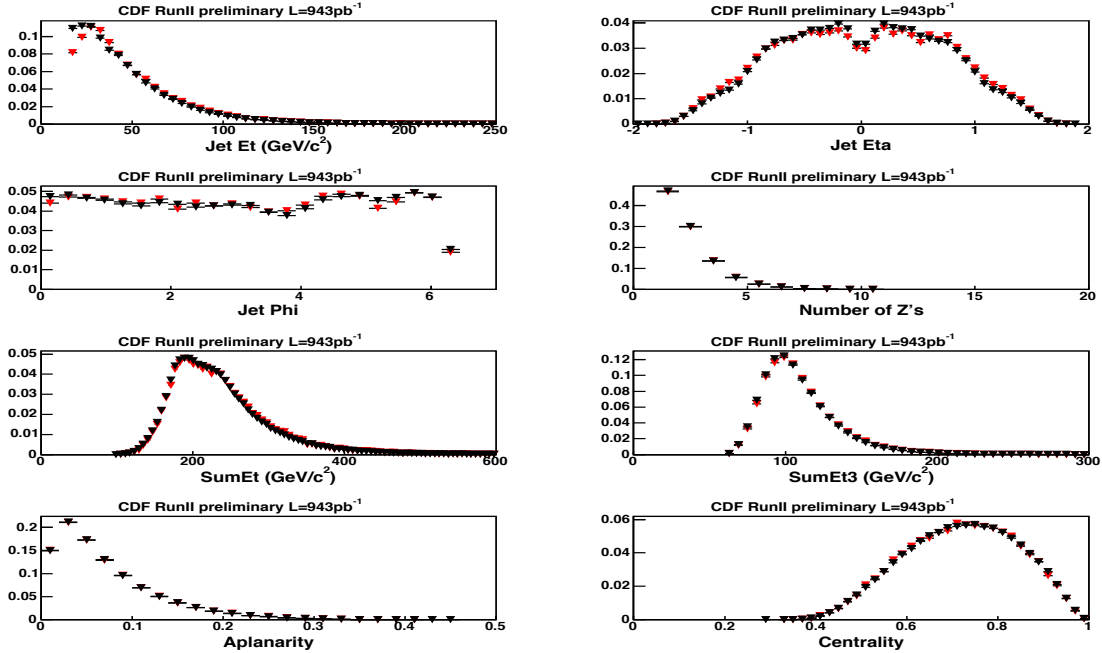


Figure 6-1. Background validation in control region 1 for single tagged events. The red points are the data points, while the black points are from the background model.

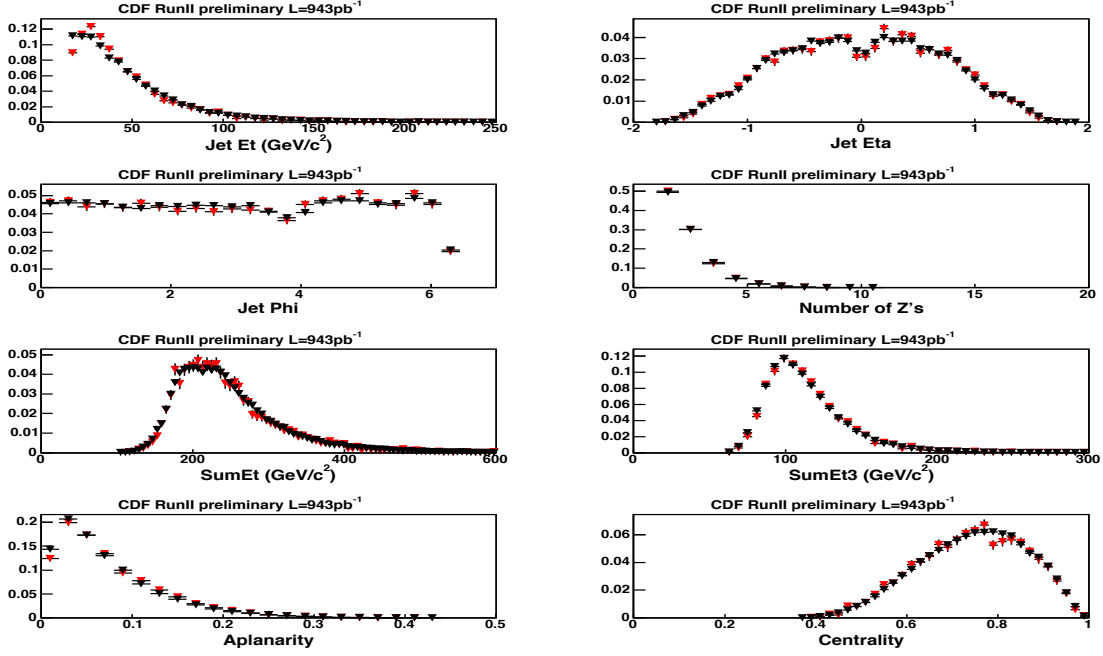


Figure 6-2. Background validation in control region 1 for double tagged events. The red points are the data points, while the black points are from the background model.

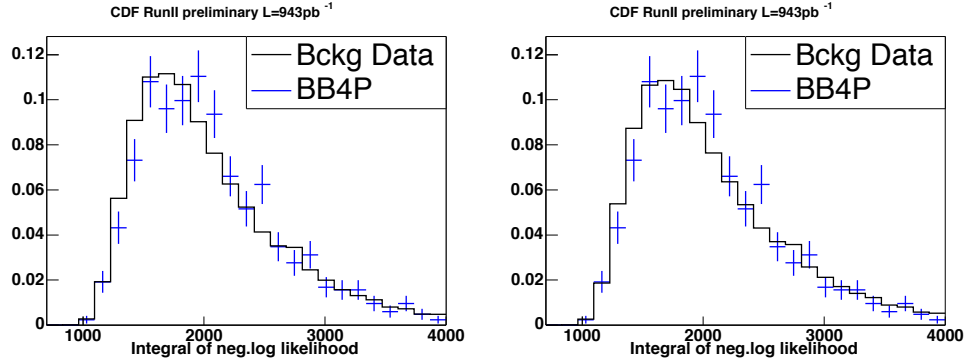


Figure 6-3. Sum of event probabilities calculated for $M_{top} = 125$ GeV up to $M_{top} = 225$ GeV in steps of 1 GeV. These are the events before the $minLKL$ cut for Alpgen $b\bar{b} + 4$ light partons in blue, and for the background model in black. The plot to the left shows the single tagged events (Kolmogorov-Smirnov probability is 1%), while the plot to the right shows the double tagged events (Kolmogorov-Smirnov probability is 13%).

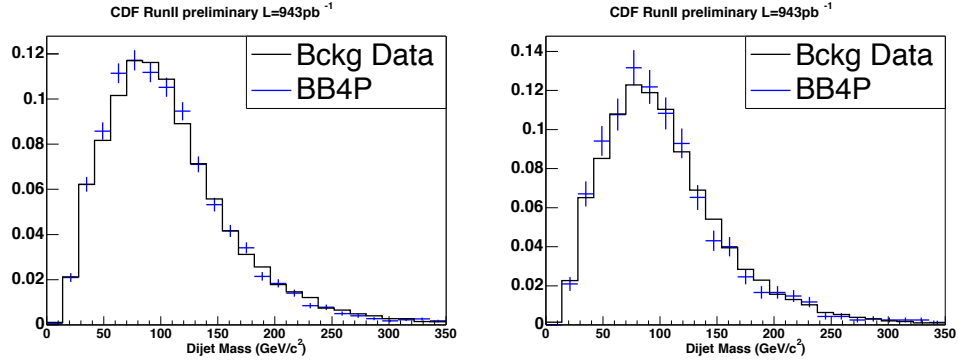


Figure 6-4. Dijet invariant mass of the untagged jets. These are the events before the $\min LKL$ cut for Alpgen $b\bar{b} + 4$ light partons in blue, and for the background model in black. The plot to the left shows the single tagged events (Kolmogorov-Smirnov probability is 25%), while the plot to the right shows the double tagged events (Kolmogorov-Smirnov probability is 43%).

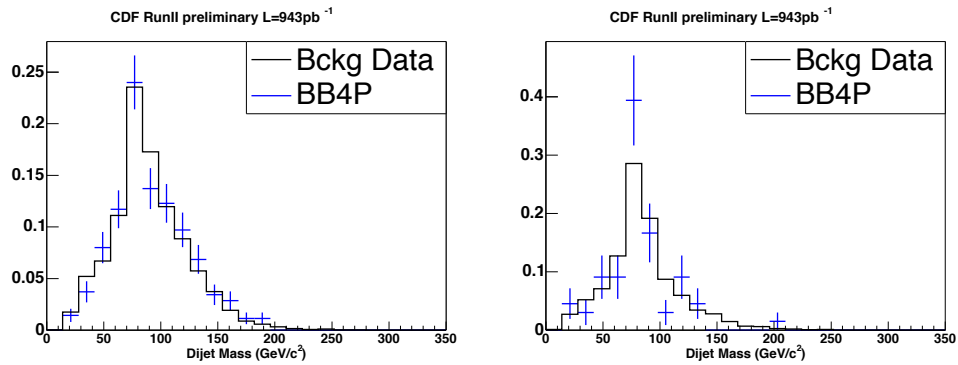


Figure 6-5. Dijet invariant mass of the untagged jets. These are the events after the $\min LKL$ cut for Alpgen $b\bar{b} + 4$ light partons in blue, and for the background model in black. The plot to the left shows the single tagged events (Kolmogorov-Smirnov probability is 90%), while the plot to the right shows the double tagged events (Kolmogorov-Smirnov probability is 70%).

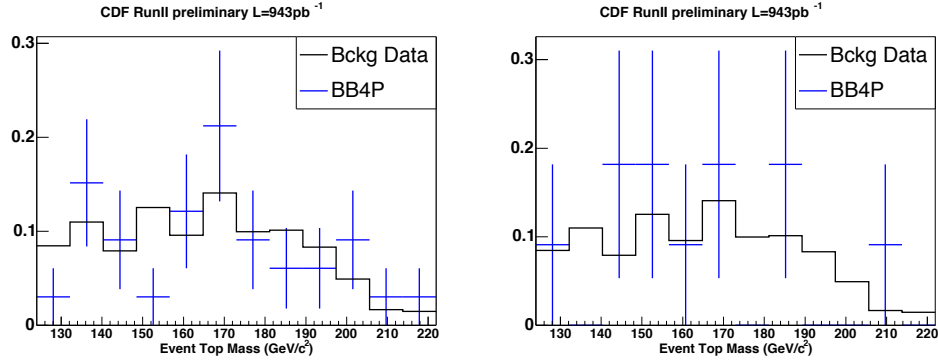


Figure 6-6. Event by event most probable top masses. These are the events after the $\min LKL$ cut for Alpgen $b\bar{b} + 4$ light partons in blue, and for the background model in red. The plot to the left shows the single tagged events, while the plot to the right shows the double tagged events.

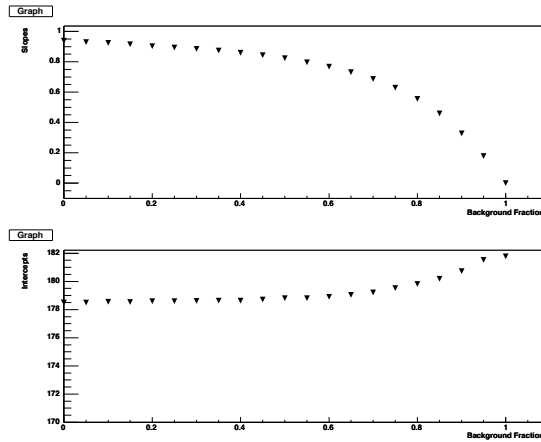


Figure 6-7. Effect of the background contamination in the top mass reconstruction using only the matrix element technique. The upper plot: slope of the calibration curve versus the background fraction. The lower plot: intercept of the calibration curve versus the background fraction. The calibration curves are built using only the matrix element reconstruction technique described in section 4.

CHAPTER 7

DESCRIPTION OF THE MASS MEASUREMENT METHOD

The biggest contribution to the uncertainty on the top quark mass is the jet energy scale uncertainty. The jet energy scale and its uncertainty is measured independently at CDF by the Jet Energy Resolution working group. It takes into account the differences between the energy scale of the jets in our Monte Carlo samples and the scale observed in the data. Its value depends on the transverse energy, pseudo-rapidity and the electromagnetic fraction of the total energy of a jet. So the jet energy uncertainty is different from jet to jet, but we will generically denote that with σ_c . The environment in which this scale and uncertainty is determined is quite different than that of the $t\bar{t}$ events, and additional corrections might be needed at this level. We define a variable, JES , called Jet Energy Scale, measured in units of σ_c . There is a correlation between the top mass and the value of JES, and that's why we plan to measure them simultaneously to avoid any double counting in the final uncertainty on the mass.

Our technique starts by modeling the data using a mixture of Monte Carlo signal and Monte Carlo background events. The events will be represented by two variables: dijet invariant mass and an event-by-event reconstructed top mass. The latter is obtained using the matrix element technique described in section 4. For signal, the shapes obtained in these two variables are parameterized as a function of top quark pole mass and JES. For background no such parameterization is needed. Hence our model will depend on the top mass and the JES. The measured values for the top quark mass and for the JES are determined using a likelihood technique described in this section.

7.1 Likelihood Definitions

The likelihood function used to reconstruct the top mass, shown in Equation 7-1, is product of 3 terms: the single tag likelihood used for single tagged events, \mathcal{L}_{1tag} , the double tag likelihood used for double tagged events, \mathcal{L}_{2tag} and the JES constraint, \mathcal{L}_{JES} , whose expression is shown in Equation 7-7.

$$\mathcal{L} = \mathcal{L}_{1tag} \cdot \mathcal{L}_{2tag} \cdot \mathcal{L}_{JES} \quad (7-1)$$

Both the single tag likelihood and the double tag likelihood are a product of four terms as shown in Equation 7-2. The top template term, \mathcal{L}_{top} , is shown in Equation 7-3. The W template term, \mathcal{L}_W , is shown in Equation 7-4. The constraint on total number of events, \mathcal{L}_{nev} , is shown in Equation 7-5. The constraint on the $t\bar{t}$ number of events, \mathcal{L}_{n_s} , is shown in Equation 7-6.

$$\mathcal{L}_{1,2tag} = \mathcal{L}_{top} \cdot \mathcal{L}_W \cdot \mathcal{L}_{nev} \cdot \mathcal{L}_{n_s} \quad (7-2)$$

Both top and W template terms have the same structure: a weighted sum of the event signal probability at a given top mass and JES and the event background probability. The fraction of $t\bar{t}$ events, $n_s/(n_s + nb)$, is the weight of the signal probability and the fraction of background events, $n_b/(n_s + nb)$, is the weight of the background probability. Together with M and JES , the parameters n_s and n_b are free in the likelihood fit.

$$\mathcal{L}_{top} = \prod_{evt=1}^{N_{events}^{tot}} \frac{n_s \cdot P_s^{top}(m_{evt}^{top}|M, JES) + n_b \cdot P_b^{top}(m_{evt}^{top})}{n_s + n_b} \quad (7-3)$$

$$\mathcal{L}_W = \prod_{evt=1}^{N_{events}^{tot} \cdot N_{combi}} \frac{n_s \cdot P_s^W(m_{evt}^W|M, JES) + n_b \cdot P_b^W(m_{evt}^W)}{n_s + n_b} \quad (7-4)$$

The sum of signal and background events, $n_s + nb$, is constrained to the total number of observed events in the data, N_{events}^{tot} , via a Poisson probability with a mean equal to N_{events}^{tot} .

$$\mathcal{L}_{nev} = \frac{(N_{events}^{tot})^{n_s+n_b} \exp(-N_{events}^{tot})}{(n_s + n_b)!} \quad (7-5)$$

The number of signal events, n_s , is constrained to the expected number of $t\bar{t}$ events, n_s^{exp} , via a Gaussian of mean equal to n_s^{exp} and width equal to $\sigma_{n_s^{exp}}$. The width of the gaussian is simply the uncertainty on the expected number of $t\bar{t}$ events.

The expected numbers of signal events, n_s^{exp} , are 13 single tagged and 14 double tagged events, corresponding to a theoretical cross-section of $6.7_{-0.9}^{+0.7}$ pb [55] and an

integrated luminosity of 943 pb^{-1} . These numbers have been determined using a $t\bar{t}$ Monte Carlo sample with a cross-section equal to the theoretical value. The value of the top mass used in the $t\bar{t}$ Monte Carlo sample just mentioned is 175 GeV and it also corresponds to the top mass value for which the theoretical cross-section has been calculated. Therefore we read the expected number of signal events from Table 5-4.

The uncertainties on the numbers of signal events $\sigma_{n_s^{exp}}$ are chosen to be the Poisson errors. This is a conservative approach since the Poisson errors are larger than the uncertainties derived based on the theoretical cross-section uncertainty.

$$\mathcal{L}_{n_s} = \exp\left(-\frac{(n_s - n_s^{exp})^2}{2\sigma_{n_s}}\right) \quad (7-6)$$

The value of JES is constrained to the a priori determination of this parameter by the CDF Jet Energy Resolution group, JES^{exp} . This constraint is a gaussian centered on JES^{exp} and width equal to 1. The unit used is σ_c which represents the uncertainty on the jet energy scale.

$$\mathcal{L}_{JES} = \exp\left(-\frac{(JES - JES^{exp})^2}{2}\right) \quad (7-7)$$

7.2 Top Templates

7.2.1 Definition of the Template

As mentioned in section 7.1, we use the matrix element to build the *top* templates. The event probability defined in section 4 is plotted as a function of the top pole mass in the range 125 GeV and 225 GeV. In negative logarithmic scale this event probability will be minimized for a certain value of top mass which we'll use to form the *top* templates. The shape of these templates depends on the input top mass and JES for $t\bar{t}$ events, but not for background events.

7.2.2 Parameterization of the Templates

We form signal templates for the mass samples described in section 5 with 7 different JES values: $-3, -2, -1, 0, 1, 2, 3$, after all our selection cuts have been applied. In total there are 84 templates for signal used for parameterization. The function used to fit them

is a normalized product of a Breit-Wigner function and an exponential. The parameters of this function depend linearly on top mass and JES. The Equation 7-8 displays the fit function and the dependence of its parameters on top mass and JES.

$$P_s^{top}(m_{evt}^{top}|M, JES) = \frac{1}{N(M, JES)} \cdot \alpha_0 \exp(-(m_{evt}^{top} - \alpha_1)\alpha_3) \times \\ \times \frac{\alpha_2}{2\pi} \cdot \frac{1}{(m_{evt}^{top} - \alpha_1)^2 + \alpha_2^2 \div 4} \quad (7-8)$$

The expression for normalization term $N(M, JES)$ from Equation 7-8 is given in Equation 7-9.

$$N(M, JES) = \sum_{k=0}^4 (p_{3k} + p_{3k+1} \cdot JES + p_{3k+2} \cdot JES^2) \cdot M^k. \quad (7-9)$$

The dependence of the parameters α_i from Equation 7-8 as a function of the top mass M and jet energy scale JES is given by Equation 7-10.

$$\alpha_i = \begin{cases} p_{15} & i = 0 \\ p_{3i+13} + p_{3i+14} \cdot M + p_{3i+15} \cdot JES & i = 1, 2, 3 \end{cases} \quad (7-10)$$

The χ^2 per degree of freedom is $1554/1384 = 1.12$ for the single tagged sample and $1469/1140 = 1.29$ for the double tagged sample. The expression for χ^2 is given in Equation 7-11.

$$\chi^2 = \frac{\sum_{m=1}^{12} \sum_{j=1}^7 \sum_{bin=1}^{Nbins} \left(\frac{h_{bin} - f_{bin}}{\sigma_{h_{bin}}} \right)^2}{(\sum_{m=1}^{12} \sum_{j=1}^7 \sum_{bin=1}^{Nbins} 1) - 25} \quad (7-11)$$

where h_{bin} is the bin content of the template histogram and f_{bin} is the value of the function from Equation 7-8 at the center of the bin. The summation in Equation 7-11 is done for all templates and for all the bins for which h_{bin} has more than 5 entries. The denominator of Equation 7-11 is the number of degrees of freedom.

For each sample, the values of the 25 parameters, p , are given in Table 7-1. The shapes of few of the signal templates as well as the parameterized curves are shown in Figure 7-1.

The background template shape is build in the same way as the signal templates using the matrix element, There is no top mass dependence. Also because we use data events to model the background there is no JES dependence. There is one subtlety regarding this shape: the procedure used to extract the background shape from data and described in section 6 doesn't remove any possible top contamination. After all the cuts are applied, this contamination is quite significant. To remove it, from the raw shape of the background template we subtract the shape corresponding to a signal template for mass equal to 170 GeV and $JES = 0$, with the appropriate coefficients reflecting the sample composition. We will assess a systematic uncertainty for the choice of signal template we subtracted.

After corrections, the shape of the background template is fitted to a normalized gaussian. For both the single tagged and the double tagged samples, we show the values of the parameters in Table 7-2.

Figure 7-2 shows the shapes of the background templates as well as the parameterized curves, for single and double tagged events. In Appendix D, all the top templates corresponding to signal events are displayed.

7.3 Dijet Mass Templates

7.3.1 Definition of the Template

The dijet mass templates are formed by considering the invariant mass of all possible pairs of untagged jets in the sample. The shape of these templates depends on the input top mass and JES for $t\bar{t}$ events, but not for background events.

7.3.2 Parameterization of the Templates

To form the signal templates we use the same 84 samples used for determining the top templates, after all our selection cuts have been applied. The function used to fit them is a normalized sum of two gaussians and a gamma integrand. The parameters of this function depend linearly on top mass and JES. The Equation 7-12 shows the fit function and the dependence of its parameters on top mass and JES.

$$\begin{aligned}
P_s^W(m_{evt}^W|M, JES) = \frac{1}{N(M, JES)} & \left[\frac{\alpha_6 \alpha_7 \exp(-\alpha_7(m_{evt}W - \alpha_8))}{\Gamma(1 + \alpha_9)} \times \right. \\
& \times (m_{evt}W - \alpha_8)^{\alpha_9} + \frac{\alpha_0}{\alpha_2 \sqrt{2\pi}} \exp\left(-\frac{(m_{evt}^{top} - \alpha_1)^2}{2\alpha_2^2}\right) + \\
& \left. + \frac{\alpha_3}{\alpha_5 \sqrt{2\pi}} \exp\left(-\frac{(m_{evt}^{top} - \alpha_4)^2}{2\alpha_5^2}\right) \right] \quad (7-12)
\end{aligned}$$

The expression for normalization term $N(M, JES)$ from Equation 7-12 is given in Equation 7-13.

$$N(M, JES) = \sum_{k=0}^1 (p_{3k} + p_{3k+1} \cdot JES + p_{3k+2} \cdot JES^2) \cdot M^k \quad (7-13)$$

The dependence of the parameters α_i from Equation 7-12 as a function of the top mass M and jet energy scale JES is given by Equation 7-14.

$$\alpha_i = p_{3i+6} + p_{3i+7} \cdot M + p_{3i+8} \cdot JES, i = 0, 9 \quad (7-14)$$

The χ^2 per degree of freedom is $3551/2636 = 1.35$ for the single tagged sample and $2972/2524 = 1.18$ for the double tagged sample. The χ^2 has the same definition as in Equation 7-11. In each sample, the values of the 36 parameters, p , are given in Table 7-3. The shapes of few of the signal templates as well as the parameterized curves are shown in Figure 7-3.

The background template shape is build in the same way as the signal templates. The top contamination is removed in the same way as in the case of the top templates (see section 7.2).

The background template is fitted to a normalized sum of two gaussians and a gamma integrand. For both the single tagged and the double tagged samples, we show the values of the parameters in Table 7-4.

Figure 7-4 shows the shapes of the background templates as well as the parameterized curves, for single and double tagged events. In Appendix E, all the dijet mass templates corresponding to signal events are displayed.

Table 7-1. Values of the parameters describing the shapes of the top templates for the $t\bar{t}$ samples.

Parameter	Values (1Tag)	Uncertainties (1Tag)	Values (2Tags)	Uncertainties (2Tags)
p_0	1.56e+03	5.69e+02	1.76e+01	4.56e+00
p_1	-3.25e+02	2.15e+02	-1.03e+01	4.65e-01
p_2	1.25e+02	9.62e+01	-3.14e+00	2.05e-01
p_3	-8.71e+00	2.85e+00	8.72e-02	1.14e-02
p_4	2.68e+00	2.26e+00	1.39e-01	3.56e-03
p_5	-1.06e+00	6.81e-01	4.12e-02	1.74e-03
p_6	-6.70e-03	1.53e-02	-3.88e-03	3.82e-05
p_7	3.44e-03	1.34e-02	-4.50e-04	2.09e-05
p_8	-1.07e-03	2.69e-03	-8.99e-05	9.69e-06
p_9	2.74e-04	9.24e-05	2.64e-05	1.48e-07
p_{10}	-5.77e-05	7.07e-05	-8.36e-07	1.09e-07
p_{11}	2.41e-05	1.40e-05	-6.36e-07	5.06e-08
p_{12}	-5.47e-07	3.33e-07	-5.41e-08	7.52e-10
p_{13}	5.81e-08	2.05e-07	4.39e-09	4.38e-10
p_{14}	-3.66e-08	5.63e-08	2.25e-09	1.91e-10
p_{15}	8.36e+02	7.17e+02	5.11e+00	5.02e+00
p_{16}	4.28e+00	1.23e+00	4.84e+00	1.06e+00
p_{17}	9.79e-01	6.97e-03	9.81e-01	6.03e-03
p_{18}	1.98e+00	5.85e-02	1.63e+00	4.72e-02
p_{19}	4.09e+00	2.29e+00	-7.95e+00	1.63e+00
p_{20}	9.29e-02	1.32e-02	1.38e-01	9.30e-03
p_{21}	2.13e-01	9.86e-02	5.01e-01	7.21e-02
p_{22}	-3.87e-02	5.50e-03	1.28e-02	6.61e-03
p_{23}	3.06e-04	3.04e-05	-4.10e-05	3.65e-05
p_{24}	-1.35e-03	2.53e-04	-2.20e-03	2.680e-04

Table 7-2. Values of the parameters describing the shapes of the top templates in the case of the background events.

Parameter	Values (1Tag)	Uncertainties (1Tag)	Values (2Tags)	Uncertainties (2Tags)
1	1.53e-02	3.09e-05	1.28e-02	9.08e-05
2	1.59e+02	7.68e-02	1.63e+02	3.73e-01
3	1.79e+03	7.17e+00	3.28e+03	6.42e+01

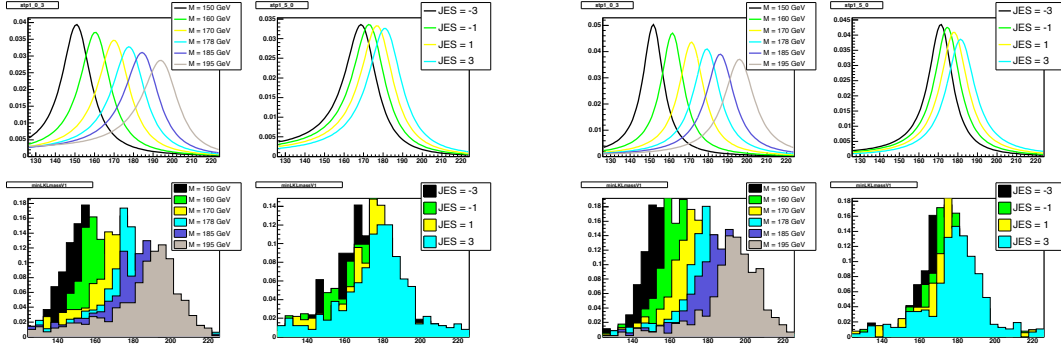


Figure 7-1. Top templates for $t\bar{t}$ events, single tags in the left plot, double tags in the right plot. The upper plots show the parameterized curves, while the bottom plots show the original histograms. The left column shows the templates variation with top mass at $JES = 0$. The right column shows their variation with JES at top mass $M_{top} = 170$ GeV.

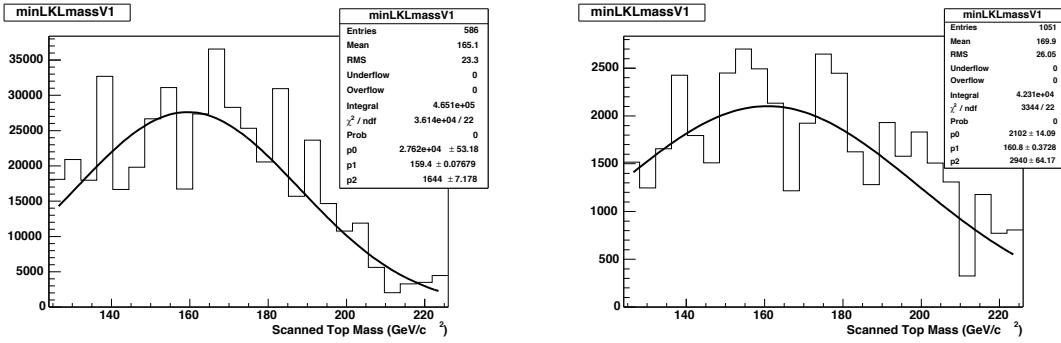


Figure 7-2. Top templates for background events. Single tags in the left plot, and double tags in the right plot.

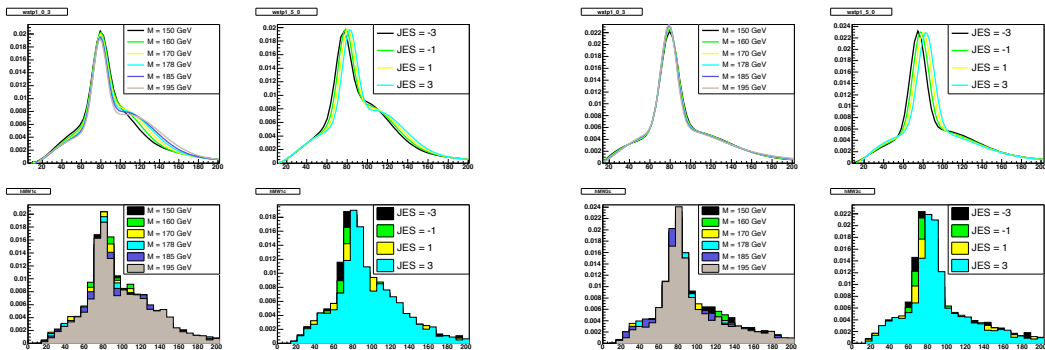


Figure 7-3. Dijet mass templates for $t\bar{t}$ events, single tags in the left plot, double tags in the right plot. The upper plots show the parameterized curves, while the bottom plots show the original histograms. The left column shows the templates variation with top mass at $JES = 0$. The right column shows their variation with JES at top mass $M_{top} = 170$ GeV.

Table 7-3. Values of the parameters describing the dijet mass templates shapes for the $t\bar{t}$ samples.

Parameter	Values (1Tag)	Uncertainties (1Tag)	Values (2Tags)	Uncertainties (2Tags)
p_0	-1.11e+00	6.84e-02	1.60e+00	8.78e-03
p_1	5.78e-01	3.45e-02	-5.84e-02	4.20e-03
p_2	-1.49e-03	1.01e-02	-1.53e-03	1.25e-03
p_3	3.44e-02	3.96e-04	-5.38e-03	4.83e-05
p_4	4.33e-05	1.68e-04	-8.99e-06	2.11e-05
p_5	6.51e-06	5.83e-05	7.51e-06	6.88e-06
p_6	2.20e-02	3.70e-02	6.51e-01	5.48e-03
p_7	6.46e-03	2.08e-04	-2.38e-03	2.86e-05
p_8	1.63e-01	9.01e-03	-2.02e-02	1.73e-03
p_9	8.20e+01	2.81e-01	8.19e+01	2.31e-01
p_{10}	-1.60e-02	1.57e-03	-1.72e-02	1.28e-03
p_{11}	1.07e+00	2.39e-02	1.37e+00	2.40e-02
p_{12}	1.04e+01	2.29e-01	1.19e+01	1.91e-01
p_{13}	-1.78e-02	1.27e-03	-2.21e-02	1.07e-03
p_{14}	2.64e-02	2.56e-02	8.09e-02	2.42e-02
p_{15}	-4.61e+00	4.58e-02	6.97e-01	6.25e-03
p_{16}	3.52e-02	2.94e-04	-3.20e-03	3.28e-05
p_{17}	1.24e-01	1.30e-02	-8.24e-03	1.82e-03
p_{18}	4.86e+01	9.69e-01	1.22e+02	1.89e+00
p_{19}	3.24e-01	5.39e-03	-1.10e-01	1.14e-02
p_{20}	2.64e+00	1.39e-01	-1.15e+00	2.82e-01
p_{21}	-2.48e+01	7.58e-01	3.90e+01	1.48e+00
p_{22}	2.85e-01	4.12e-03	-3.29e-02	8.97e-03
p_{23}	-2.53e-02	1.06e-01	1.17e+00	2.24e-01
p_{24}	3.46e+00	5.52e-02	2.68e-01	6.71e-03
p_{25}	-7.15e-03	3.05e-04	1.51e-04	3.81e-05
p_{26}	2.99e-01	1.91e-02	-3.20e-02	2.67e-03
p_{27}	8.61e-02	3.95e-04	5.75e-04	3.82e-04
p_{28}	-3.04e-04	2.38e-06	1.49e-04	2.06e-06
p_{29}	7.73e-04	1.29e-04	-5.69e-04	1.18e-04
p_{30}	-2.55e+01	6.34e-01	2.29e+01	7.68e-01
p_{31}	2.05e-01	3.58e-03	-6.22e-02	4.19e-03
p_{32}	-2.16e-01	1.18e-01	1.35e+00	1.15e-01
p_{33}	7.40e+00	3.64e-02	-1.67e+00	3.12e-02
p_{34}	-3.10e-02	1.86e-04	1.79e-02	1.82e-04
p_{35}	4.96e-02	1.39e-02	-9.61e-02	1.16e-02

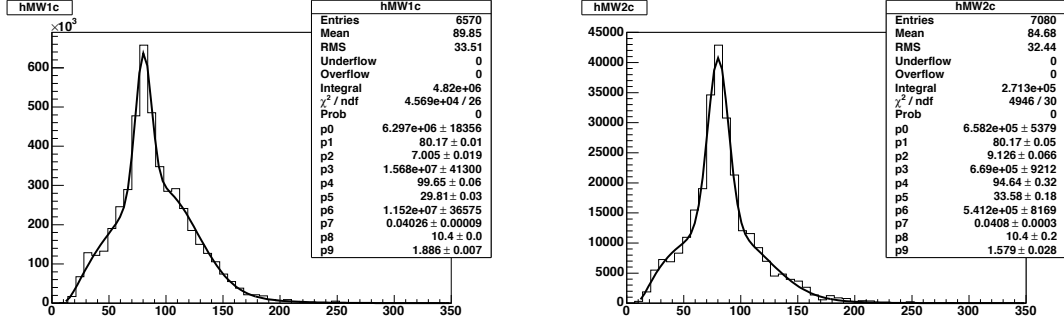


Figure 7-4. Dijet mass templates for background events. Single tags in the left plot, and double tags in the right plot.

Table 7-4. Values of the parameters describing the dijet mass templates shapes in the case of the background events.

Parameter	Values (1Tag)	Uncertainties (1Tag)	Values (2Tags)	Uncertainties (2Tags)
1	1.88e-01	9.52e-02	3.53e-01	2.39e-01
2	8.02e+01	4.29e-02	8.02e+01	1.12e-01
3	7.01e+00	1.70e-02	9.13e+00	4.41e-02
4	4.68e-01	9.52e-02	3.59e-01	2.39e-01
5	9.97e+01	4.29e-02	9.46e+01	1.12e-01
6	2.98e+01	1.70e-02	3.36e+01	4.41e-02
7	3.44e-01	9.52e-02	2.90e-01	2.39e-01
8	4.03e-02	4.29e-02	4.08e-02	1.12e-01
9	1.04e+01	1.70e-02	1.04e+01	4.41e-02
10	1.89e+00	9.52e-02	1.58e+00	2.39e-01

CHAPTER 8

MODEL VALIDATION AND SENSITIVITY STUDIES

Having defined in the previous sections the model used to describe the data, now we need to validate it and then determine the sensitivity of our method given this model. The validation of the method is in fact a self-consistency test since we will use the same Monte Carlo samples on which the modeling of the data was determined.

The statistical fluctuations of the data sample can be estimated by building many copies of the model, and by performing in each of them the same analysis we would in real data. For obvious reasons, these copies are called pseudo-experiments, and in the following subsection we describe their construction.

8.1 Pseudo-experiments Setup

Each pseudo-experiment is a mixture of signal and background events. The number of events per pseudo-experiment is drawn from a Poisson distribution of mean equal to the expected number of events. For signal events this expectation depends on the top mass according to the Standard Model. The number of background events is the difference between the observed total number of events in the data and the number of signal events.

The event-by-event top and dijet masses are randomly drawn from the shapes of the top templates histograms and dijet mass templates histograms respectively. This is what is called sampling with replacement. Therefore the pseudo-experiments thus formed will be correlated. These correlations will affect the width of any distribution filled with variables determined from the pseudo-experiments. Based on [52], we found that for any distribution the statistical uncertainty on the mean should be expressed as in Equation 8-1, the width should be expressed as in Equation 8-2 and the statistical uncertainty on the width should be expressed as in Equation 8-3.

$$\delta M = \sigma_{raw} \sqrt{\frac{1}{(N_{PE} - 1)(1 - \rho)} + \frac{\rho}{1 - \rho}} \quad (8-1)$$

$$\sigma = \sigma_{raw} \sqrt{\frac{N_{PE}}{(N_{PE} - 1)(1 - \rho)}} \quad (8-2)$$

$$\delta\sigma = \frac{\sigma}{\sqrt{2(N_{PE} - 1)}} \quad (8-3)$$

In Equations 8-1, 8-2 and 8-3, N_{PE} is the number of pseudo-experiments, σ_{raw} is the uncorrected width of a distribution, and ρ is the average correlation between any two pseudo-experiments. The value of the correlation factors depends on the size of the number of events per pseudo-experiment and on the total number of events available. Since the last two numbers depend on the top mass (see Table 5-4) then the average correlation between any two pseudo-experiments will depend on the top mass. The values for these correlation terms are given in Table 8-1.

When the JES prior is applied, the value of the JES each pseudo-experiment is constrained to is randomly selected based on a gaussian centered on the true JES of the sample and of width equal to 1.

The variables extracted from each pseudo-experiment are the values of mass, M_{out} , and JES, JES_{out} , that minimize the likelihoods defined in section 7; the statistical uncertainties on the above variables, δM_{out} and δJES_{out} and the pulls as defined by Equation 8-4.

$$Pull_{mass} = \frac{M_{out} - M_{true}}{\delta M_{out}}, \quad Pull_{JES} = \frac{JES_{out} - JES_{true}}{\delta JES_{out}} \quad (8-4)$$

The pseudo-experiment by pseudo-experiment reconstructed mass and JES form the distribution of the most probable values for mass and JES respectively. These distributions are each fitted to a gaussian. The means of these gaussians are interpreted as the reconstructed top mass and JES respectively. The width of the gaussians will represent the expected uncertainty on the top mass and on JES respectively.

8.2 Validation of the Model

This technique is used to simultaneously measure the top mass and the JES, and the likelihood to be maximized is described in section 7. Neither the top mass, nor the JES

are fixed in the likelihood. However the JES is constrained via a gaussian centered on the true JES and with a width of 1.

Figure 8-1 shows the reconstructed JES and the reconstructed top mass represented by the points, versus the true JES and true top mass represented by the grid. Ideally the points should match the grid crossings. Figure 8-2 shows reconstructed top mass versus the true top mass for a true JES of 0. Ideally, this curve should have a slope of 1, and an intercept of 175 consistent with no bias. Figure 8-3 shows reconstructed JES versus the true JES for a true top mass of 170 GeV, and again, ideally, this curve should have a slope of 1, and an intercept of 0 consistent with no bias. Figure 8-4 shows how the slope of Figure 8-2 changes with the true JES, while Figure 8-5 shows how the intercept of Figure 8-2 changes with the true JES. Figure 8-6 shows how the slope of Figure 8-3 changes with the true top mass, while Figure 8-7 shows how the intercept of Figure 8-3 changes with the true top mass. Figure 8-8 shows the mass pull means versus true top mass, while Figure 8-9 shows the mass pull widths versus true top mass. In both plots the true JES is 0. Based on these figures it results that the uncertainty on top mass has to be inflated by 10.5%. The average mass pull mean as a function of true JES is shown in Figure 8-10, while the average mass pull width as a function of true JES is shown in Figure 8-11. For a given true JES value, the average is over all the mass samples. Figure 8-12 shows the JES pull means versus true JES, while Figure 8-13 shows the JES pull widths versus true JES. In both plots the true top mass is 170 GeV. Based on these plots it results that the uncertainty on the JES has to be inflated by 5.8%. The average JES pull mean as a function of true top mass is shown in Figure 8-14, while the average JES pull width as a function of true top mass is shown in Figure 8-15. For a given true top mass value, the average is over all the JES samples.

As it can be seen in Figure 8-1, there seems to be a slight bias in the reconstruction of JES and top mass. We can extract the slope and the intercept of the dependence of the reconstructed mass on the true mass. This can be done for different JES values.

Figures 8-4 and 8-5 show the dependences on the JES of the slopes and, respectively, of the intercepts. Similarly, in the case of JES reconstruction we obtain Figures 8-6 and 8-7.

Based on the fits from Figures 8-4 and 8-5, we can express analytically how the reconstructed mass depends on the true top mass and on the true JES. This is shown in Equation 8-5. Using the fits from Figures 8-6 and 8-7, we can write similar expressions for the reconstructed JES. This is shown in Equation 8-6.

$$M_{out} = C_m + S_m \cdot (M_{true} - 175) \quad (8-5)$$

$$JES_{out} = C_j + S_j \cdot JES_{true} \quad (8-6)$$

The parameters C_m , C_j , S_m , and S_j from Equations 8-5 and 8-6 depend on the true values of top mass and jet energy scale as shown in Equation 8-7. The values of the parameters of these equations correspond to the fit parameters of Figures 8-4, 8-5, 8-6 and 8-7. They are listed in Table 8-2.

$$\begin{aligned} C_m &= a_1 + a_2 \cdot JES_{true} \\ S_m &= a_3 + a_4 \cdot JES_{true} \\ C_j &= b_1 + b_2 \cdot M_{true} \\ S_j &= b_3 + b_4 \cdot M_{true} \end{aligned} \quad (8-7)$$

Our studies indicate that the imperfect parameterization of the templates is behind the poor reconstruction of JES and top mass. The failure of the parameterization to describe the template histograms is linked to the poor statistics of the histograms. To undo these effects on the reconstruction, we can use the Equations 8-5 and 8-6 as a system of equations and solve them for the true top mass, M_{true} , and the true JES, JES_{true} . After these corrections are applied the new reconstructed values for JES and top mass are consistent with the true value within the uncertainties, as it can be seen in Figures 8-16, 8-17, 8-18, 8-19 and 8-20.

Figure 8-21 shows the residual of the top mass reconstruction using samples for which the input top mass was unknown to us, and Figure 8-22 shows the JES residuals for samples with unknown true JES. The top mass group conveners provided the samples and they were the only ones able to calculate these residuals. The plots indicate that within the uncertainties the top mass and JES reconstruction is unbiased.

8.3 Expected Statistical Uncertainty

Similar to the correction on the top mass and JES reconstructed values, we need a correction on the uncertainties on these values. By differentiating Equations 8-5 and 8-6, we obtain another system of equations to be solved for the real uncertainties. Solving Equations 8-8 and 8-9 will provide the correct uncertainties on top mass and on JES.

$$\delta M_{out} = (a_2 + a_4 \cdot (M_{true} - 175)) \cdot \delta JES_{true} + (a_3 + a_4 \cdot JES_{true}) \cdot \delta M_{true} \quad (8-8)$$

$$\delta JES_{out} = (b_2 + b_4 \cdot JES_{true}) \cdot \delta M_{true} + (b_3 + b_4 \cdot M_{true}) \cdot \delta JES_{true} \quad (8-9)$$

Figure 8-23 shows the expected uncertainty on top mass versus input top mass, using an input JES of 0. Figure 8-24 shows the expected uncertainty on the JES versus input JES for an input top mass of 170 GeV. The expected uncertainties shown in Figure 8-23 contain both the pure statistical uncertainty on the top mass and the uncertainty due to JES. This uncertainty depends on the top mass because the expected number of $t\bar{t}$ events depends on the top mass.

In order to disentangle the statistical contribution from the JES component of this uncertainty, we performed a different reconstruction of the top mass by fixing the JES to the true value in the 2D fit. Following this reconstruction, the uncertainty on the top mass is purely of statistical nature. For a top mass of 170 GeV the expected statistical uncertainty is 2.5 GeV, whereas the combined statistical and JES-systematic uncertainty, as per Figure 8-23, is 3.2 GeV. That means the systematic uncertainty due to JES on top mass is 2.0 GeV. This systematic uncertainty shows an improvement of 10% over the 1D JES systematic uncertainty on top mass of 2.2 GeV.

On average, the uncertainty on the JES is $0.9 \sigma_c$, and this also shows an improvement of 10% over the uncertainty provided by the JER group. The uncertainty on JES is consistent with the weighted average of the in situ measurement of JES provided by the W templates and the measurement provided by the JER group. The uncertainty in the latter case is 1. In order to estimate the uncertainty on the JES provided by the in situ measurement using the W templates, we performed a different 2D reconstruction with the JES constraint removed. The uncertainty on the JES in this case is 1.47, and it is consistent with the weighted averaged result.

Table 8-1. Value of the average correlation factor between any two pseudo-experiments. The dependence on the value of the top mass is due to the $t\bar{t}$ cross-section dependence on top mass.

M_{top} (GeV/ c^2)	ρ
150	0.073
155	0.068
160	0.065
165	0.064
170	0.062
175	0.061
178	0.055
180	0.059
185	0.059
190	0.062
195	0.059
200	0.061

Table 8-2. Values of the parameters describing the linear dependence on the true JES and on the true M_{top} , of the intercept and slope of the M_{top} calibration curve and of the JES calibration curve respectively.

Parameter	Value	Uncertainty
a_1	175.0	0.1
a_2	-0.09	0.05
a_3	0.975	0.008
a_4	0.016	0.004
b_1	0.6	0.3
b_2	-0.003	0.002
b_3	1.35	0.15
b_4	-0.0021	0.0008

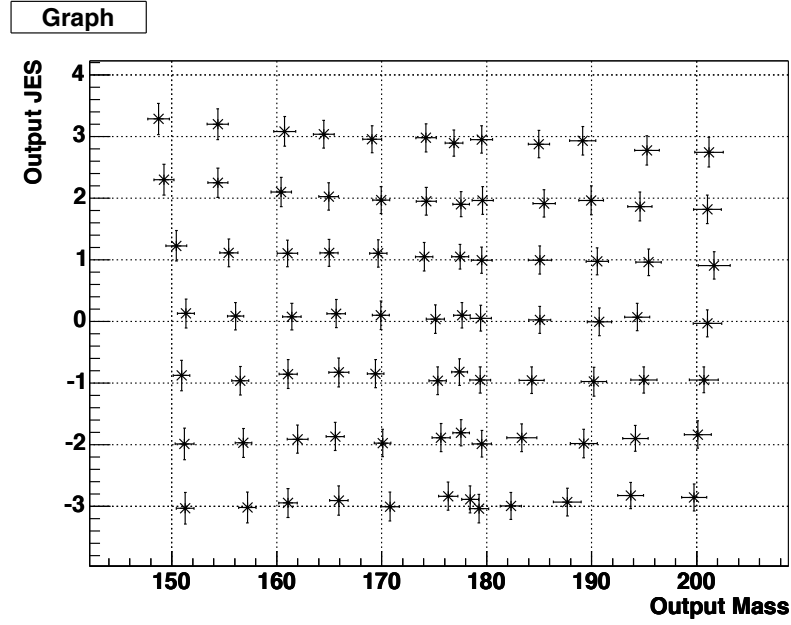


Figure 8-1. JES versus Top Mass plane. The points represent the reconstructed JES and mass.

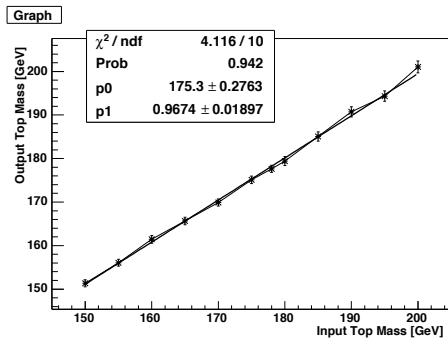


Figure 8-2. Reconstructed top mass versus input top mass, for input JES equal to 0.

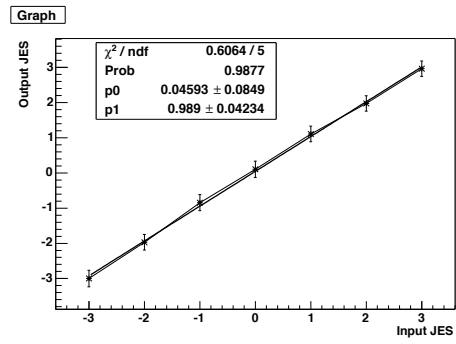


Figure 8-3. Reconstructed JES versus input JES, for input top mass equal to 170 GeV.

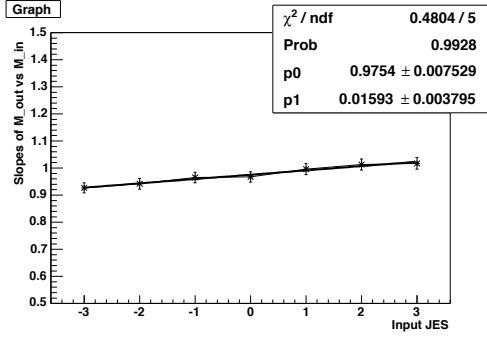


Figure 8-4. Slope of the mass calibration curve versus input JES.

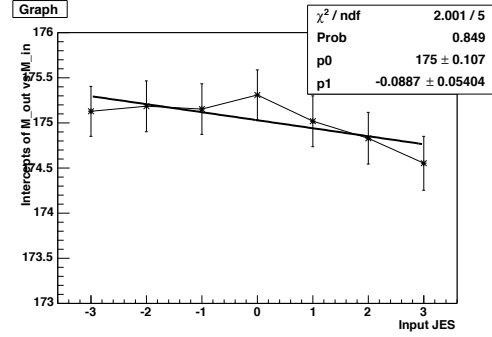


Figure 8-5. Constant of the mass calibration curve versus input JES.

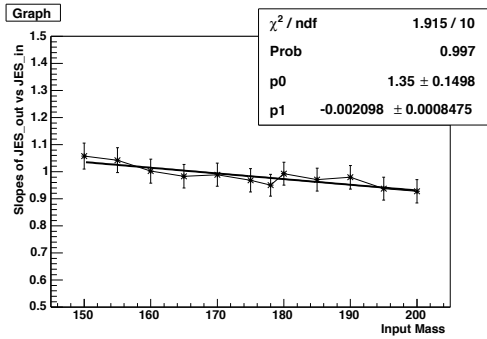


Figure 8-6. Slope of the JES calibration curve versus input JES.

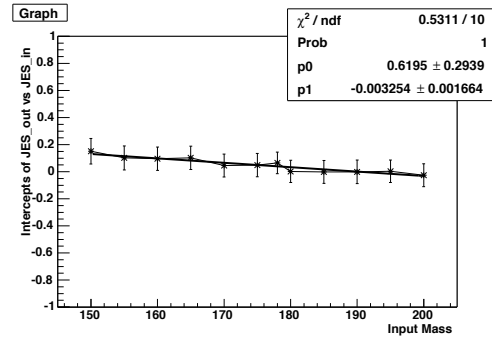


Figure 8-7. Constant of the JES calibration curve versus input JES.

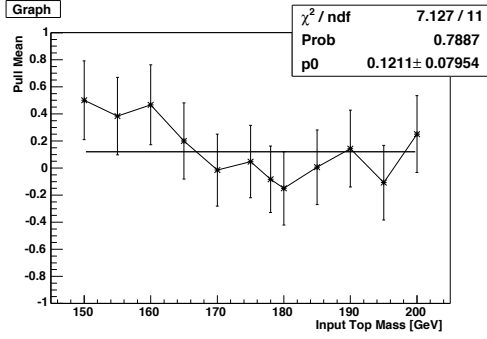


Figure 8-8. Mass pull means versus input top mass, for input JES equal to 0.

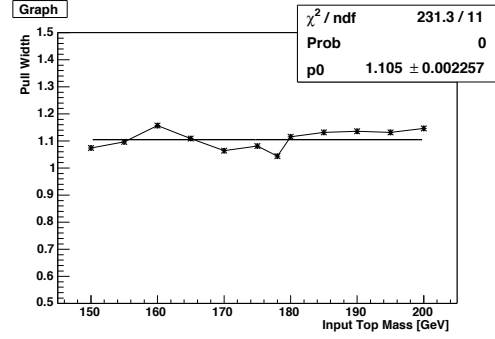


Figure 8-9. Mass pull widths versus input top mass, for input JES equal to 0.

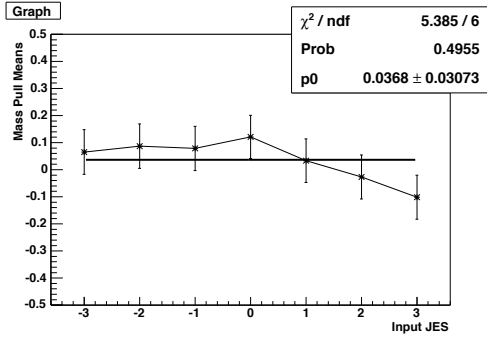


Figure 8-10. Average of mass pull means versus input JES.

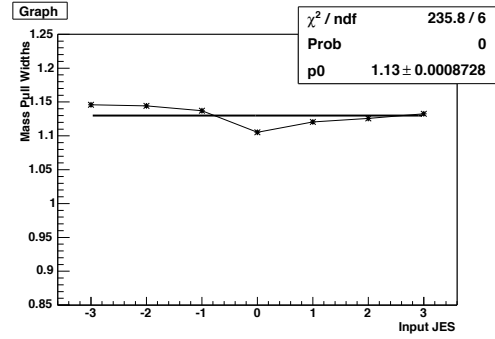


Figure 8-11. Average of mass pull widths versus input JES.

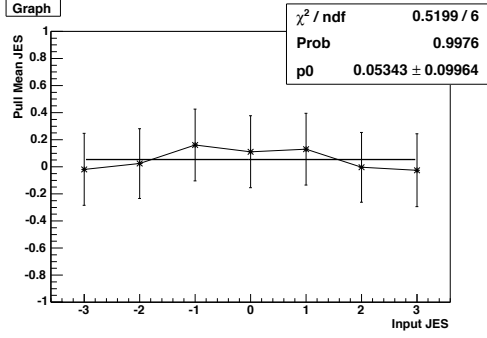


Figure 8-12. JES pull means versus input top mass, for input top mass equal to 170 GeV.

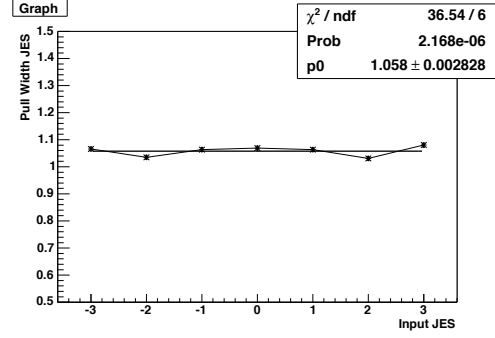


Figure 8-13. JES pull widths versus input top mass, for input top mass equal to 170 GeV.

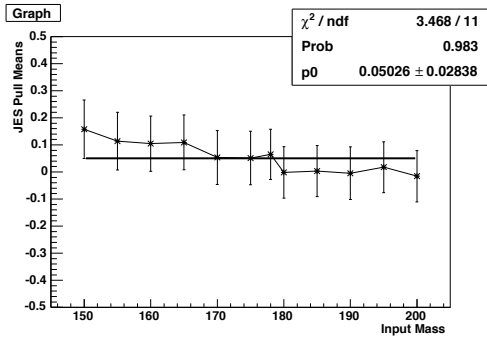


Figure 8-14. Average of JES pull means versus input top mass.

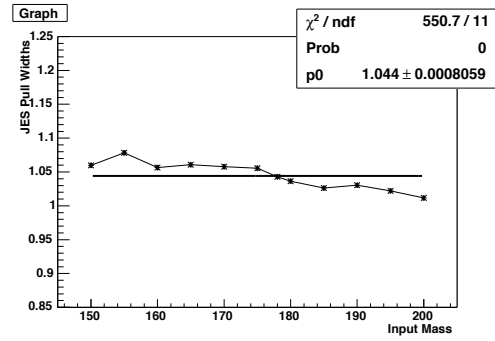


Figure 8-15. Average of JES pull widths versus input top mass.

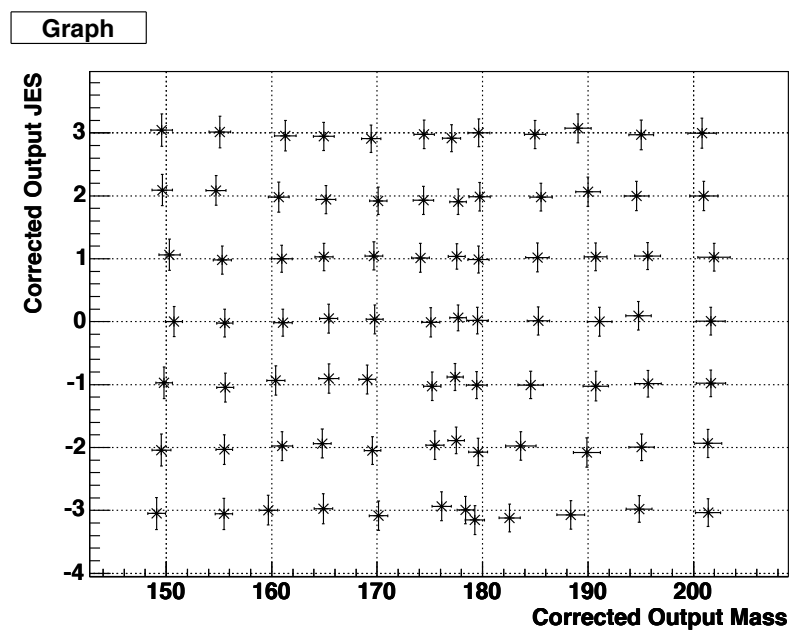


Figure 8-16. JES versus Top Mass plane. The points represent the reconstructed JES and mass after the 2D correction.

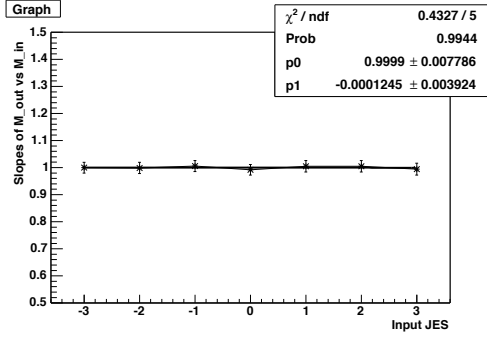


Figure 8-17. Slope of the M_{top} calibration curve versus true JES after the 2D correction.

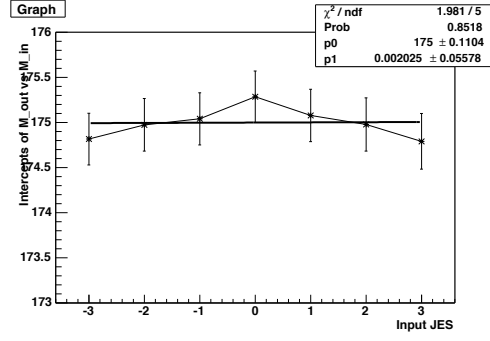


Figure 8-18. Intercept of the M_{top} calibration curve versus true JES after the 2D correction.

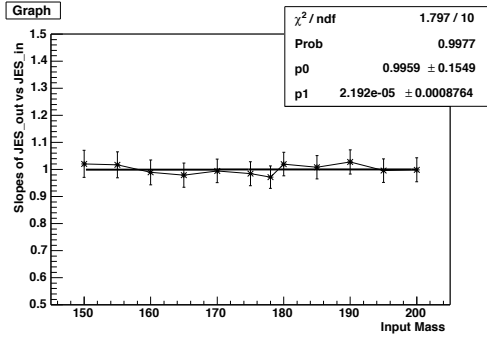


Figure 8-19. Slope of the JES calibration curve versus true M_{top} after the 2D correction.

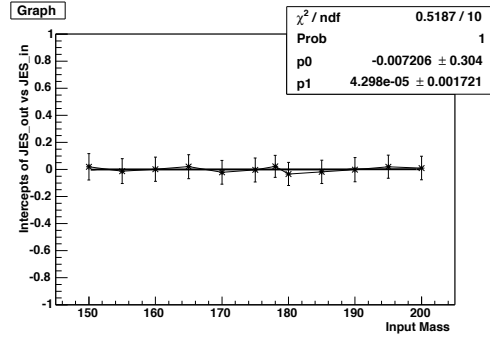


Figure 8-20. Intercept of the JES calibration curve versus true M_{top} after the 2D correction.

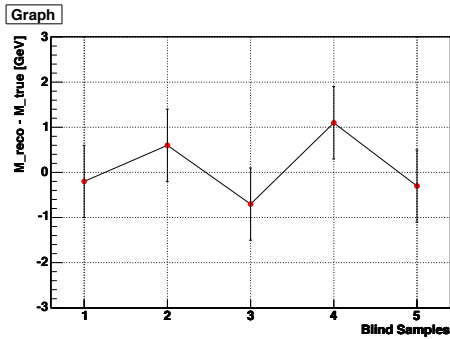


Figure 8-21. Difference between the reconstructed mass and the true mass for blind mass samples.

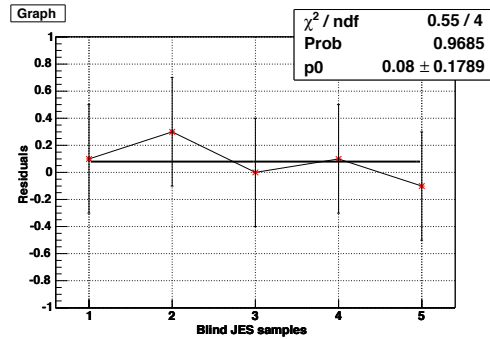


Figure 8-22. Difference between the reconstructed and the true JES for blind JES samples.

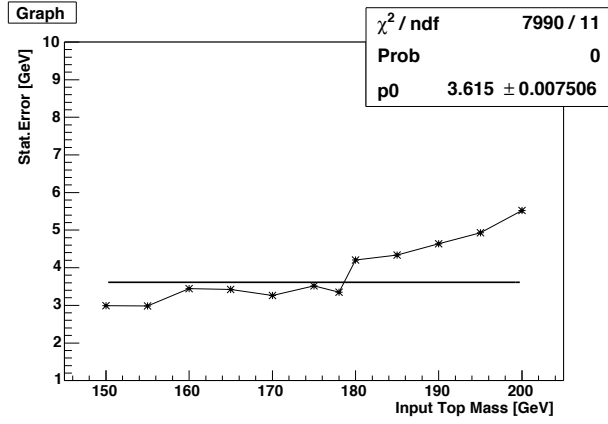


Figure 8-23. Expected uncertainty on top mass versus input top mass, for input JES equal to 0. This uncertainty includes the pure statistical uncertainty and the systematic uncertainty due to JES.

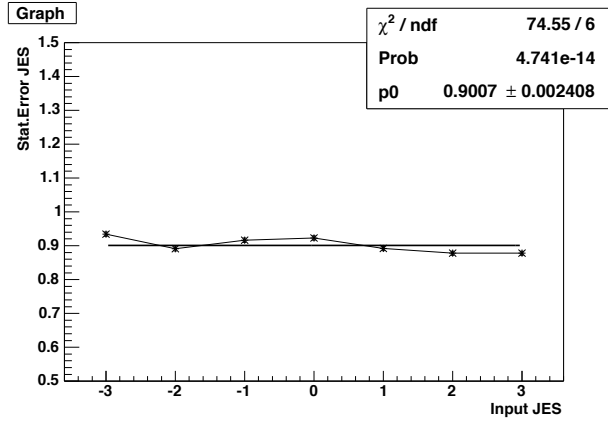


Figure 8-24. Expected uncertainty on JES versus input JES, for input top mass equal to 170GeV.

CHAPTER 9

SYSTEMATIC UNCERTAINTIES

Our model for $t\bar{t}$ events is exclusively based on the simulation which doesn't describe the physics of such events very precisely. The major sources of uncertainties appear from our understanding of jet fragmentation, our modeling of the radiation off the initial or final partons, and our understanding of the proton and antiproton internal structure. Apart from these generic uncertainties, we also address other issues specific to the present method such as the shape of the background top templates following the $t\bar{t}$ decontamination, the correlation between the dijet masses and the top mass determined for each event, and the level of imprecision in the determination of the bi-dimensional correction of the reconstructed top mass and JES .

9.1 Jet Fragmentation

The default Monte Carlo package used to determine our top and dijet templates is Herwig which is known to differ from the Pythia package in terms of modeling the jet fragmentation. We decided that reconstructing the top mass in a sample generated with Pythia, but using our Herwig based machinery, will result in an offset with respect to the Herwig sample that would represent the uncertainty on the jet fragmentation model. Having the true top mass equal to 178 GeV, we reconstruct a top mass of 177.6 GeV using Herwig as generator and 178.6 GeV using Pythia. Therefore the uncertainty due to modeling of the jet fragmentation amounts to 1 GeV.

9.2 Initial State Radiation

The amount of radiation off the initial partons is regulated in Pythia by certain parameters. Using the default set of values, a sample with the true top mass of 178 GeV is reconstructed at 178.6 GeV. Increasing the amount of radiation off the initial partons results in a reconstructed top mass of 178.9 GeV, while decreasing the amount of such radiation results in a top mass of 178.6 GeV. Taking the maximum change in top mass, we quote 0.3 GeV as the uncertainty due to initial state radiation modeling.

9.3 Final State Radiation

Similar arguments to those used for initial state radiation uncertainties will help us determine the uncertainty due to modeling of the radiation off the final partons. The reconstructed top mass in the default case is again 178.6 GeV for a true top mass of 178 GeV. Increasing the amount of radiation results in a top mass of 177.7 GeV, while decreasing it we get 177.4 GeV. The maximum change in top mass is 1.2 GeV and this will be the uncertainty on the modeling of the final state radiation.

9.4 Proton and Antiproton PDFs

In our default simulation, the internal structures of the proton and antiproton is given by the CTEQ5L set of functions, and a true top mass of 178 GeV is reconstructed at 178.6 GeV. Changing the set of functions to those given by CTEQ6M, the reconstructed top mass is 178.7 GeV. Within the CTEQ6M set, the top group has identified 20 independent parameters whose variations will be representative for the uncertainty on the modeling of such structure functions. Adding in quadrature all the 20 offsets observed on top mass reconstruction due to these variations, we get 0.4 GeV.

Also, it is known that the value of Λ_{QCD} has a direct effect on the shape of the structure functions. In order to estimate this effect, we chose yet another set of PDFs given by MRST, and reconstructed the top mass for $\Lambda_{QCD} = 228$ GeV to get a top mass of 177.7 GeV, and for $\Lambda_{QCD} = 300$ GeV to get a top mass of 178.7 GeV. Therefore the uncertainty due to the value of Λ_{QCD} is 0.3 GeV.

Adding the two contributions in quadrature, we quote that the total uncertainty due to the choice of structure functions of proton and antiproton is 0.5 GeV.

9.5 Background Shape

Since the background shape has been obtained initially from data, we had to remove the $t\bar{t}$ contamination. To remove the top contamination, we assumed a top mass of 170 GeV, and now we have to estimate effect of this assumption. We have modify our assumption on the top mass of the top contamination by 10 GeV, that is we got two

background shapes one corrected for top of 160 GeV and the other corrected for top of 180 GeV. The change in the value of the reconstructed top mass is 0.9 GeV.

9.6 Background Statistics

Another effect we address here is the effect of the limited statistics of the sample used to generate the background sample. To estimate this effect is enough to vary the parameters describing the background shapes. First we notice that the dijet mass template histograms for background are quite smooth, so only the event top mass template histograms will be modified.

One has to remember that the background model is based on about 2600 pretag data events passing the kinematical selection. Then using the mistag matrix we artificially increased the size of this sample by calling “event” any distinct tagged configuration. Therefore any of the original 2600 events will generate a number of these artificial “events”. This number will be referred to as the multiplicity of the real event.

In order to find the uncertainties on the background parameters, we need to fluctuate the content of the template histograms. Given the fact that entries of these histograms are not real events, but artificial “events”, we have to somehow fluctuate the number of real events from each bin. The procedure is described below:

- assume the event multiplicity the same for all real events and equal to the average multiplicity for the whole sample: 735 for single tags and 41 for double tags
- before the $t\bar{t}$ contamination removal and based on the constants above, we scale down the template histograms
- fluctuate the content of the scaled histograms using the Poisson probability
- after the Poisson fluctuation, scale back up the histograms, remove the $t\bar{t}$ contamination and fit with a gaussian to obtain the new template function
- repeat the above steps 10,000 times, and histogram the parameters of the new templates
- extract the uncertainties on the background parameters from these last histograms

Figure 9-1 shows the event multiplicity single tagged events on the left, and for double tagged events on the right. Figure 9-2 shows the histograms of the three parameters describing the gaussian fit for the single tagged events, while Figure 9-3 shows the equivalent plots in the case of the double tagged events. The uncertainties on the background parameters as determined following the histogram fluctuation are shown in Table 9-1. Varying the background parameters within these uncertainties results in a shift in top mass of 0.4 GeV.

9.7 Correlation Between Top Mass and Dijet Mass

We investigate here the effect of the correlation between the event top mass and dijet mass has on the top mass pull widths and pull means. Our pseudo-experiments were formed by randomly selecting the event top masses from the top mass templates and by randomly selecting the dijet masses from the dijet mass templates. As a consequence the correlation between two masses is reduced to zero. Figure 9-4 shows on the left the top mass pull mean in the default case when the above correlation was reduced to zero, while on the right is shown the situation with full correlation. Figure 9-5 shows the equivalent comparison involving the top mass pull widths.

On average over different top mass samples, the pull mean is consistent within the uncertainties between the two scenarios. However, the pull widths appear higher when the correlation between the event top mass and the dijet mass is zero. We conclude that there is no need for a systematic uncertainty, and we keep the default pull width as the correcting factor on the statistical error on the top mass since it represents the more conservative approach.

9.8 2D Calibration

We have varied the parameters of Equations 8-5 and 8-6 within their uncertainties as listed in Table 8-2. We then re-calibrated the reconstructed values for the top mass. The change in top mass is 0.2 GeV.

9.9 B-jet Energy Scale

We study the effect of the uncertainty on the modeling of heavy flavor jets due to the uncertainty in the semi-leptonic branching ratio, the modeling of the heavy flavor fragmentation and due to the color connection effects.

To determine this we reconstruct the top mass in a Monte Carlo sample where the b -quarks could be geometrically matched to a jet, and the energy of such jets was modified by 1%. As it turns out in [53], 0.6% of the jet energy uncertainty on the b -jets is coming from the effects listed above. Therefore the final shift on the top mass following our 1% shift in b -jets energies needs to be scaled down by a factor of 0.6. The systematic uncertainty on the top mass due to the b -jet energy scale is 0.4 GeV.

9.10 Residual Jet Energy Scale

From the bi-dimensional fit for top mass and JES, we extract an uncertainty on the top mass that includes a statistical component as well as a systematic uncertainty due to the uncertainty on the JES parameter. However, the JES parameter is defined as the sum of six independent effects, and therefore the systematic uncertainty on the top mass included in the 2D fit is only a leading order uncertainty due to our limited understanding of the jet energy scale. Second order components of this uncertainty arise from the limited understanding of the six individual contributions to JES. Additional details on this source of uncertainty can be found in [54].

For this we have to study the effect on the top mass reconstruction from each of these six sources: level 1, 4, 5, 6, 7 and 8. A Monte Carlo sample has been used where the energies of the jets have been shifted up or down by the uncertainty at each level separately, so a total of 12 samples have been obtained. We reconstruct the top mass in each of them, without applying any constrain on the value of JES. In Table 9-2 we present the average shift on the top mass at each level, and their sum in quadrature. We conclude from this that the residual jet energy uncertainty on top mass is 0.7 GeV.

9.11 Summary of the Systematic Uncertainties

The total systematic uncertainty on the top mass combining all the effects listed above is 2.1 GeV. Table 9-3 summarizes all sources of systematic uncertainties with their individual contribution as well as the combined effect.

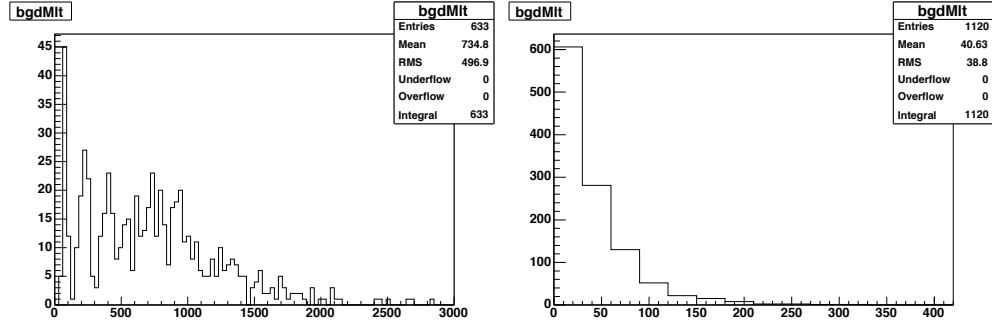


Figure 9-1. Event multiplicity for background events. On the left is shown the plot for single tagged events, while on the right the plot for double tagged events is shown.

Table 9-1. Uncertainties on the parameters of the top mass templates for background.

Parameter	1 tag	2 tags
Constant	10.2e-04	7.0e-04
Mean	2.59	3.35
Sigma	272.1	711.9

Table 9-2. Residual jet energy scale uncertainty on the top mass.

Level	Uncertainty (GeV/c ²)
L1	0.2
L4	0.1
L5	0.5
L6	0.0
L7	0.5
L8	0.1
Total <i>JES</i> Residual	0.7

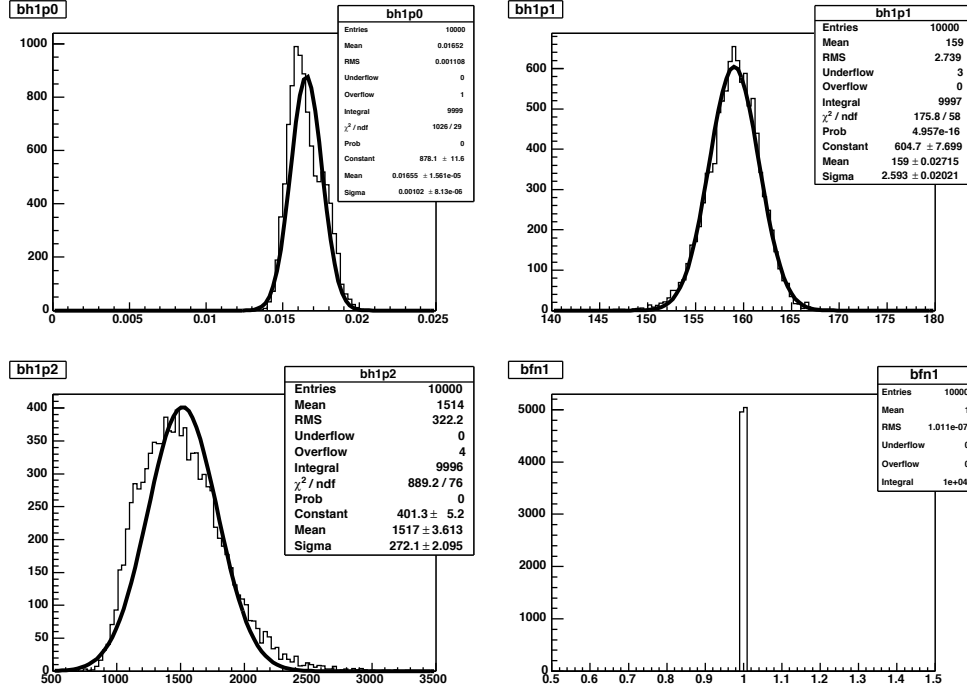


Figure 9-2. Histograms of the parameters of the gaussian fit of the background event top mass template for single tagged events. Upper left plot shows the constant of the gaussian, upper right shows the mean of the gaussian, lower left shows the width of the gaussian, and lower right plot shows the normalization of the gaussian.

Table 9-3. Summary of the systematic sources of uncertainty on the top mass.

Source	Uncertainty (GeV/c ²)
Initial State Radiation	0.3
Final State Radiation	1.2
PDF choice	0.5
Pythia vs. Herwig	1.0
Method Calibration	0.2
Background Shape	0.9
Background Statistics	0.4
Sample Composition	0.1
Heavy Flavor JES	0.4
Residual JES	0.7
Total	2.1

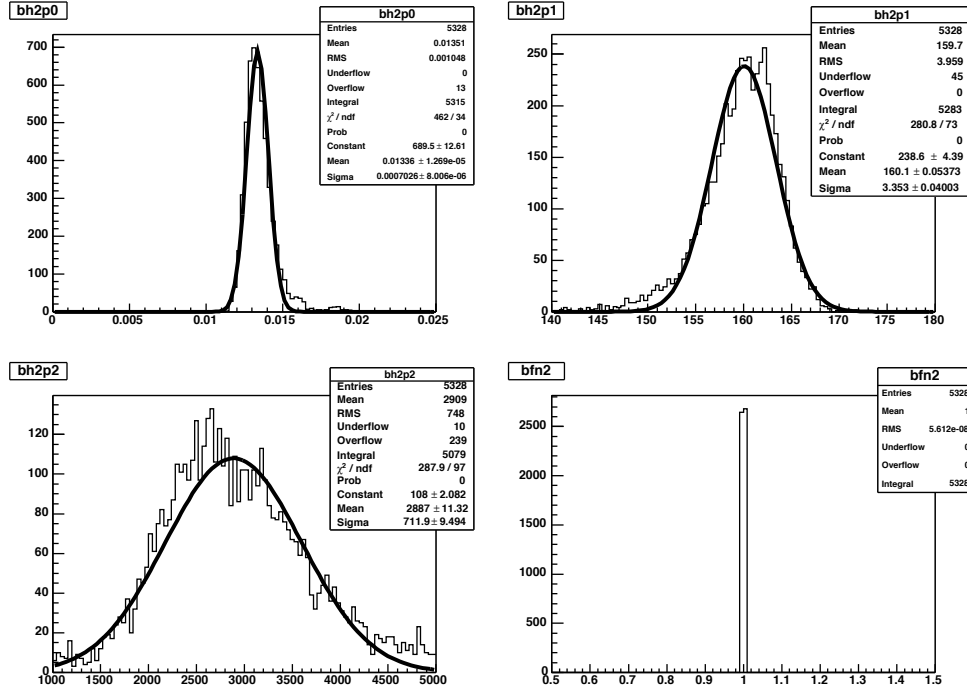


Figure 9-3. Histograms of the parameters of the gaussian fit of the background event top mass template for double tagged events. Upper left plot shows the constant of the gaussian, upper right shows the mean of the gaussian, lower left shows the width of the gaussian, and lower right plot shows the normalization of the gaussian.

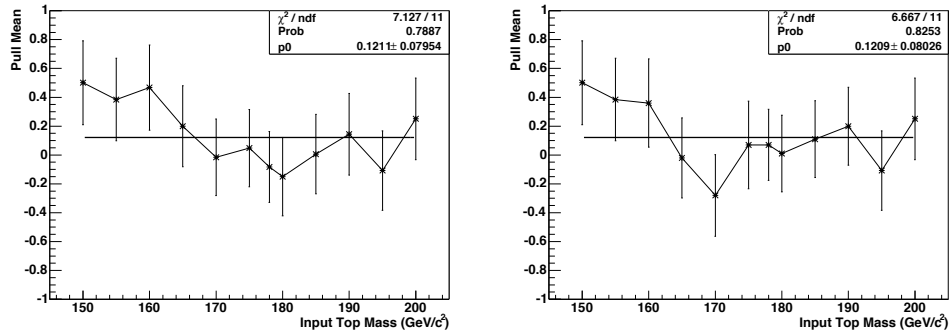


Figure 9-4. Top mass pull mean as a function of top mass for different treatment of the correlation between the event top mass and the dijet mass. On the left is the default case when the correlation is zero, while on the right is shown the situation with the full correlation.

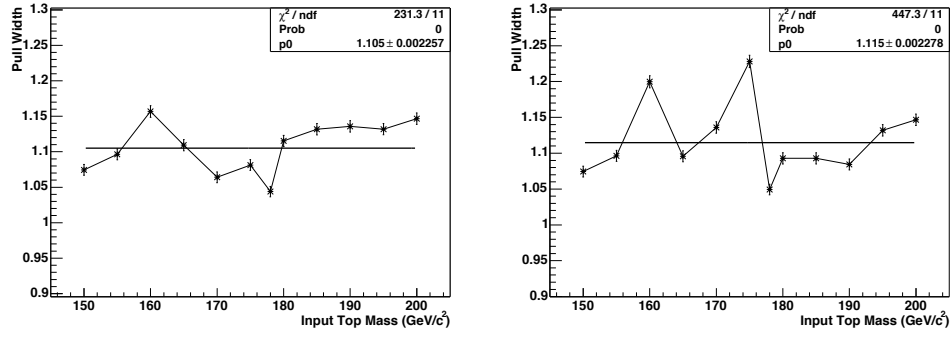


Figure 9-5. Top mass pull width as a function of top mass for different treatment of the correlation between the event top mass and the dijet mass. On the left is the default case when the correlation is zero, while on the right is shown the situation with the full correlation.

CHAPTER 10 CONCLUSION

We have applied the method described in the previous chapters to the data sample corresponding to 943 pb^{-1} . In this sample, there are 48 single tagged and 24 double tagged events after all the cuts have been applied.

In the second column of Table 10-1, we show in the total number of events and the expected number of signal events used as input in the 2D likelihood of Equation 7-1. Note that in Equation 7-1 we need the uncertainty on the expected number of signal events and this is also shown in Table 10-1. The numbers of background events are shown as well, but they are not used as input values in the likelihood. In the third column we show the number of events as they result from the minimization of the 2D likelihood.

Following the minimization of the 2D likelihood, we measured a top mass of $171.1 \pm 3.7 \text{ GeV}$, and a JES of $0.5 \pm 0.9 \sigma_c$. The value of the jet energy scale (JES) is therefore consistent with the previous determination of JES at CDF.

The quoted uncertainty on the top mass represents the combination of the statistical uncertainty with the systematic uncertainty due to JES uncertainty. In order to obtain only the statistical uncertainty on the top mass, the minimization of the 2D likelihood is modified such that the JES parameter is fixed to $0.5 \sigma_c$ (the result from 2D fit). Following this procedure the statistical uncertainty on the top mass is 2.8 GeV . Therefore the systematic uncertainty due to JES is 2.4 GeV .

Figure 10-1 shows the distributions of event by event reconstructed top masses as the black points for data and as the orange histogram for the combination of signal and background templates that best fitted the data. The blue histogram represents only the background template. The sample with single tagged events is shown in the left plot, while the double tagged events are shown in the right plot.

The 2D likelihood is shown in Figure 10-2. The central point corresponds to the minimum of the likelihood, while the contours represent the 1-sigma, 2-sigma, and 3-sigma levels, respectively.

Using a $t\bar{t}$ Monte Carlo sample with a top mass equal to 170 GeV and the number of signal and background events as resulted from the data fit, we formed pseudo-experiments and determined the expected uncertainty on the top mass due to statistical effects and JES. About 41% of the pseudo-experiments had such combined uncertainty on the top mass lower than the measured value of 3.7 GeV. This can be seen in Figure 10-3, where the histogram shows the results of the pseudo-experiments and the blue line represents the measured uncertainty. In conclusion, the measured combined statistical and JES uncertainties on the top mass agrees with the expectation.

The total uncertainty on the top mass in this analysis is 4.3 GeV. The previous best mass measurement in this channel had an equivalent total uncertainty of 5.3 GeV [56] which is 23% more. The source for this improvement is the uncertainty due to jet energy scale (JES) on the top mass. In this analysis this uncertainty amounts to 2.4 GeV compared to 4.5 GeV in the previous best result which is 88% more. Some of this gain in precision is lost due to the somewhat higher systematic uncertainties from other sources and due to a slightly worse statistical uncertainty in this analysis compared with the previous best mass result in this channel. A more careful estimation of the other sources of systematic uncertainties on the top mass as well as a more efficient $t\bar{t}$ event selection will help further reduce the total uncertainty on the top mass.

Compared to mass measurements in other $t\bar{t}$ decay channels, the mass measurement from this analysis ranked third in the top mass world average [57] with a 11% weight. The two better measurements were performed in the lepton+jets channel as it can be seen in Figure 10-4. This measurement promotes the all hadronic channel as the second best channel for the top quark mass analyses in Run II at the Tevatron.

In conclusion, it is for the first time in the $t\bar{t}$ all hadronic channel to have a simultaneous measurement of the top mass and of the jet energy scale. It is also the first mass measurement in this channel that involved the use of the $t\bar{t}$ matrix element either in the event selection or in the mass measurement itself. All of the above were successfully mixed together resulting in the best top mass measurement in the all hadronic channel.

Table 10-1. Number of events for the $t\bar{t}$ expectation and for the observed total for a luminosity of 943 pb^{-1} passing all the cuts. The input values for signal have the uncertainties next to them in parenthesis. The background expectation being the difference between total and signal is also shown. For the output values, the numbers in the parenthesis are the uncertainties.

Number of Events	Input	Reconstructed
Total Observed(1tag)	48	47.8
Expected Signal (1tag)	13 ± 3.6	13.2 ± 3.7
Background (1tag)	35	34.6 ± 7.2
Total Observed(2tags)	24	23.3
Expected Signal (2tags)	14 ± 3.7	14.1 ± 3.4
Background (2tags)	10	9.2 ± 4.3

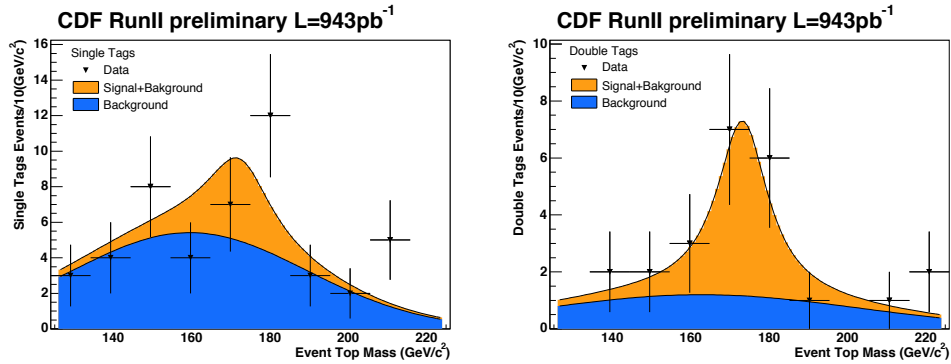


Figure 10-1. Event reconstructed top mass for data (black points), signal+background (orange) and only background events (blue). Single tagged sample is on the left, while the double tagged sample is on the right.

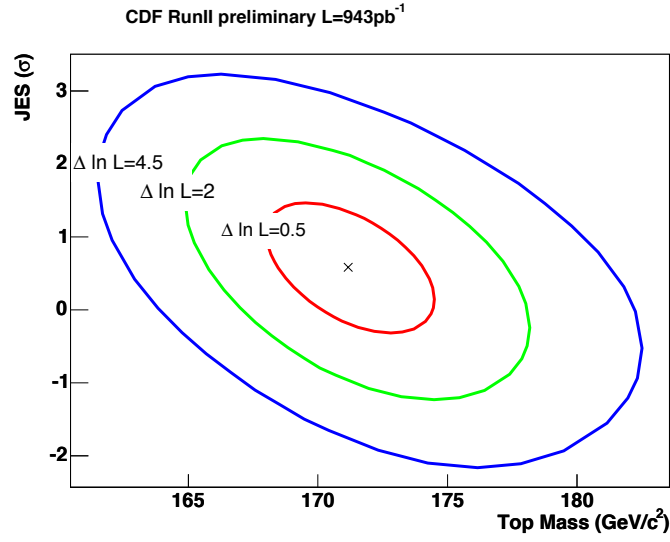


Figure 10-2. Contours for 1-sigma (red), the 2-sigma (green) and the 3-sigma (blue) levels of the mass and JES reconstruction in the data.

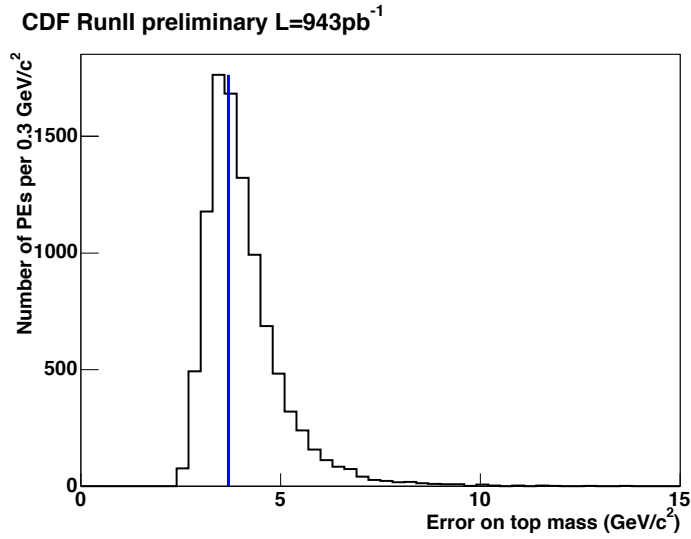


Figure 10-3. Histogram shows the expected statistical uncertainty from Monte Carlo using pseudo-experiments, while the line shows the measured one. About 41% of all pseudo-experiments have a lower uncertainty.

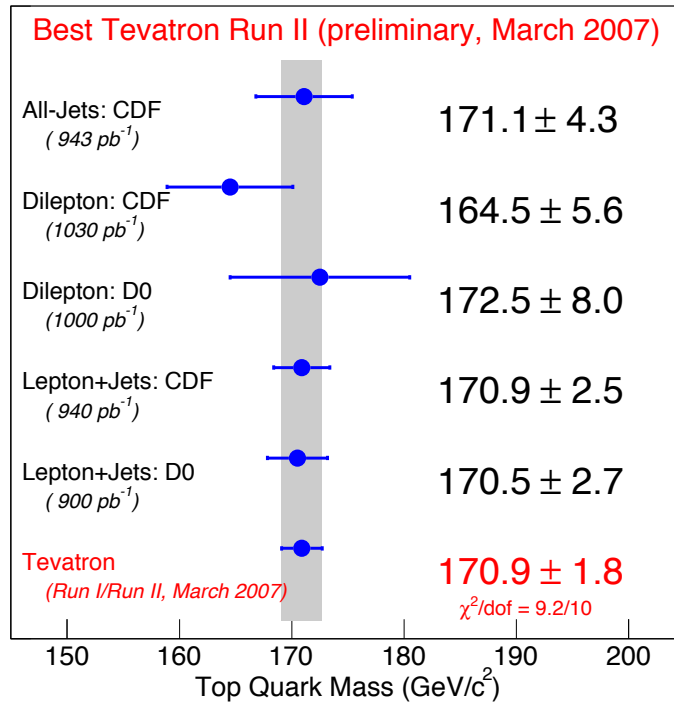


Figure 10-4. Most precise results from each channel from the D0 and CDF experiment at Fermilab by March 2007. Taking correlated uncertainties properly into account the resulting preliminary world average mass of the top quark is 170.9 ± 1.1 (stat) ± 1.5 (syst) GeV/c² which corresponds to a total uncertainty of 1.8 GeV/c². The top quark mass is now known with a precision of 1.1%.

APPENDIX A

PARTON DISTRIBUTION FUNCTION OF THE PROTON

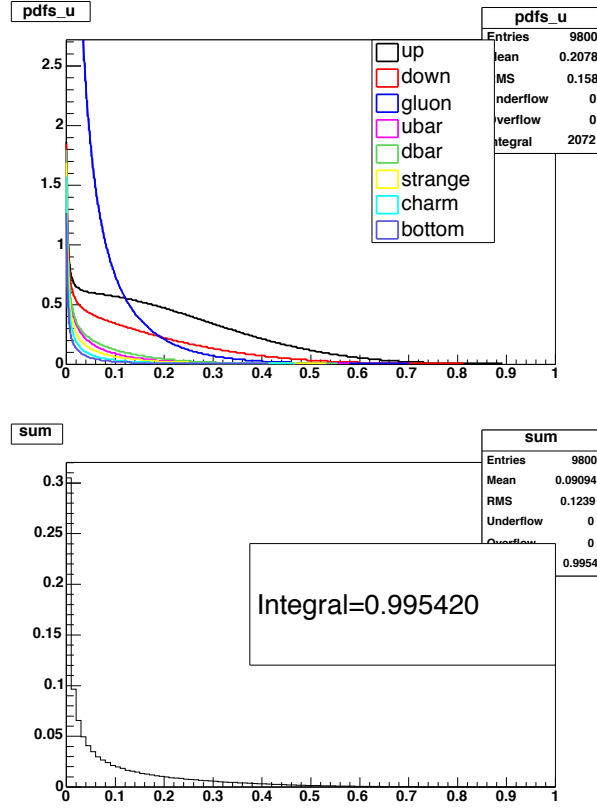


Figure A-1. Upper plot shows the PDF shapes used in the matrix element calculation of section 4.3. Bottom plot shows a cross check of the normalization of these PDFs.

APPENDIX B TRANSVERSE MOMENTUM OF THE $t\bar{t}$ SYSTEM

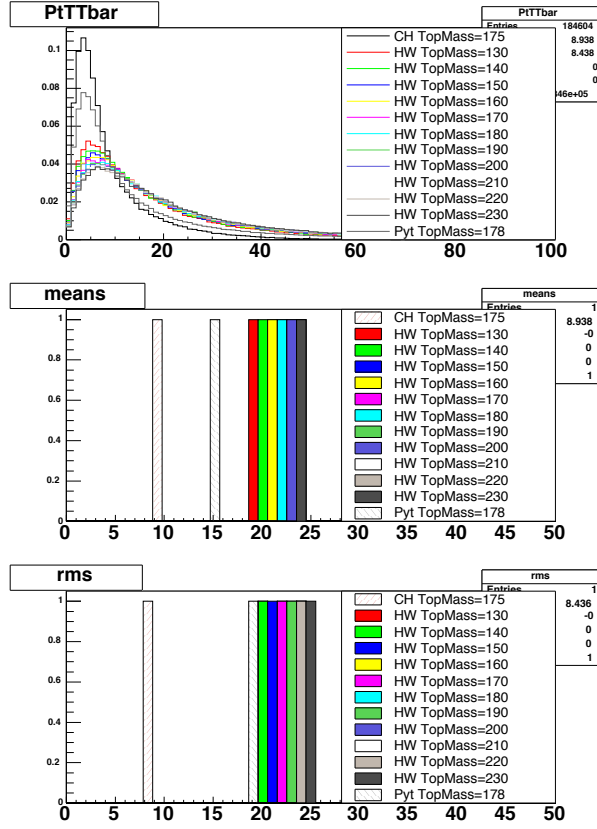


Figure B-1. Transverse momentum of the $t\bar{t}$ system for different generators and for different top masses. Upper plot: shapes of the transverse momentum of the $t\bar{t}$ system for different generators (CompHep, Pythia and Herwig) and for different top masses. Middle plot: the Means of the distributions in the upper plot. Lower plot: the RMS of the distributions in the upper plot.

APPENDIX C TRANSFER FUNCTIONS

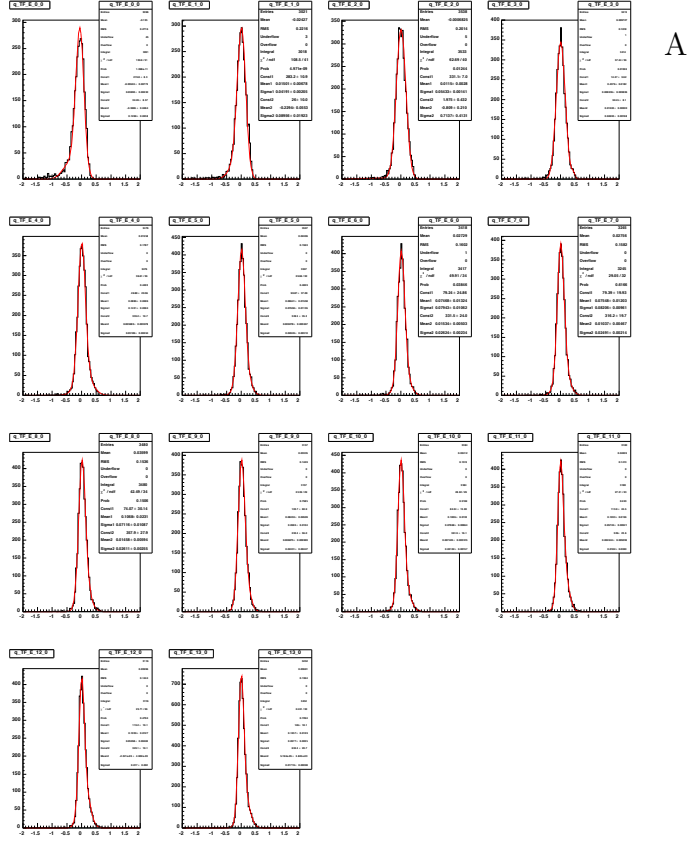
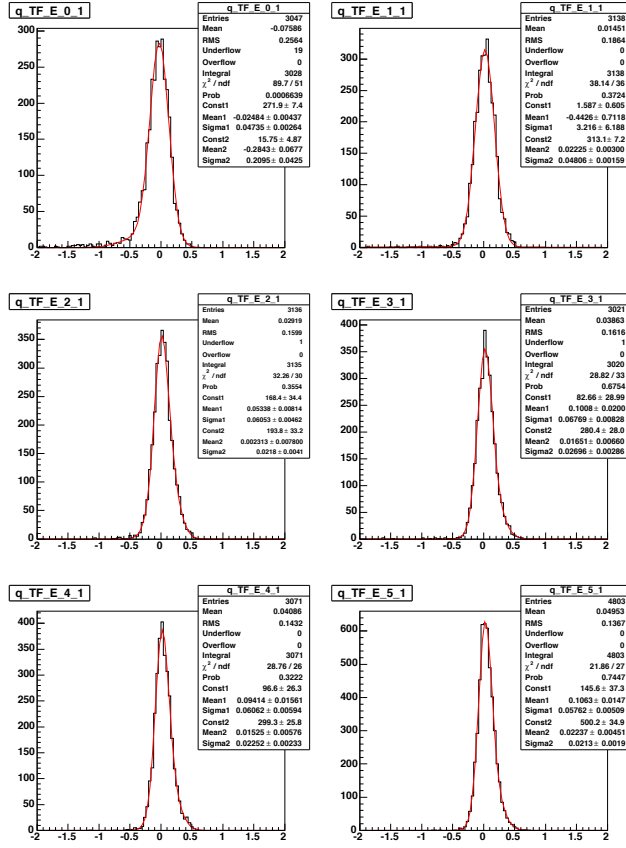


Figure C-1. Transfer functions for the W -boson decay partons. A) For partons with the value for pseudo-rapidity $|\eta| < 0.7$. B) For partons with pseudo-rapidity $0.7 \leq |\eta| < 1.3$. C) For partons with pseudo-rapidity $1.3 \leq |\eta| \leq 2$.



B

Figure C-1. Continued

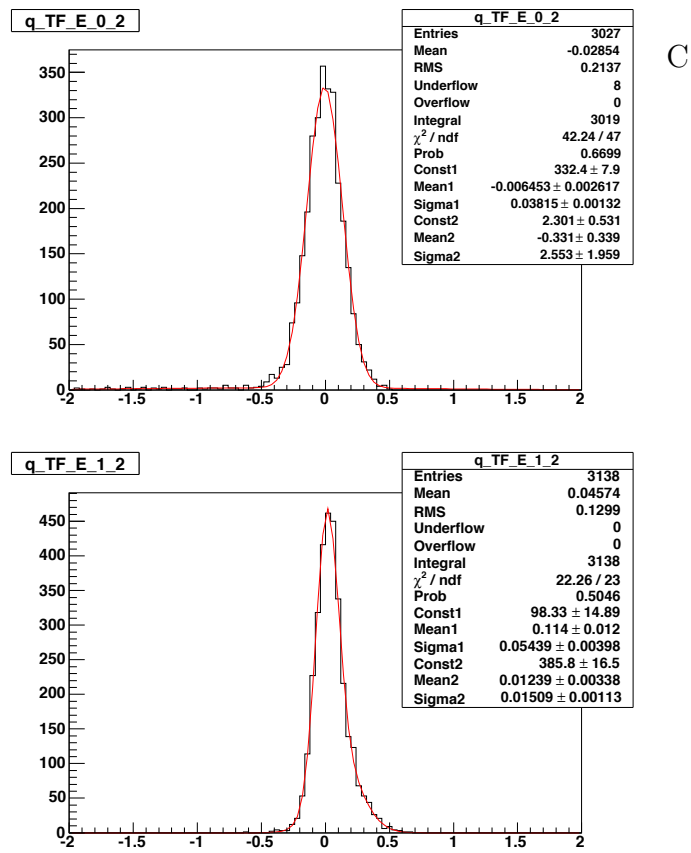


Figure C-1. Continued

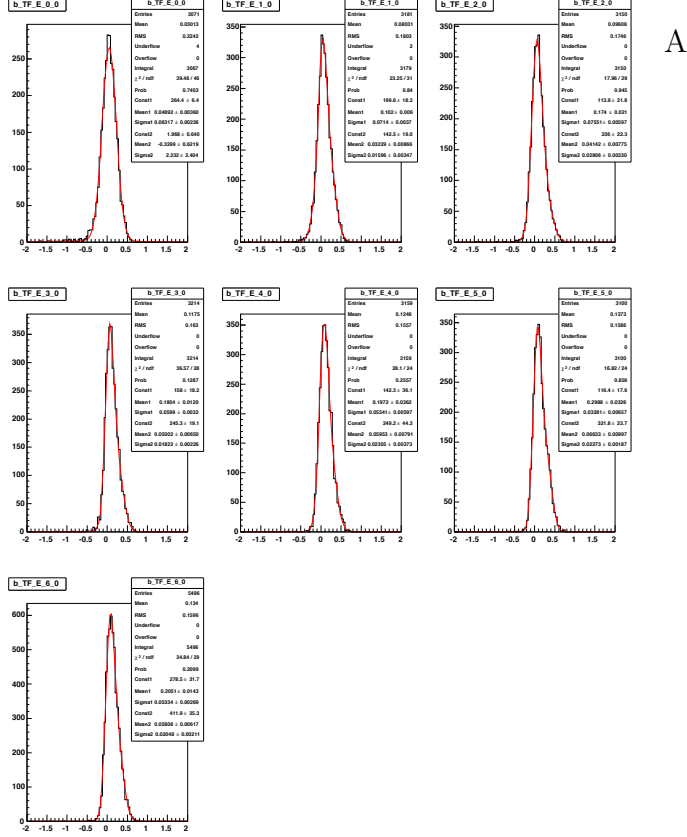


Figure C-2. Transfer functions for the b -quark partons. A) For partons with the value for pseudo-rapidity $|\eta| < 0.7$. B) For partons with pseudo-rapidity $0.7 \leq |\eta| < 1.3$. C) For partons with pseudo-rapidity $1.3 \leq |\eta| \leq 2$.

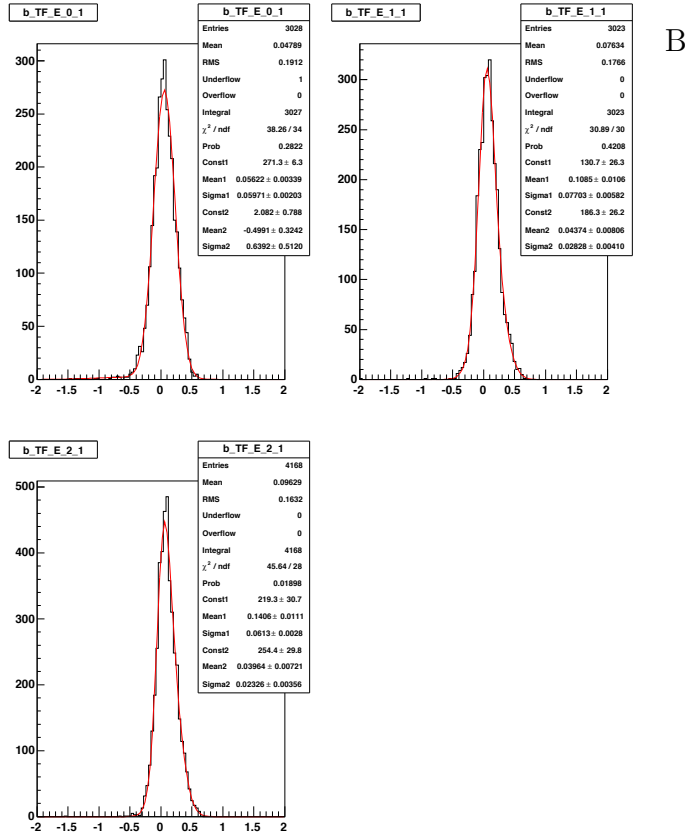


Figure C-2. Continued

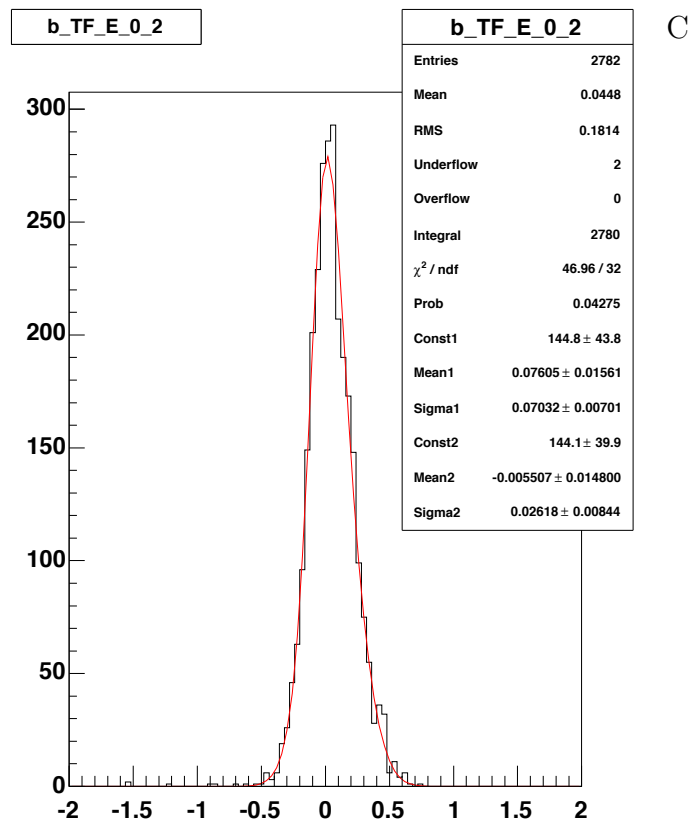
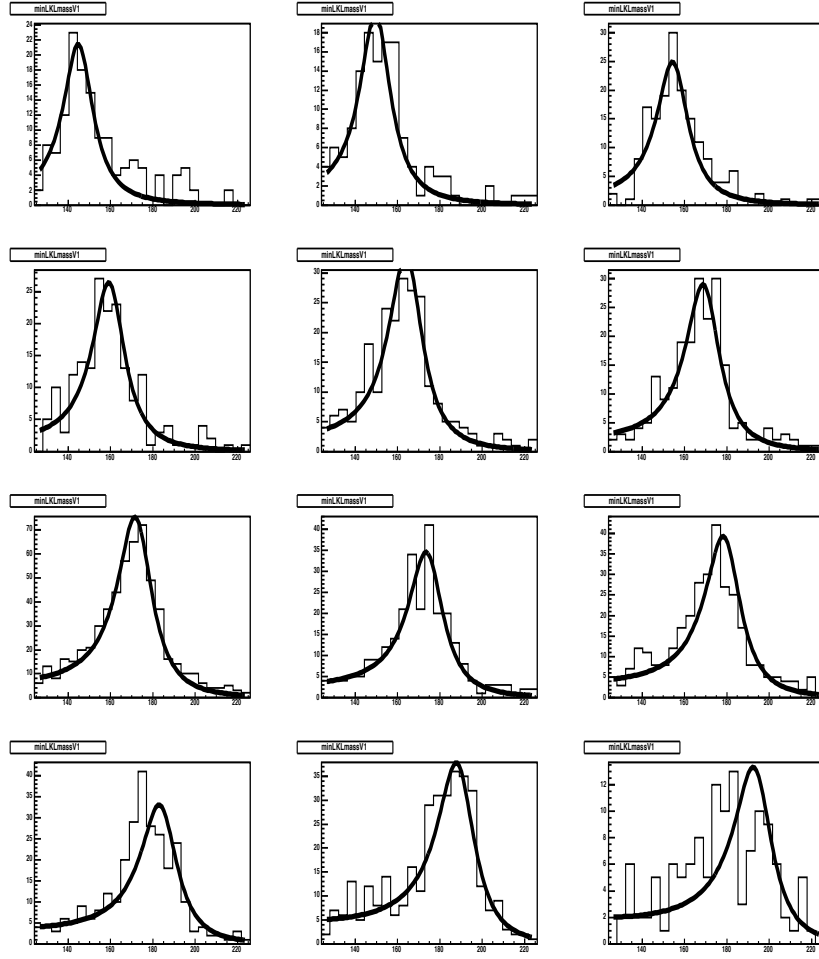


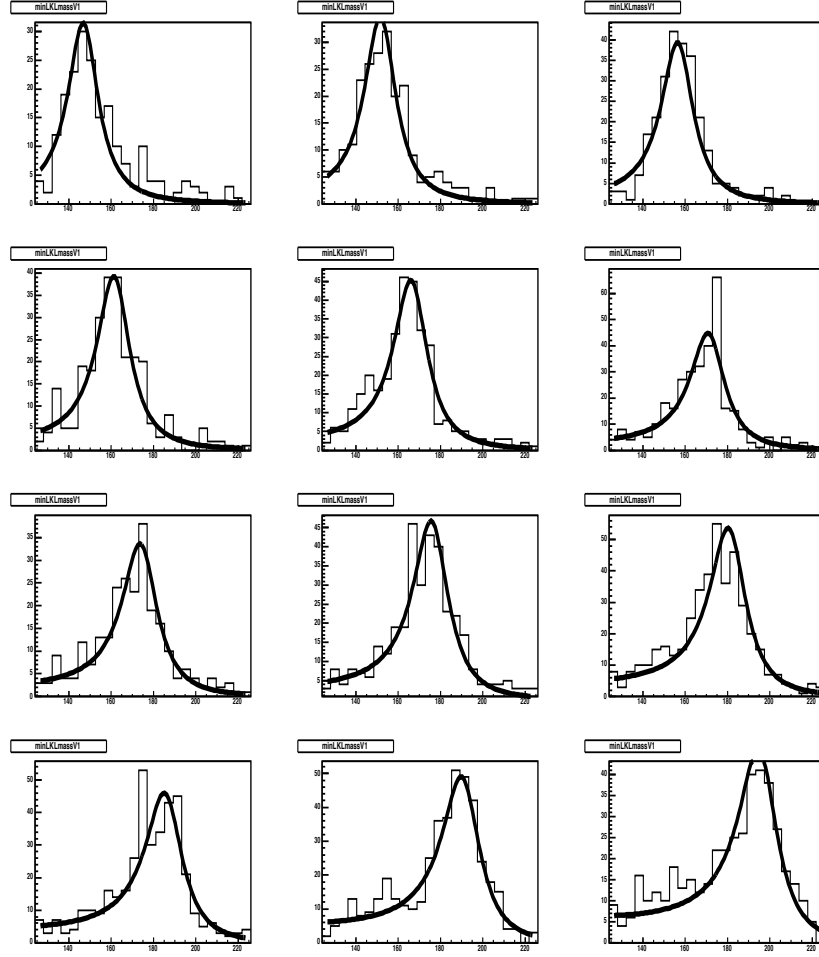
Figure C-2. Continued

APPENDIX D SIGNAL TOP TEMPLATES



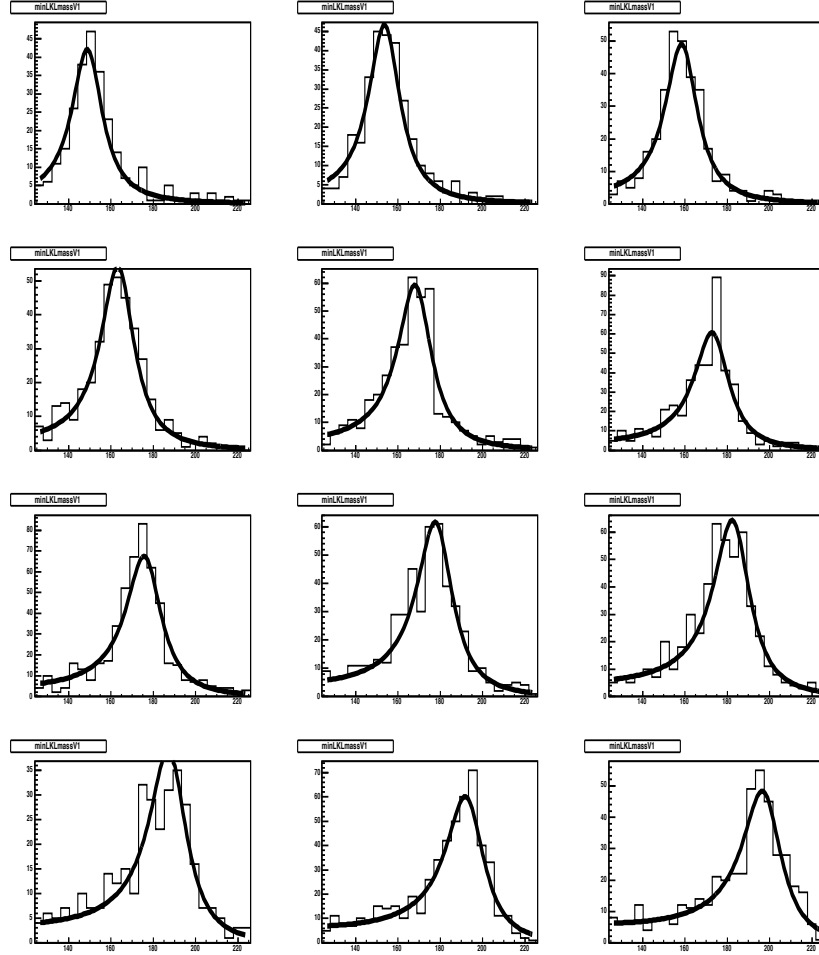
A

Figure D-1. Top templates for $t\bar{t}$ single tagged events for samples with different top masses: from 150 GeV to 200 GeV. A) Case of $JES = -3$. B) Case of $JES = -2$. C) Case of $JES = -1$. D) Case of $JES = 0$. E) Case of $JES = 1$. F) Case of $JES = 2$. G) Case of $JES = 3$.



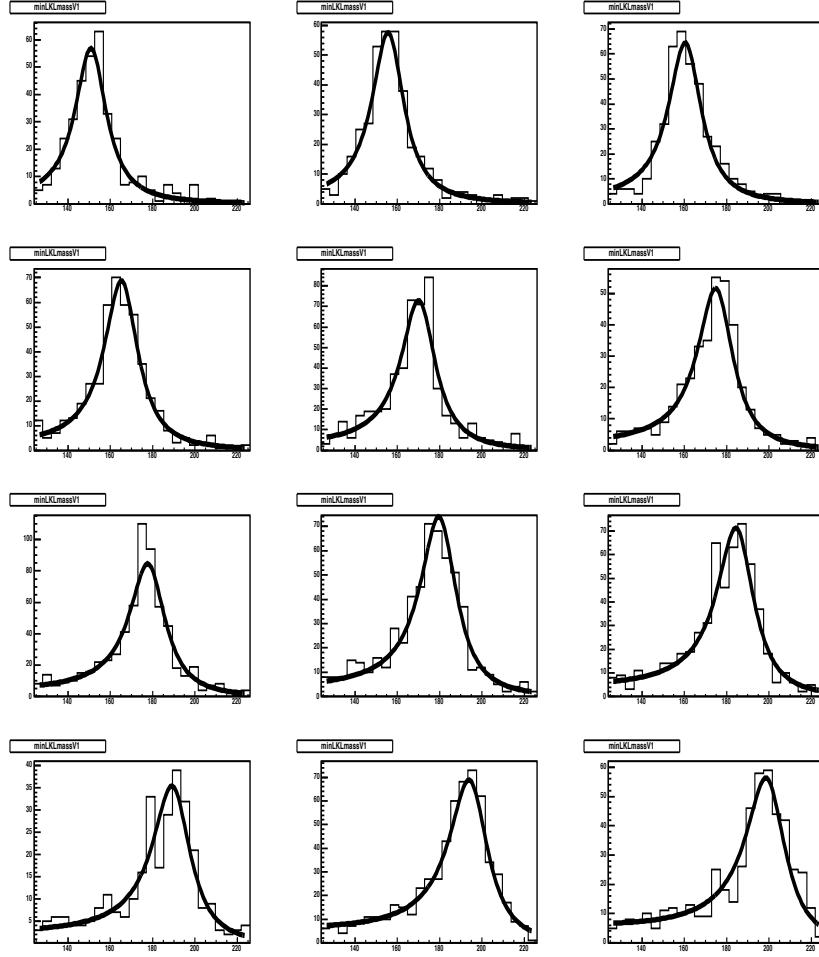
B

Figure D-1. Continued



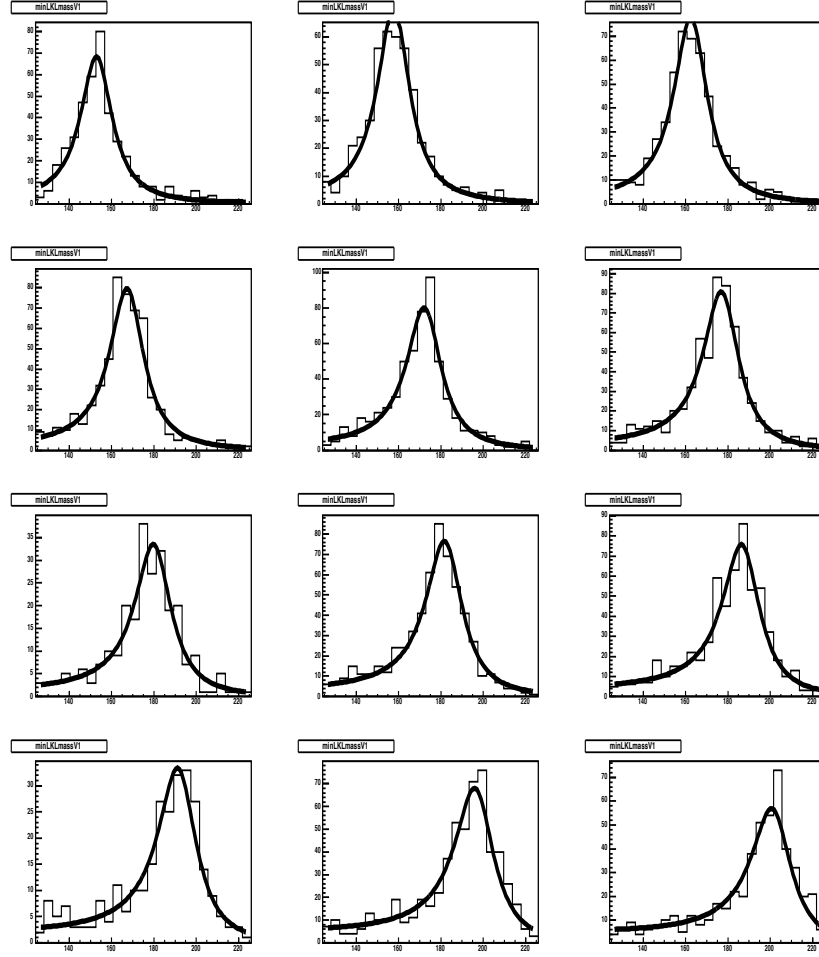
C

Figure D-1. Continued



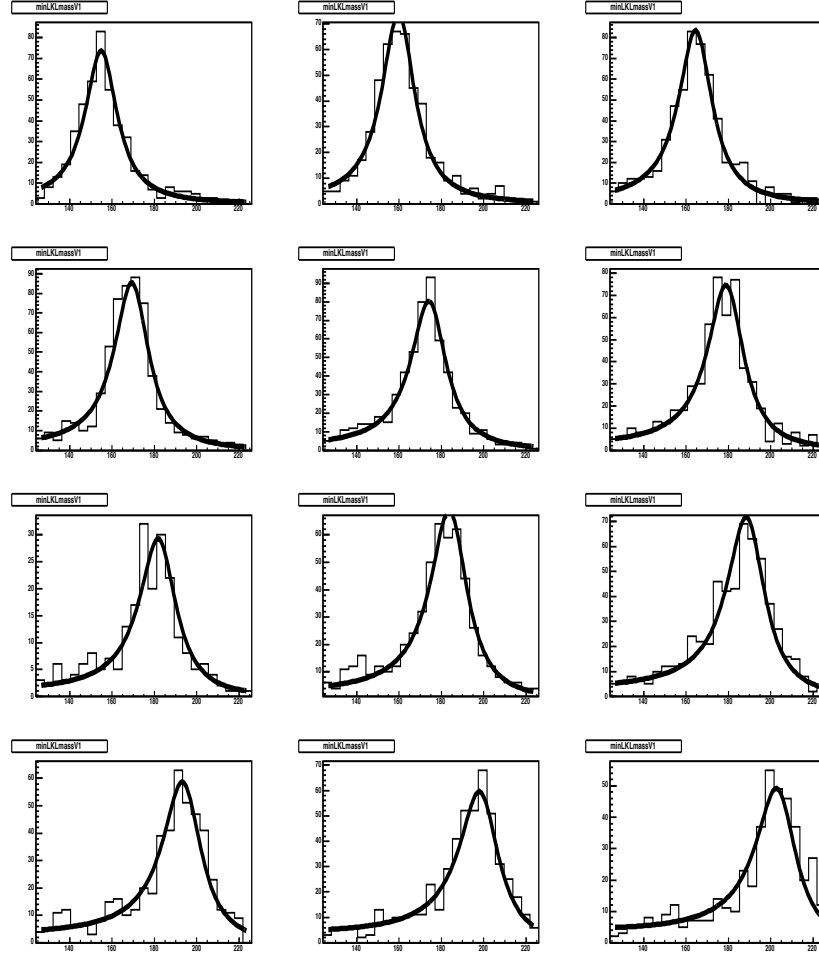
D

Figure D-1. Continued



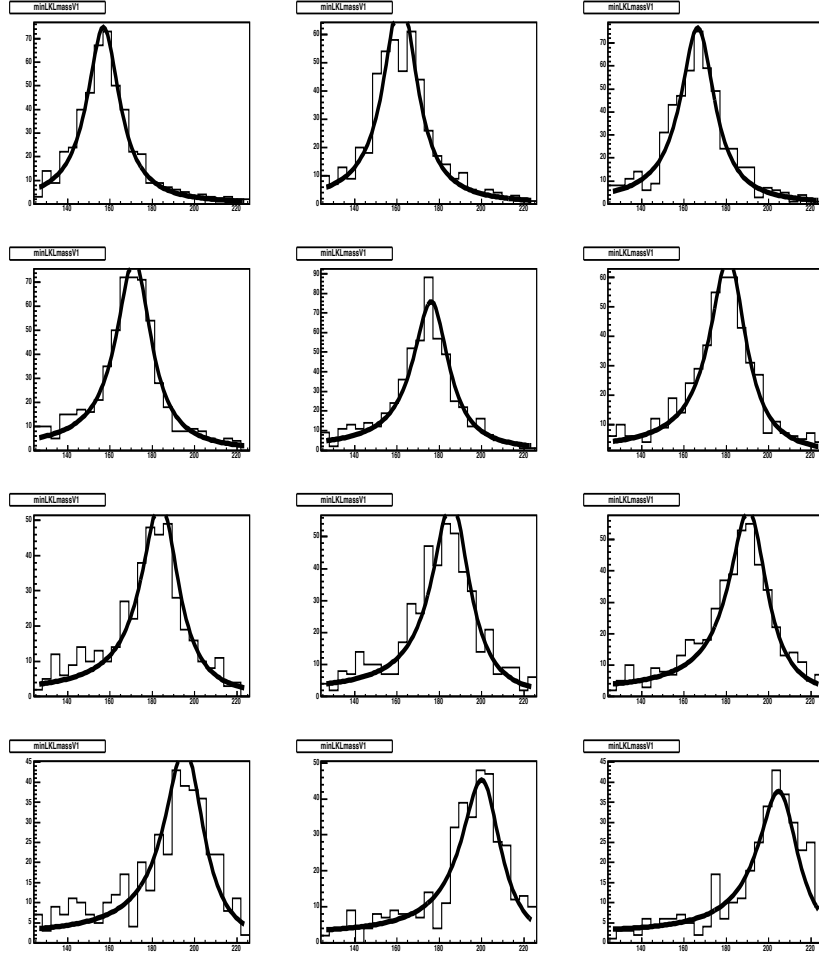
E

Figure D-1. Continued



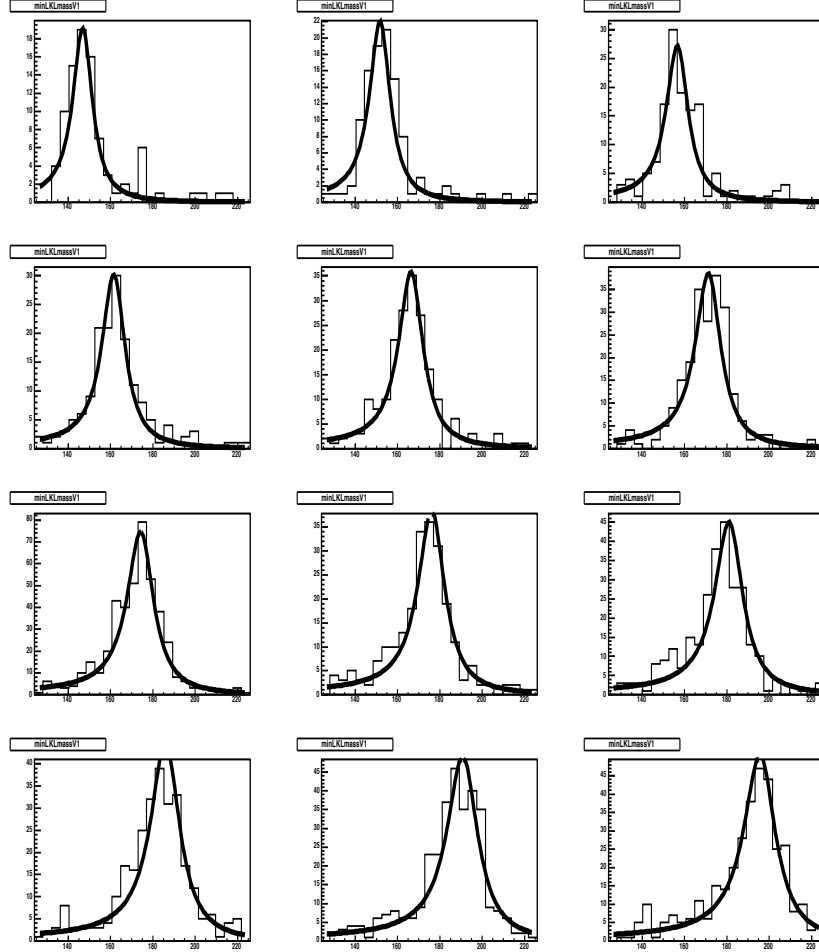
F

Figure D-1. Continued



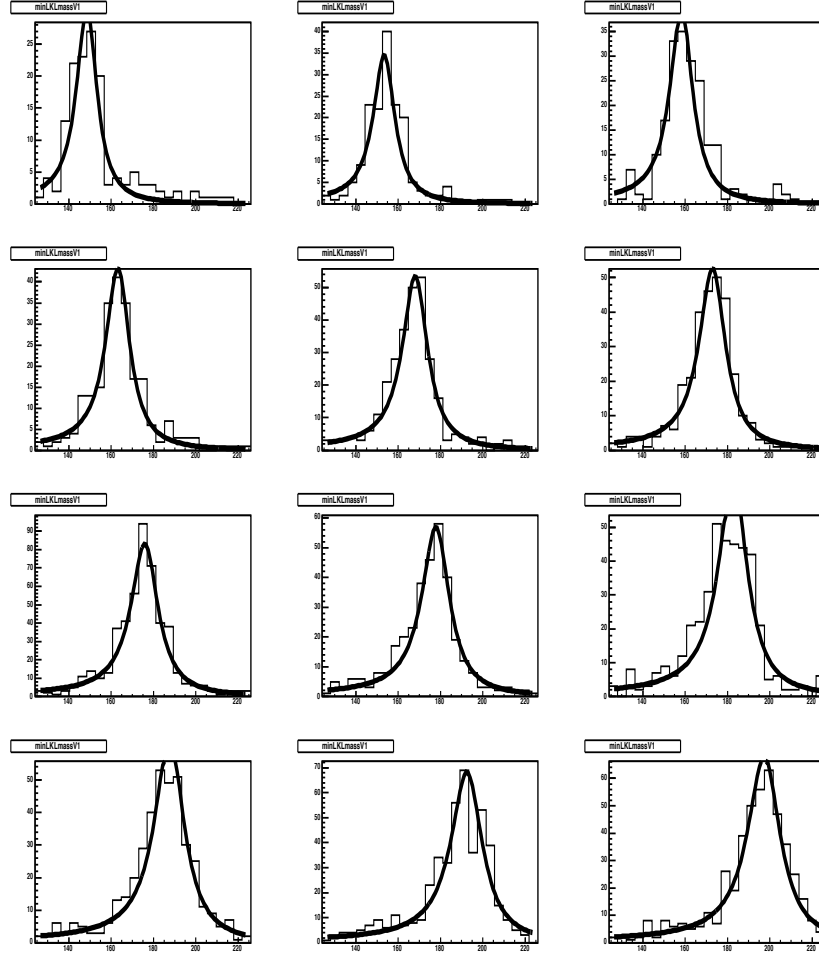
G

Figure D-1. Continued



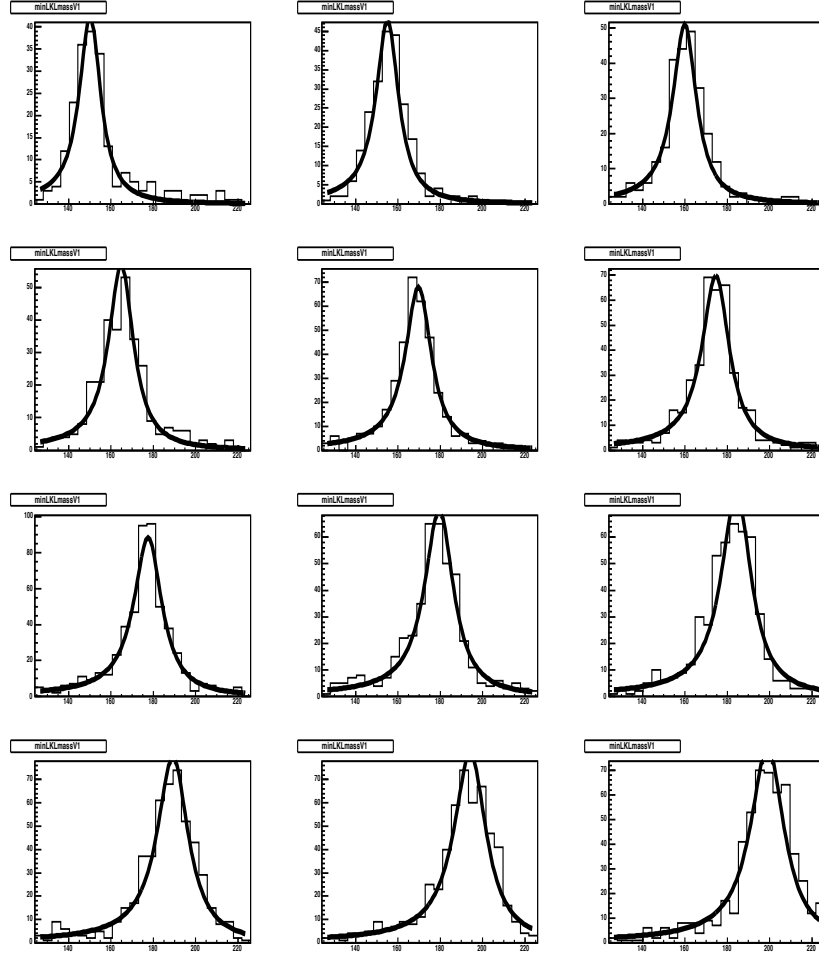
A

Figure D-2. Top templates for $t\bar{t}$ double tagged events for samples with different top masses: from 150 GeV to 200 GeV. A) Case of $JES = -3$. B) Case of $JES = -2$. C) Case of $JES = -1$. D) Case of $JES = 0$. E) Case of $JES = 1$. F) Case of $JES = 2$. G) Case of $JES = 3$.



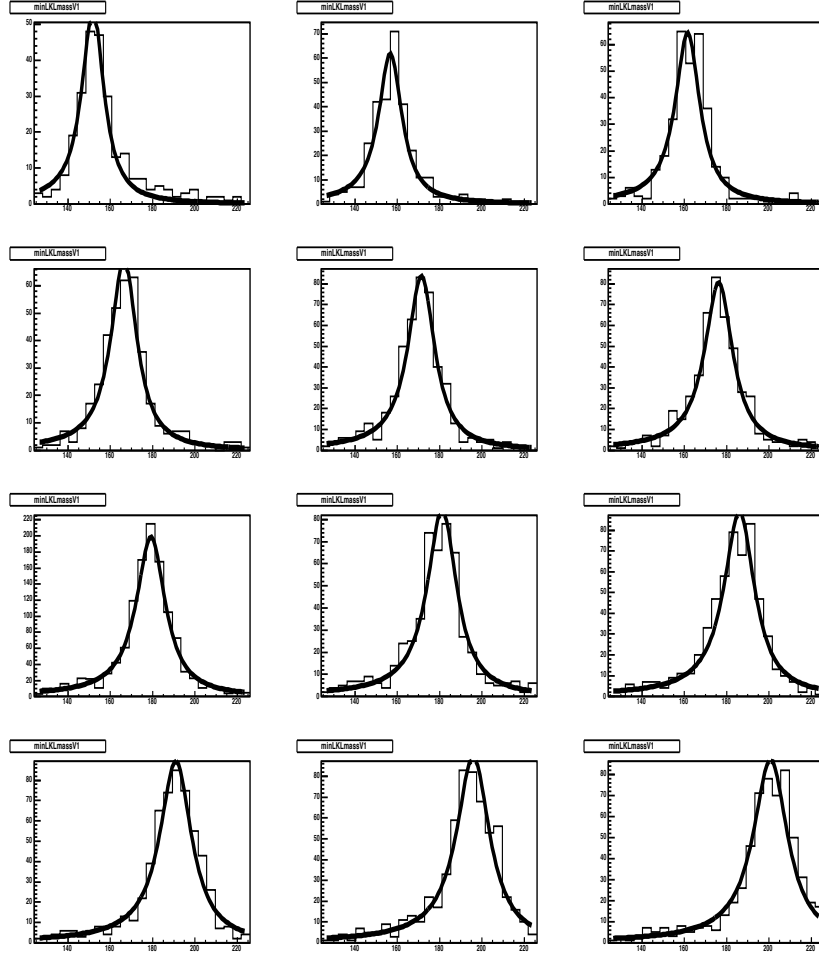
B

Figure D-2. Continued



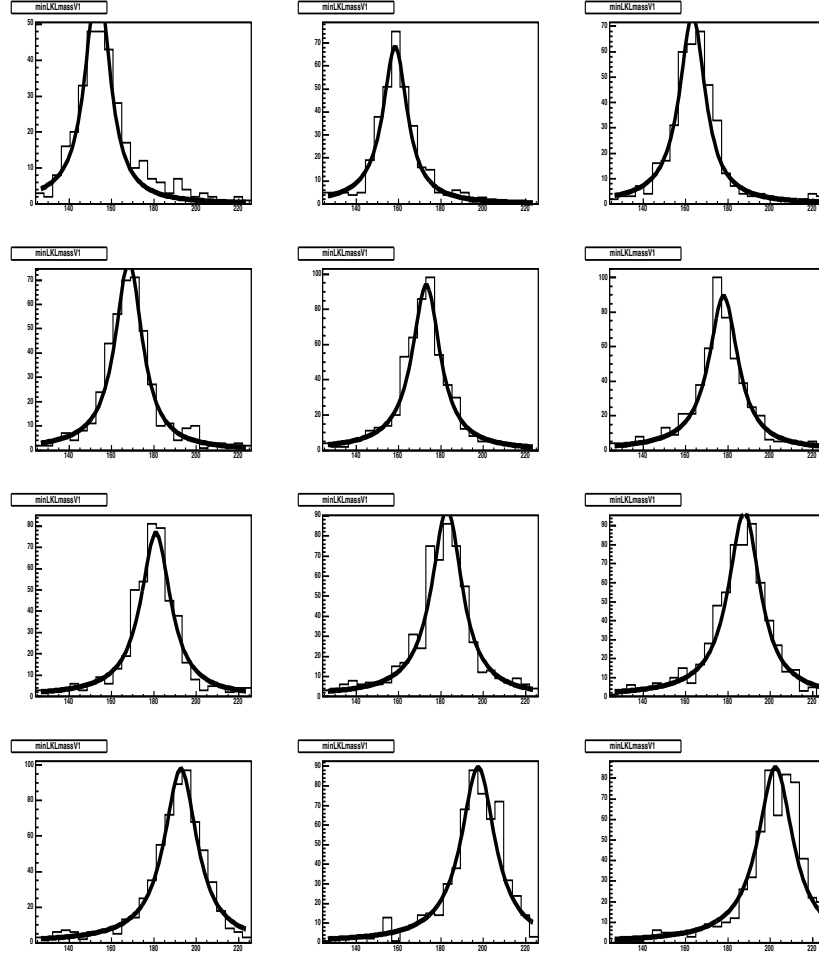
C

Figure D-2. Continued



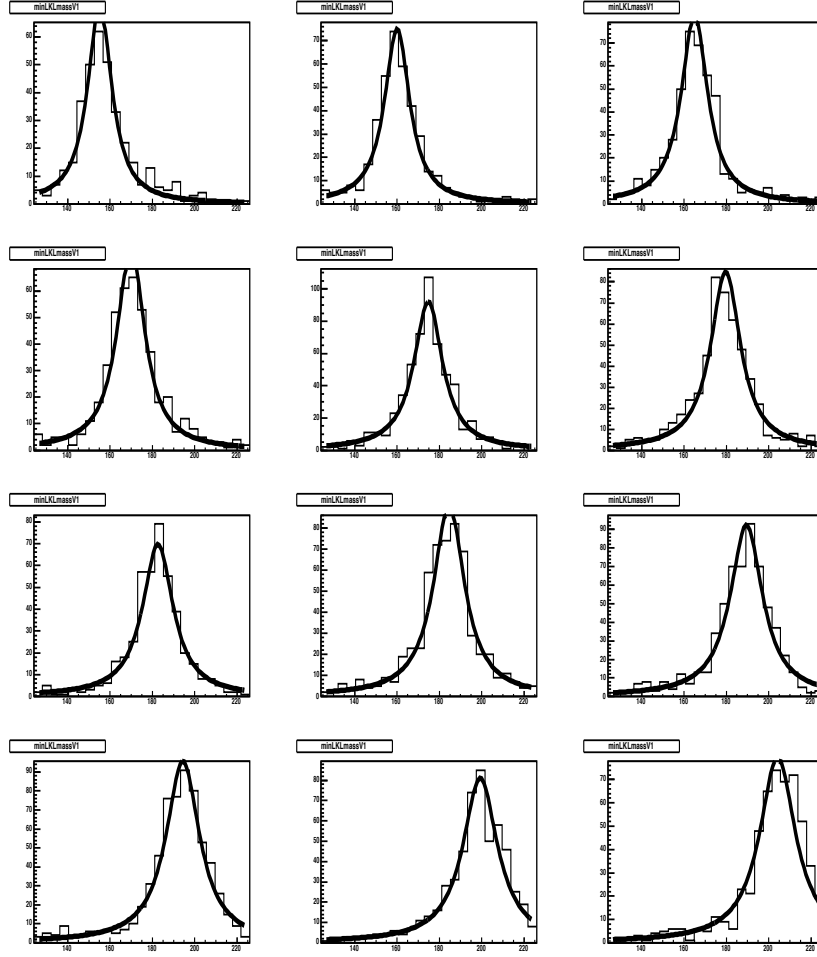
D

Figure D-2. Continued



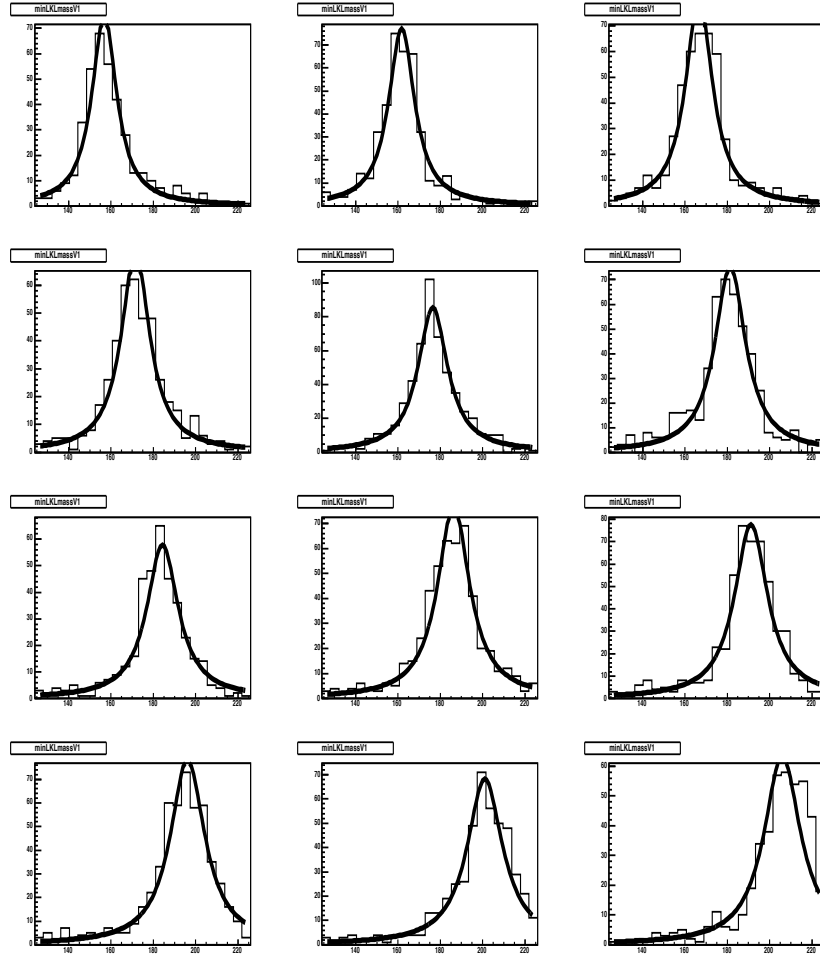
E

Figure D-2. Continued



F

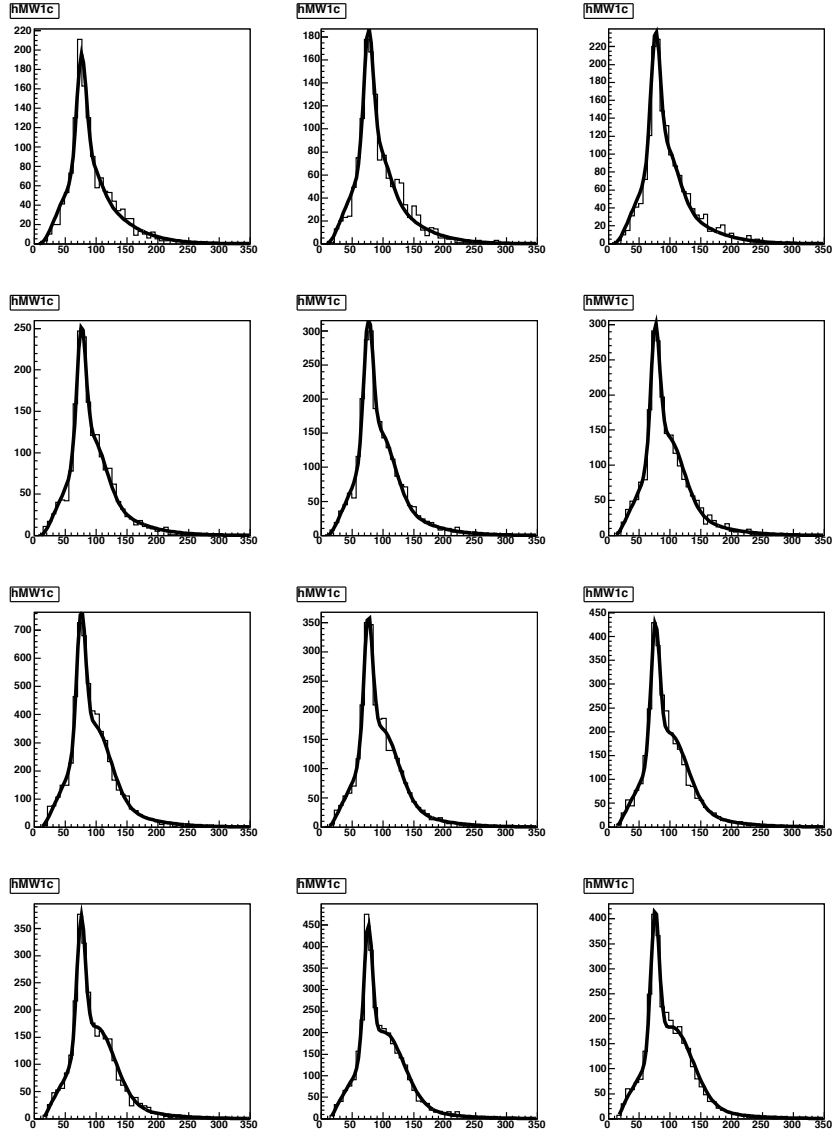
Figure D-2. Continued



G

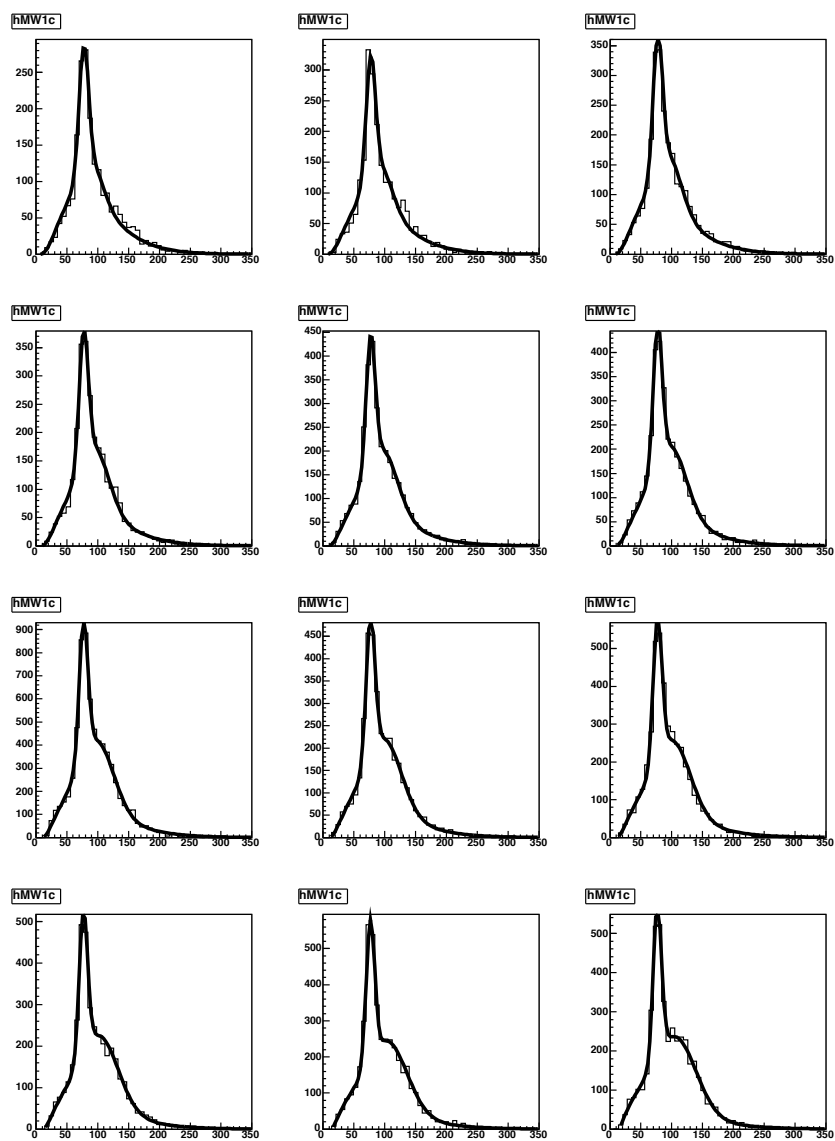
Figure D-2. Continued

APPENDIX E SIGNAL DIJET MASS TEMPLATES



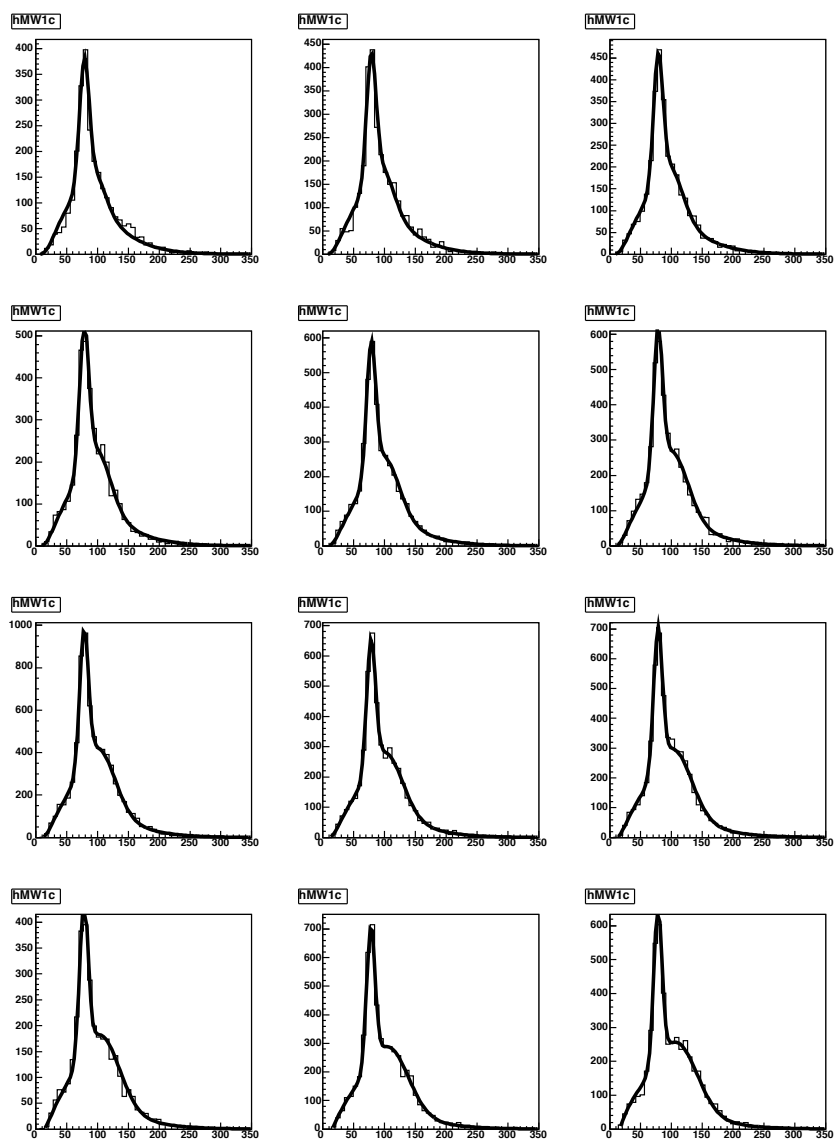
A

Figure E-1. Dijet mass templates for $t\bar{t}$ single tagged events for samples with different top masses: from 150 GeV to 200 GeV. A) Case of $JES = -3$. B) Case of $JES = -2$. C) Case of $JES = -1$. D) Case of $JES = 0$. E) Case of $JES = 1$. F) Case of $JES = 2$. G) Case of $JES = 3$.



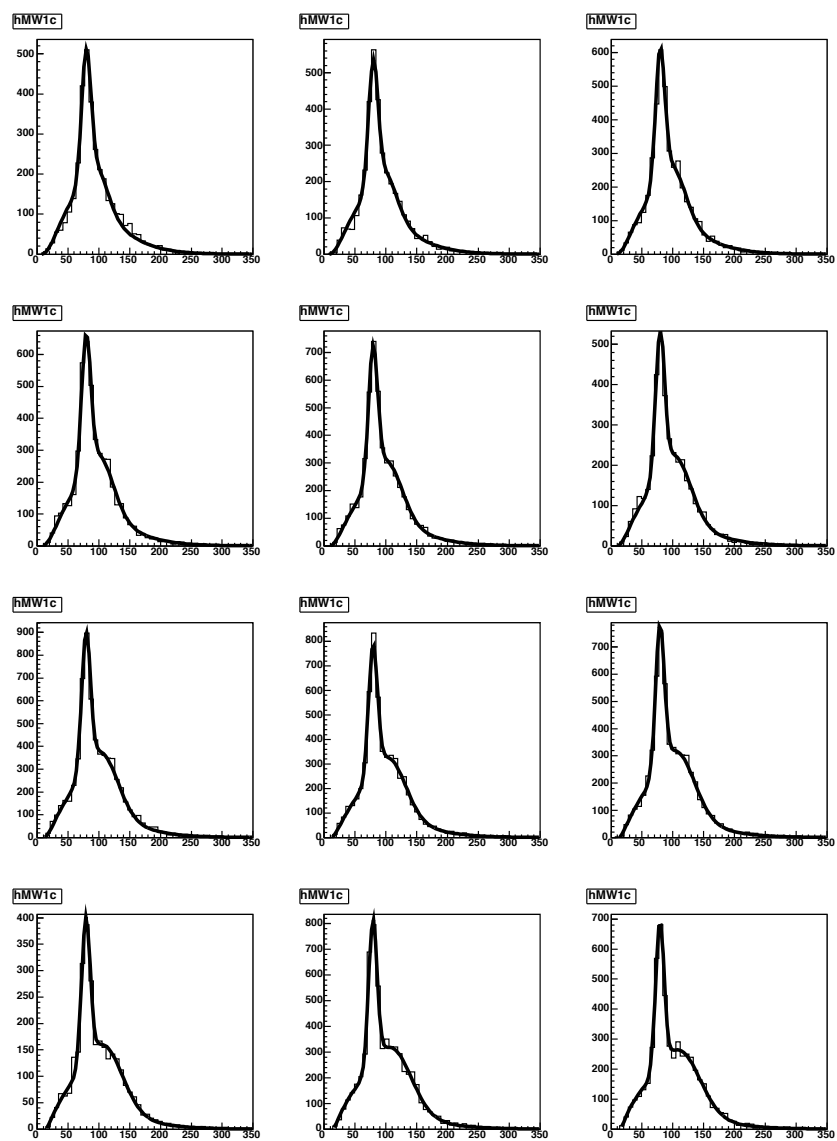
B

Figure E-1. Continued



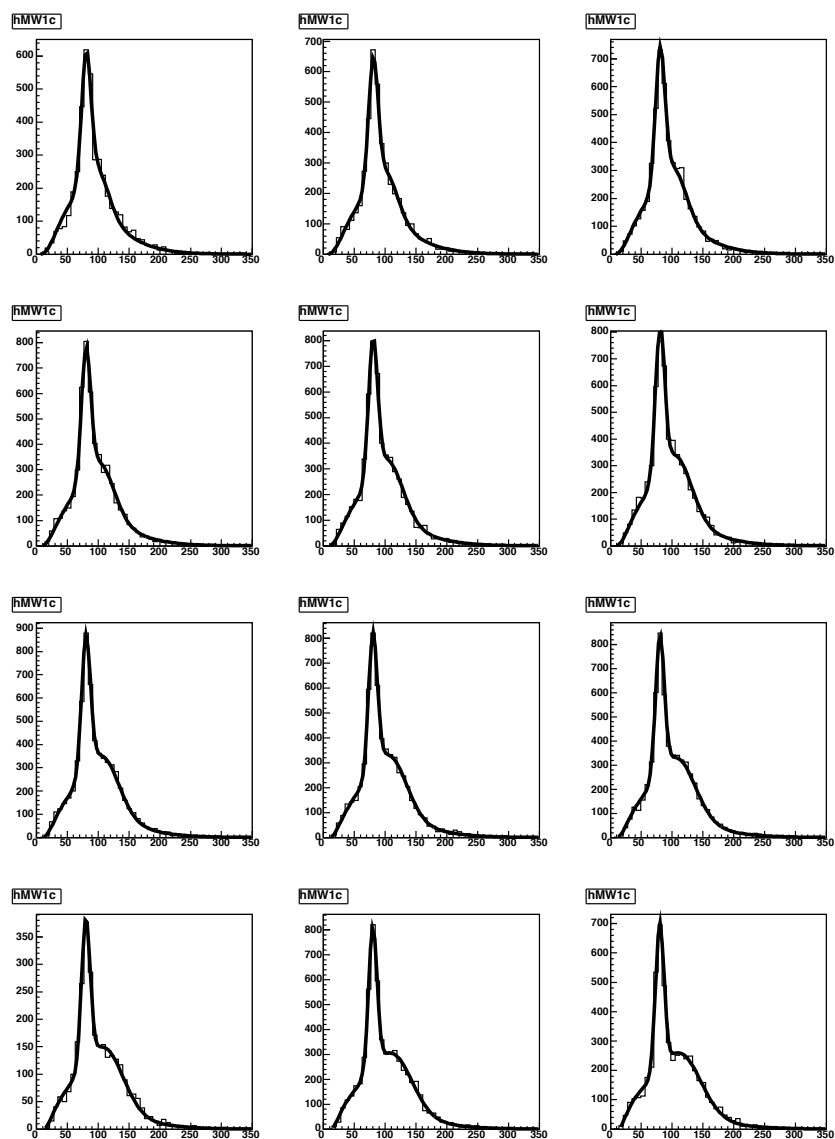
C

Figure E-1. Continued



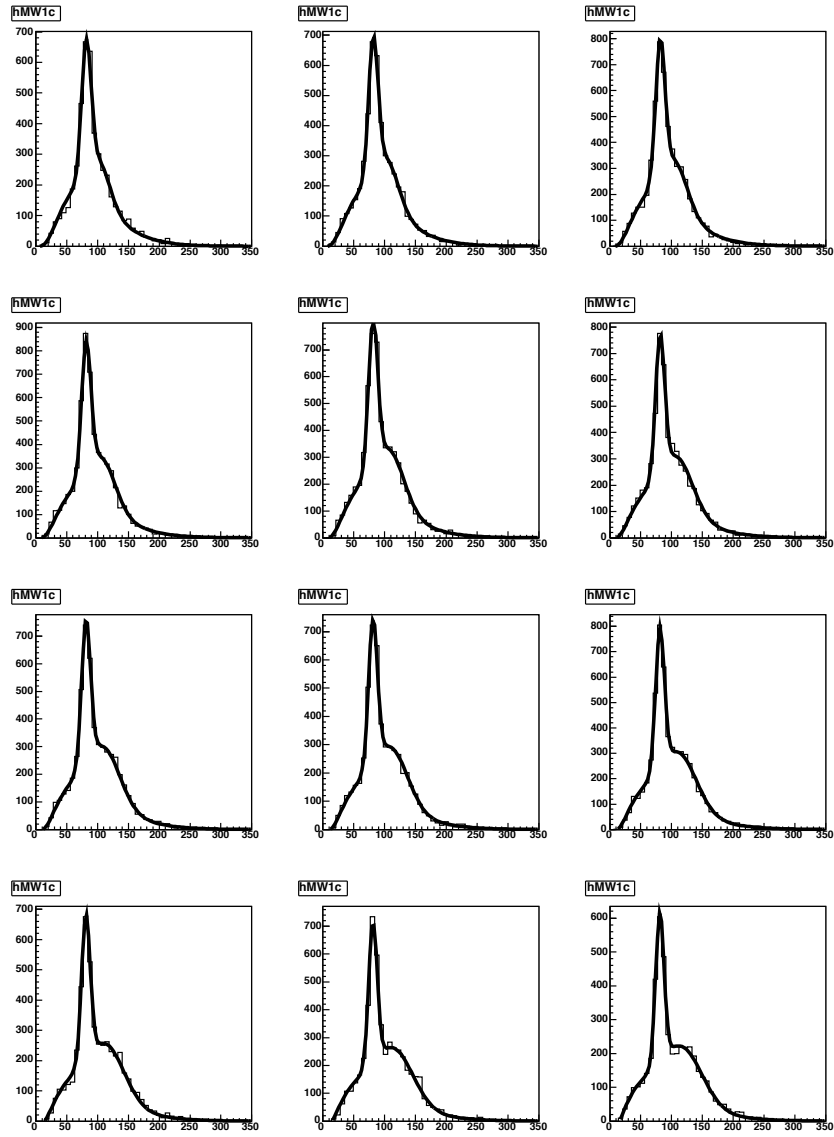
D

Figure E-1. Continued



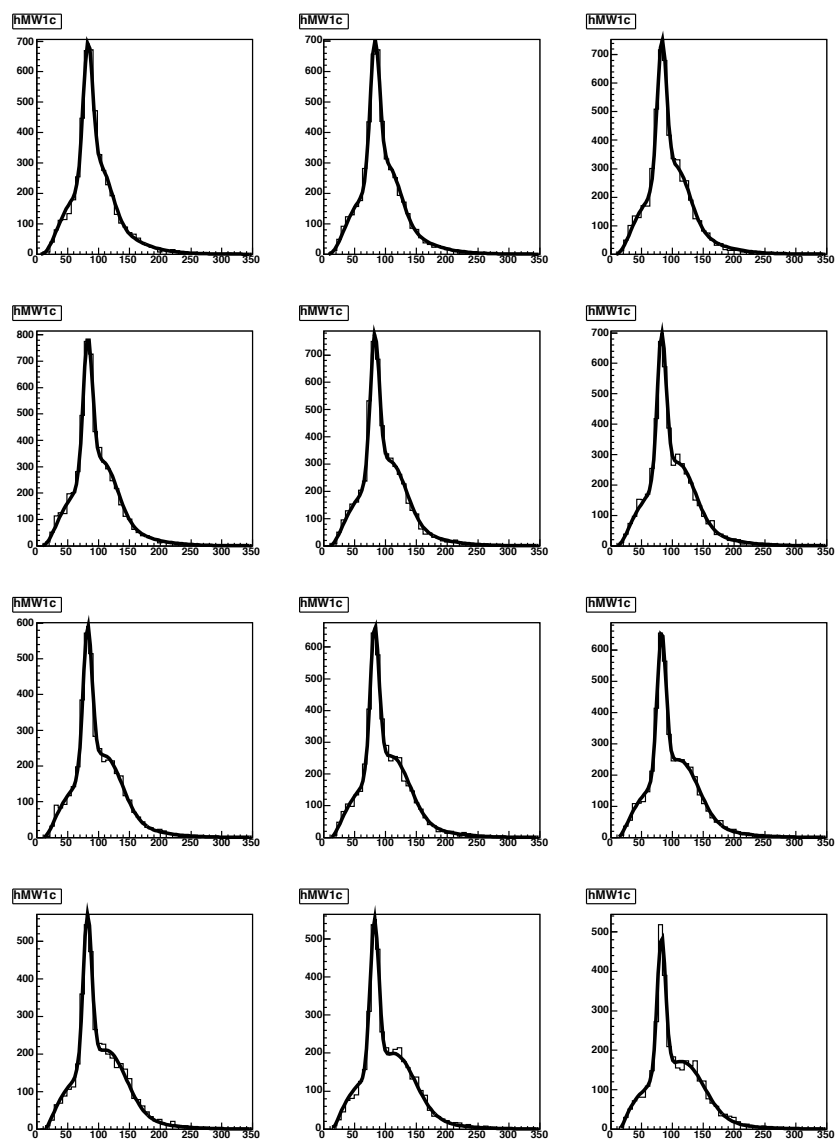
E

Figure E-1. Continued



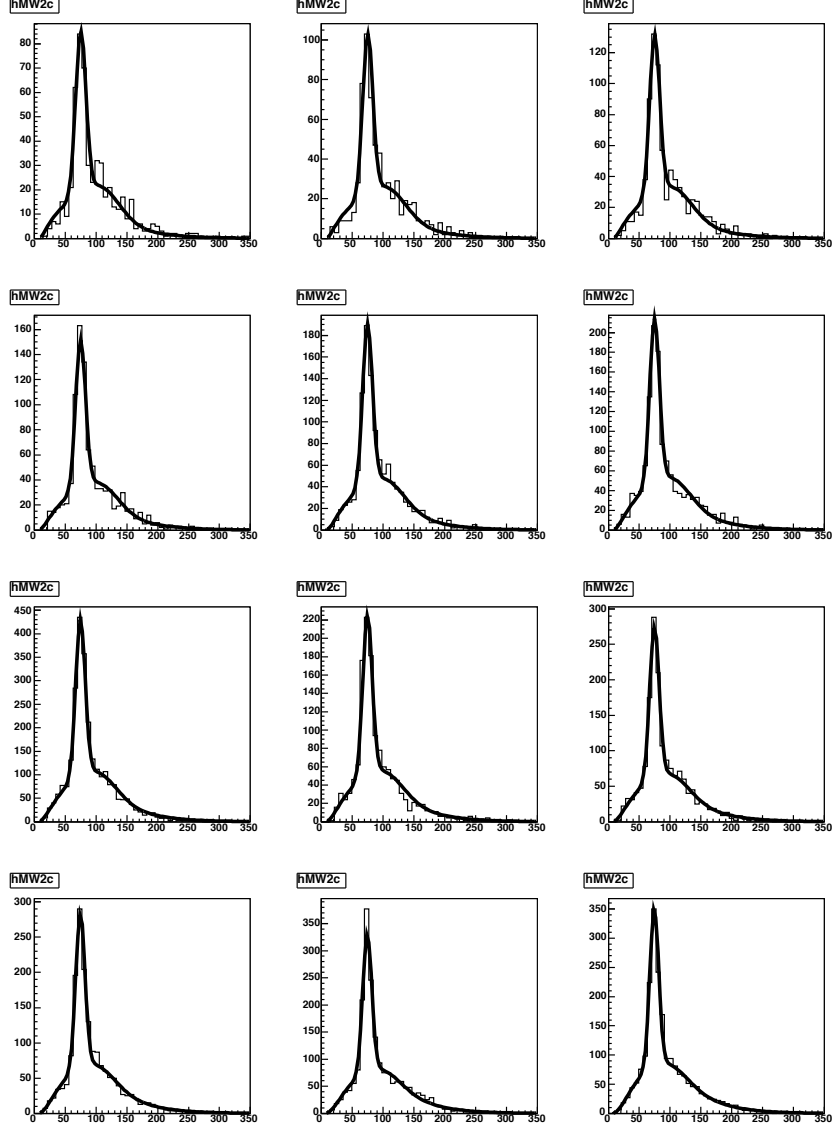
F

Figure E-1. Continued



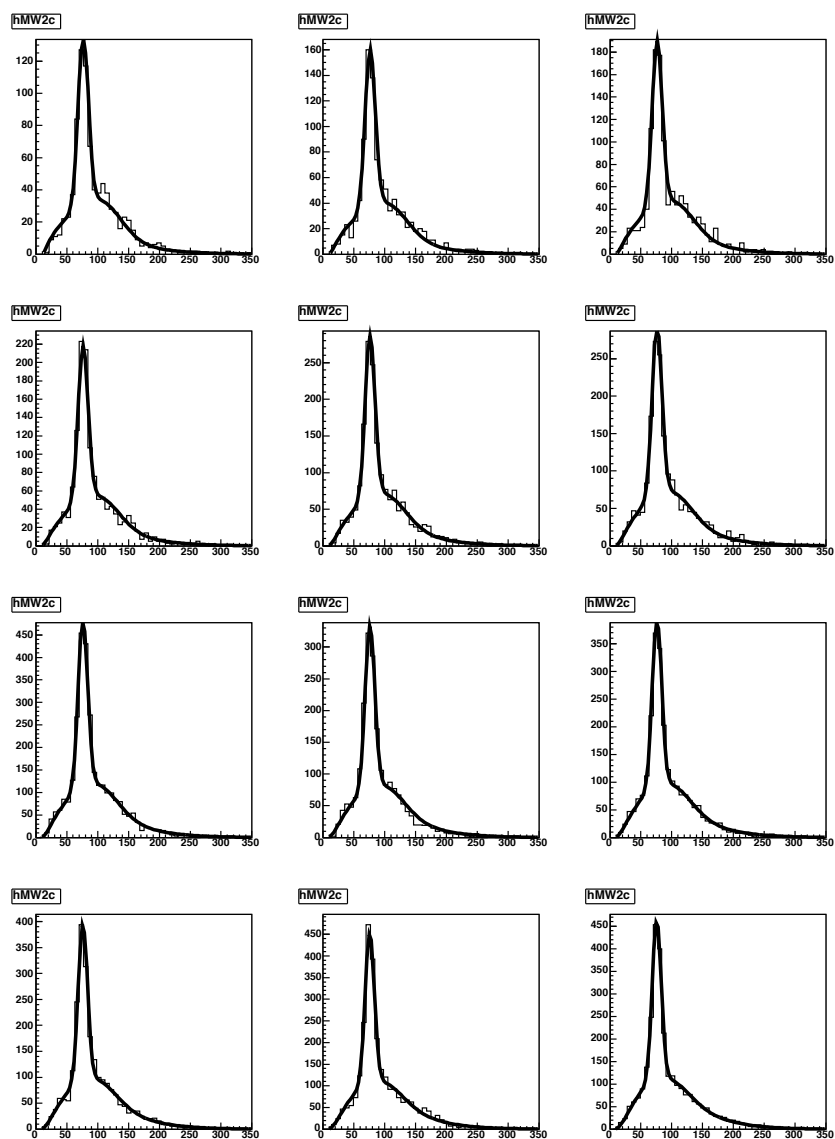
G

Figure E-1. Continued



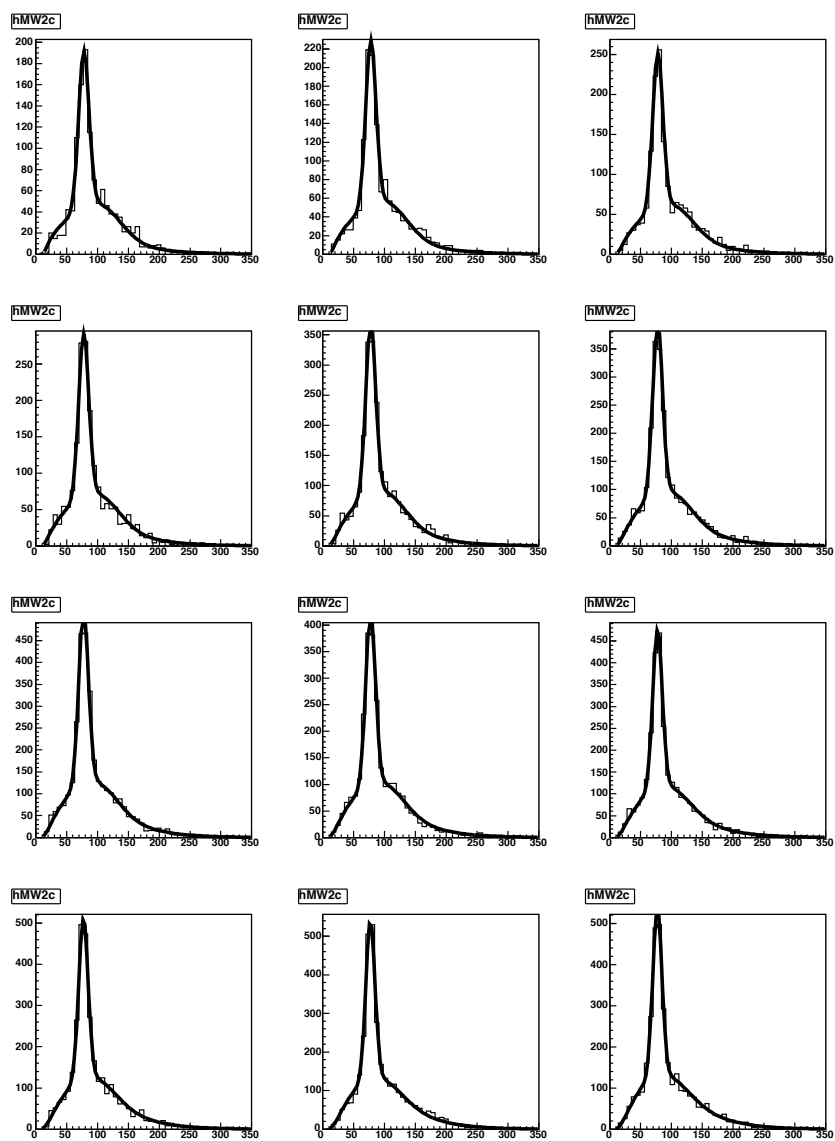
A

Figure E-2. Dijet mass templates for $t\bar{t}$ double tagged events for samples with different top masses: from 150 GeV to 200 GeV. A) Case of $JES = -3$. B) Case of $JES = -2$. C) Case of $JES = -1$. D) Case of $JES = 0$. E) Case of $JES = 1$. F) Case of $JES = 2$. G) Case of $JES = 3$.



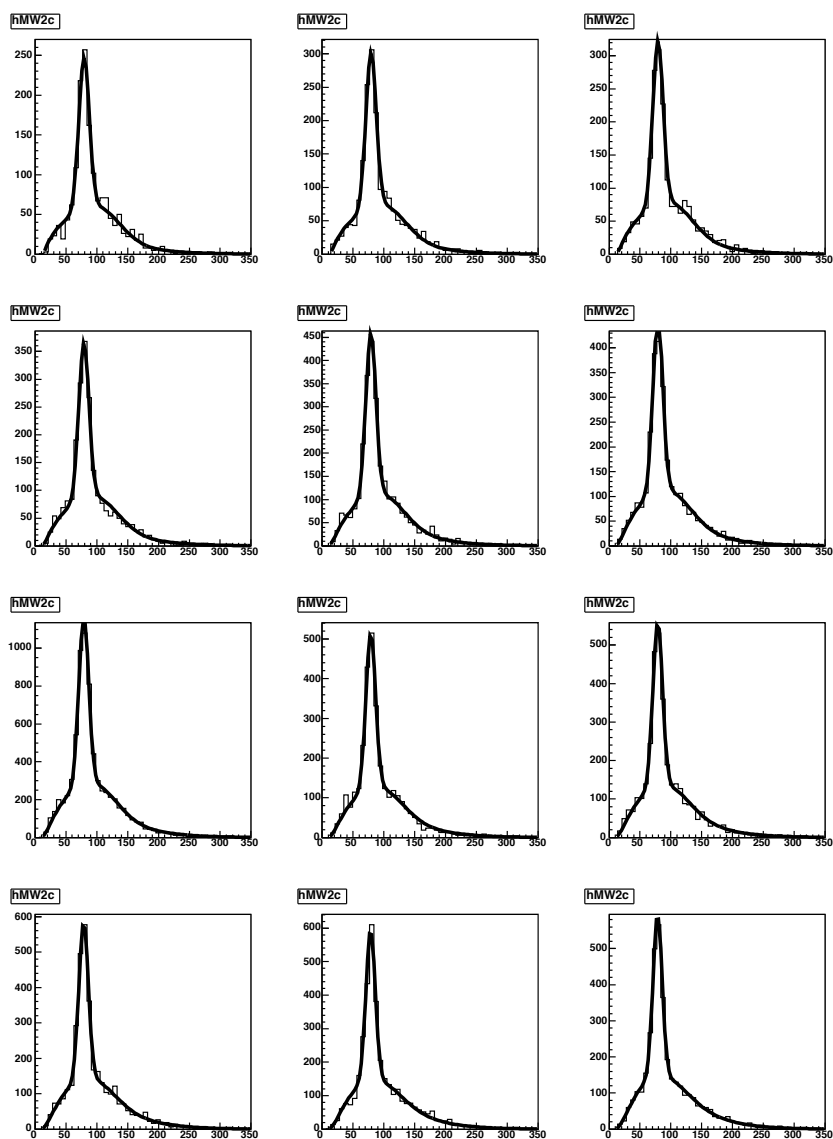
B

Figure E-2. Continued



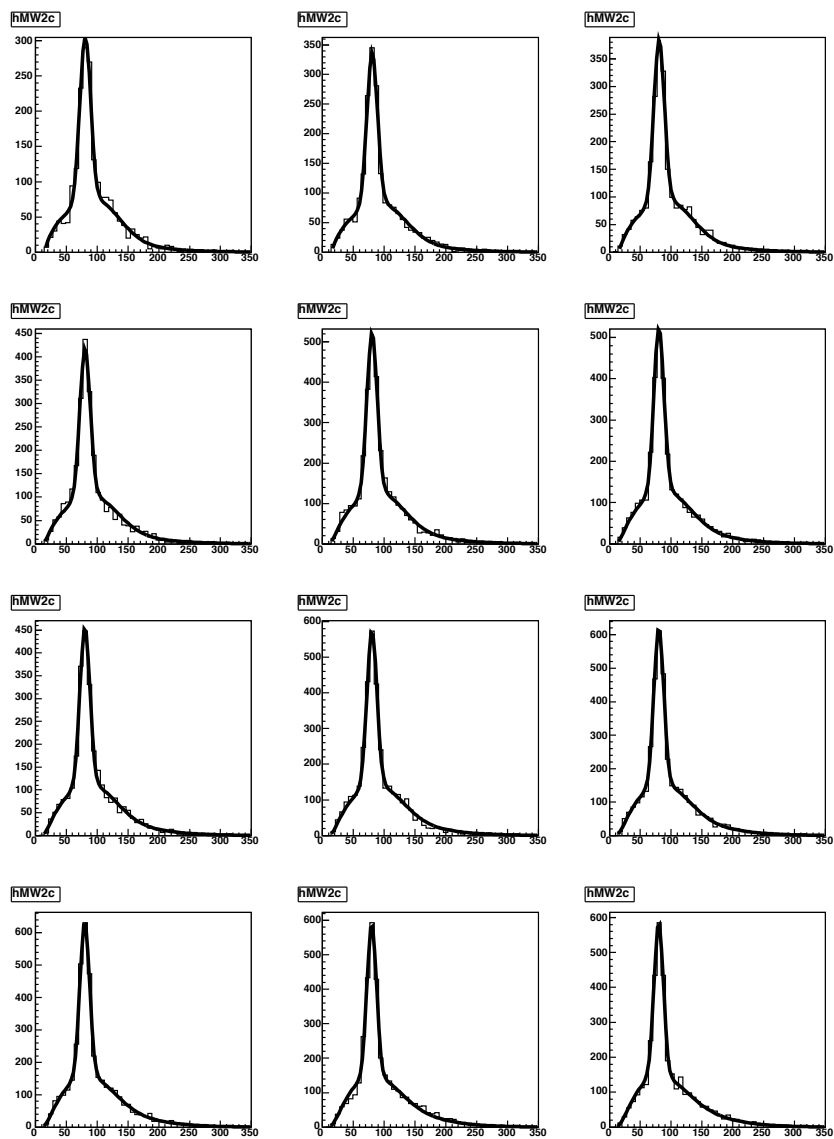
C

Figure E-2. Continued



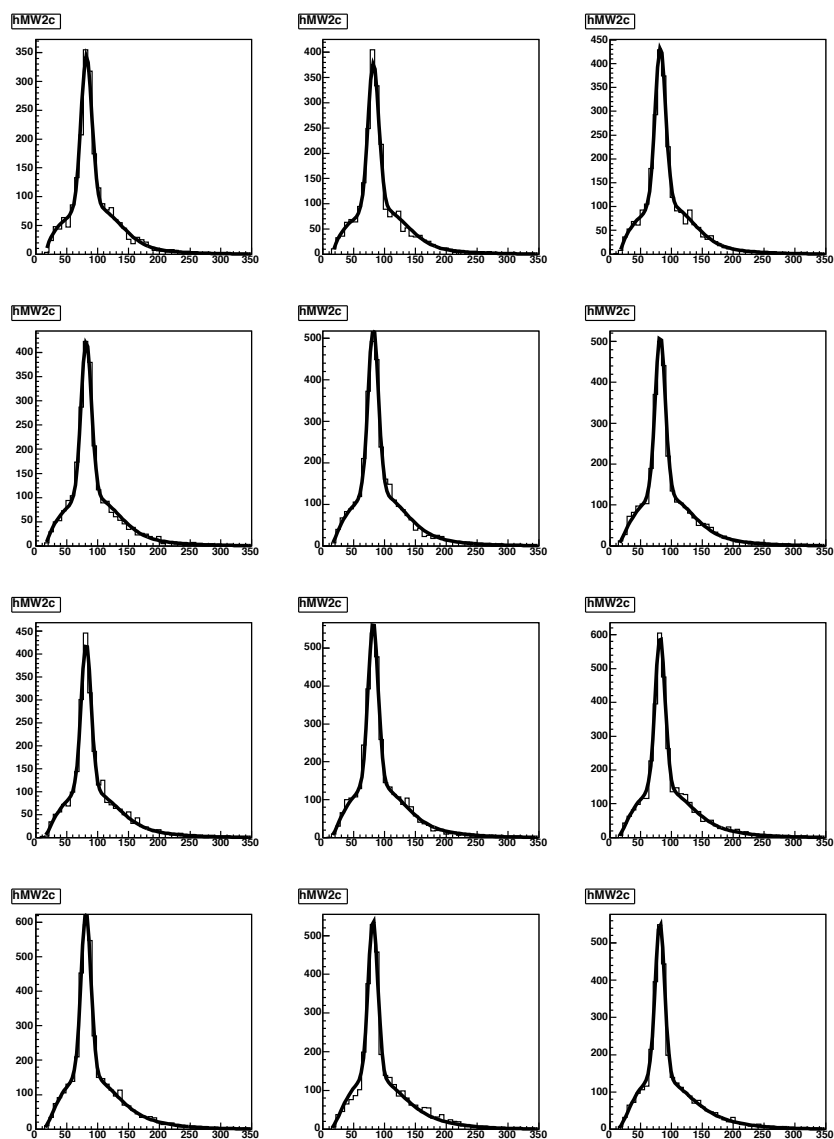
D

Figure E-2. Continued



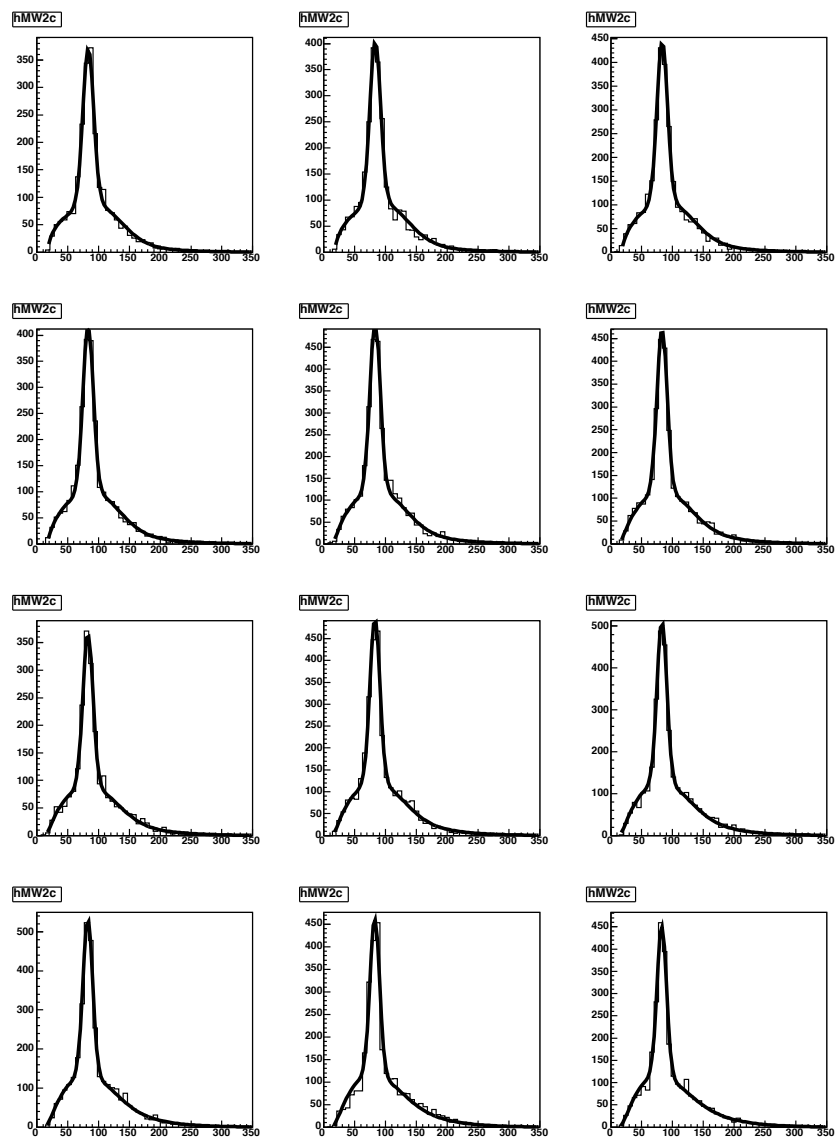
E

Figure E-2. Continued



F

Figure E-2. Continued



G

Figure E-2. Continued

REFERENCES

- [1] F. Abe *et al.*, Phys. Rev. Lett. **74**, 2626 (1995); S. Abachi *et al.*, Phys. Rev. Lett. **74**, 2632 (1995).
- [2] J.H. Kuhn, Lectures delivered at 23rd SLAC Summer Institute, hep-ph/9707321 (1997).
- [3] V.M. Abazov *et al.* (D0 Collaboration), Phys. Rev. D **67**, 012004 (2003).
- [4] T. Affolder *et al.* (CDF Collaboration), Phys. Rev. D **64**, 032002 (2001); Erratum-ibid. D **67**, 119901 (2003).
- [5] D. Acosta *et al.* (CDF Collaboration), Phys. Rev. D **71**, 052003 (2005).
- [6] D. Acosta *et al.* (CDF Collaboration), Phys. Rev. D **93**, 142001 (2004).
- [7] D. Chakraborty, J. Konigsberg and D.L. Rainwater, Ann. Rev. Nucl. Part. Sci. **53**, 301 (2003).
- [8] M. Cacciari *et al.*, JHEP **0404**, 068 (2004); N. Kidonakis and R. Vogt, Phys. Rev. D **68**, 114014 (2003).
- [9] B. Abbott *et al.* (D0 Collaboration), Phys. Rev. D Rapid Comm. **63**, 031101 (2001); V.M. Abazov *et al.* (D0 Collaboration), Phys. Lett. B **517**, 282 (2001); D. Acosta *et al.* (CDF Collaboration), Phys. Rev. D **68**, 052003 (2004).
- [10] D. Acosta *et al.* (CDF Collaboration), Phys. Rev. D **65**, 091120 (2002).
- [11] S.L. Glashow, J. Iliopoulos and L. Maiani, Phys. Rev. D **2**, 1285 (1970).
- [12] S. Eidelman *et al.*, Phys. Lett. B **592**, 1 (2004).
- [13] F. Abe *et al.* (CDF Collaboration), Phys. Rev. Lett. **79**, 3585 (1997); B. Abbott *et al.* (D0 Collaboration), Phys. Rev. Lett. **82**, 4975 (1999); T. Affolder *et al.* (CDF Collaboration), Phys. Rev. D **62**, 012004 (2000); V.M. Abazov *et al.* (D0 Collaboration), Phys. Rev. Lett. **88**, 151803 (2002).
- [14] ALEPH, DELPHI, L3 and OPAL Collaborations and The LEP Working Group for Higgs Boson Searches, hep-ex/0612034 (2006).
- [15] P. Azzi *et al.*, CDF and D0 Collaborations and The Tevatron Electroweak Working Group, hep-ex/0404010 (2004).
- [16] ALEPH, DELPHI, L3 and OPAL Collaborations and The LEP Working Group for Higgs Boson Searches, Phys. Lett. B **565**, 61 (2003).

- [17] H. Haber and R. Hempfling, Phys. Rev. Lett. **66**, 1815 (1991); Y. Okada, M. Yamaguchi and T. Yanagida, Prog. Theor. Phys., **85**, 1 (1991); J. Ellis, G. Ridolfi and F. Zwirner, Phys. Lett. B **257**, 83 (1991); J. Ellis, G. Ridolfi and F. Zwirner, Phys. Lett. B **262**, 477 (1991); R. Barbieri and M. Frigeni, Phys. Lett. B **258**, 395 (1991).
- [18] S. Heinemeyer, W. Hollik and G. Weinglein, Eur. Phys. J. C **9**, 343 (1999); G. Degrassi, S. Heinemeyer, W. Hollik, P. Slavich and G. Weinglein, Eur. Phys. J. C **28**, 133 (2003).
- [19] S. Heinemeyer and G. Weinglein, hep-ph/0412214 (2004).
- [20] A review of dynamical electroweak symmetry breaking models can be found in: C.T. Hill and E.H. Simmons, Phys. Rept. **381** 235 (2003); Erratum-ibid. **390**, 553 (2004).
- [21] S. Weinberg, Phys. Rev. D **13** 974 (1976); L. Susskind, Phys. Rev. D **20** 2619 (1979).
- [22] C.T. Hill, Phys. Lett. B **266**, 419 (1991).
- [23] D. Cronin-Hennessy, A. Beretvas, P.F. Derwent, Nucl. Instrum. Meth. A **443**, 37-50 (2000).
- [24] S. Van Der Meer *et al.*, Phys. Rep. **58**, 73 (1980).
- [25] R. Blair *et al.* (CDF Collaboration), Fermilab Report No. FERMILAB-Pub-96-390-E, Section 12 (1996).
- [26] D. Acosta *et al.* (CDF Collaboration), Phys. Rev. D **71** 032001 (2005).
- [27] D. Acosta *et al.* (CDF Collaboration), Nucl. Instrum. Meth. A **461** 540-544 (2001).
- [28] C.S. Hill *et al.* (CDF Collaboration), Nucl. Instrum. Meth. A **530** 1 (2004).
- [29] A. Sill *et al.* (CDF Collaboration), Nucl. Instrum. Meth. A **447** 1-8 (2000).
- [30] T. Affolder *et al.* (CDF Collaboration), Nucl. Instrum. Meth. A **453** 84 (2000).
- [31] T. Affolder *et al.* (CDF Collaboration), Nucl. Instrum. Meth. A **526** 249-299 (2004).
- [32] L. Balka *et al.* (CDF Collaboration), Nucl. Instrum. Meth. A **267** 272-279 (1998); S. Bertolucci *et al.* (CDF Collaboration), Nucl. Instrum. Meth. A **267** 301-314 (1998).
- [33] M. Albrow *et al.* (CDF Collaboration), Nucl. Instrum. Meth. A **480** 524-545 (2002); R. Blair *et al.* (CDF Collaboration), Fermilab Report No. FERMILAB-Pub-96-390-E, Section 9 (1996); G. Apollinari *et al.* (CDF Collaboration), Nucl. Instrum. Meth. A **412** 515-526 (1998).
- [34] A. Artikov *et al.* (CDF Collaboration), Nucl. Instrum. Meth. A **538** 358-371 (2005).
- [35] P. Gatti, "Performance of the new tracking system at CDF II", CDF Note 5561.

- [36] W. Yao, K. Bloom, “Outside-In silicon tracking at CDF”, CDF Note 5991.
- [37] H. Stadie, W. Wagner, T. Muller, “VxPrim in Run II”, CDF Note 6047.
- [38] J.F. Arguin, B. Heinemann, A. Yagil, “The z-Vertex Algorithm in Run II”, CDF Note 6238.
- [39] CDF collaboration, Jet Energy Group, “Jet Energy Corrections at CDF”, CDF Note 7543.
- [40] A.A. Bhatti, K. Hatakeyama, “Relative jet energy corrections using missing Et projection fraction and dijet balancing”, CDF Note 6854.
- [41] B. Cooper, M. D’Onofrio, G. Flanagan, “Multiple interaction corrections”, CDF Note 7365.
- [42] A. Bhatti, F. Canelli, “Absolute corrections and their systematic uncertainties”, CDF Note 5456.
- [43] J.F. Arguin, B. Heinemann, “Underlying event corrections for Run II”, CDF Note 6293.
- [44] A. Bhatti, F. Canelli, L. Galtieri, B. Heinemann, “Out-of-Cone corrections and their Systematic Uncertainties”, CDF Note 7449.
- [45] R. Wagner, “Electron Identification for Run II: algorithms”, CDF Note 5456.
- [46] J. Bellinger, “A guide to muon reconstruction and software for Run 2”, CDF Note 5870.
- [47] D. Glenzinski, “A detailed study of the SECVTX algorithm”, CDF Note 2925.
- [48] D. Acosta, “Introduction to Run II jet probability heavy flavor tagging”, CDF Note 6315.
- [49] L. Cerrito, A. Taffard, “A soft muon tagger for Run II”, CDF Note 6305.
- [50] P. Azzi, A. Castro, A. Gresele, J. Konigsberg, G. Lungu and A. Sukhanov, “New kinematical selection for All-hadronic $t\bar{t}$ events in the Run II multijet dataset”, CDF Note 7717.
- [51] P. Azzi, A. Castro, A. Gresele, J. Konigsberg, G. Lungu and A. Sukhanov, “B-tagging efficiency and background estimate in the Run II multijet dataset”, CDF Note 7723.
- [52] Roger Barlow, “Application of the Bootstrap resampling technique to Particle Physics experiments”, MAN/HEP/99/4 April 14 2000.
- [53] J.F. Arguin, P. Sinervo, “b-jets Energy Scale Uncertainty From Existing Experimental Constraints”, CDF Note 7252.

- [54] A. Abulencia, J. Adelman, E. Brubaker, G. Chlachidze, W.T. Fedorko, S.H. Kim, Y.K. Kim, Y.J. Lee, T. Maruyama, K. Sato, M. Shochet, P. Sinervo, T. Tomura, G. Velev, U.K. Yang, “Top Quark Mass Measurement Using the Template Method in the Lepton + Jets Channel with 680 pb⁻¹”, CDF Note 8074.
- [55] M. Cacciari, S. Frixione, M.L. Mangano, P. Nason, G. Ridolfi, “The $t\bar{t}$ cross-section at 1.8 and 1.96 TeV: a study of the systematics due to parton densities and scale dependence”, hep-ph/0303085 (2003).
- [56] A. Castro, F. Margaroli, “All-hadronic top mass measurement using the Template Method with 1.02 fb⁻¹”, CDF Note 8358.
- [57] Tevatron Electroweak Working Group, “A Combination of CDF and D0 Results on the Mass of the Top Quark”, hep-ex/0703034v1 (2007).

BIOGRAPHICAL SKETCH

Gheorghe Lungu [REDACTED]

[REDACTED]. After graduating from high school in 1996 he was accepted in the Physics Department of the University of Bucharest. He graduated with a B.Sc. in physics in 2000, entered the Physics Graduate Department at University of Florida in 2001 and moved to Fermilab in 2003 for research within the CDF collaboration under the supervision of Prof. Jacobo Konigsberg.